VISER
www.viserdata.com

RESEARCH AND APPLICATION OF
MATERIALS SCIENCE

ISSN:2661-4464(online)   2661-4456(print)
Volume 2 No. 1   2020

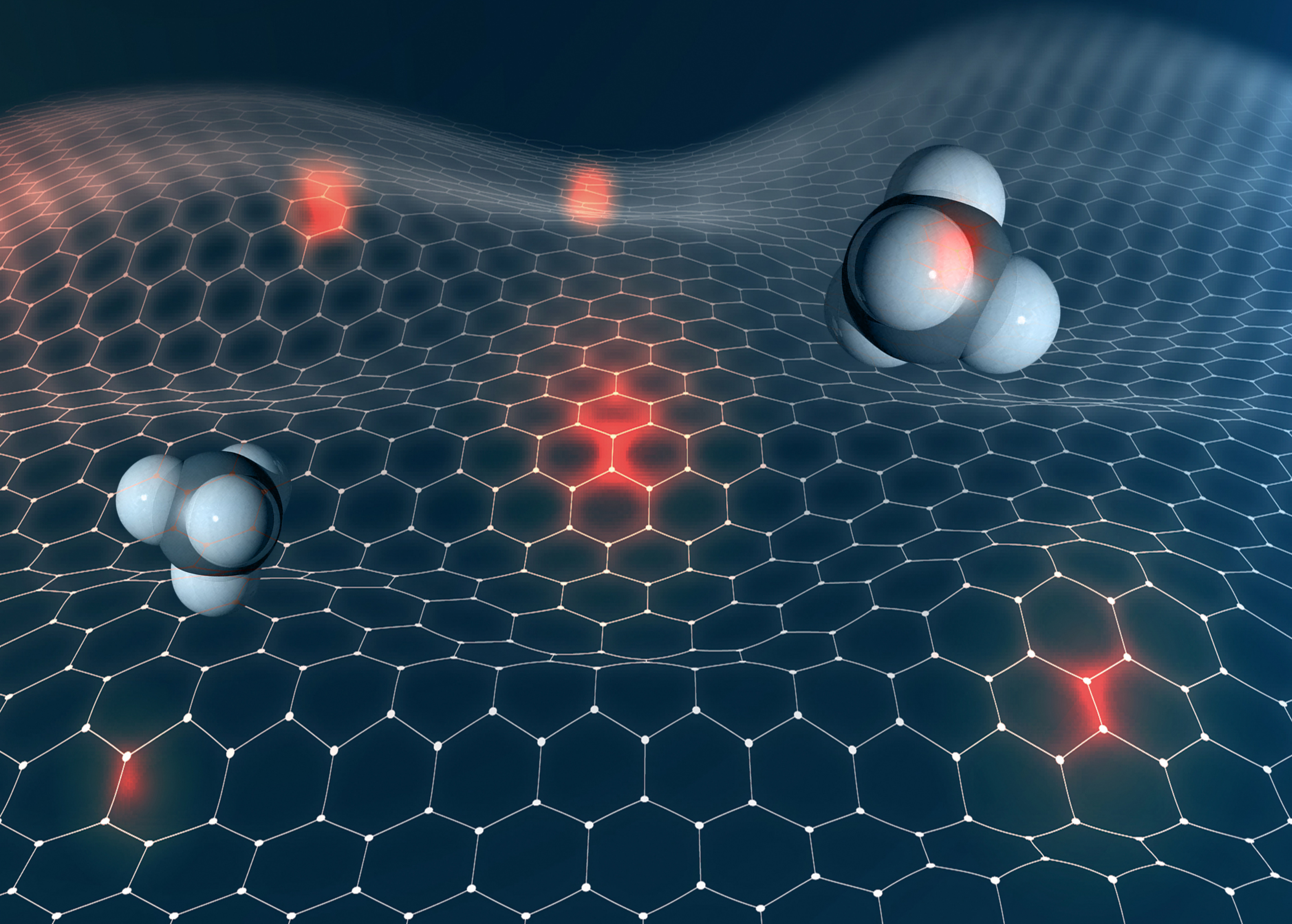

COMPANY INTRODUCTION

Viser Technology Pte. Ltd. was founded in Singapore with branch offices in both Hebei and Chongqing, China. Viser focuses on publishing scientific and technological journals and books that promote the exchange of scientific and technological findings among the research community and around the globe. Despite being a young company, Viser is actively connecting with well-known universities, research institutes, and indexation database, and has already established a stable collaborative relationship with them. We also have a group of experienced editors and publishing experts who are dedicated to publishing high-quality journal and book contents. We offer the scholars various academic journals covering a variety of subjects and we are committed to reducing the hassles of scholarly publishing. To achieve this goal, we provide scholars with an all-in-one platform that offers solutions to every publishing process that a scholar needs to go through in order to show their latest finding to the world.

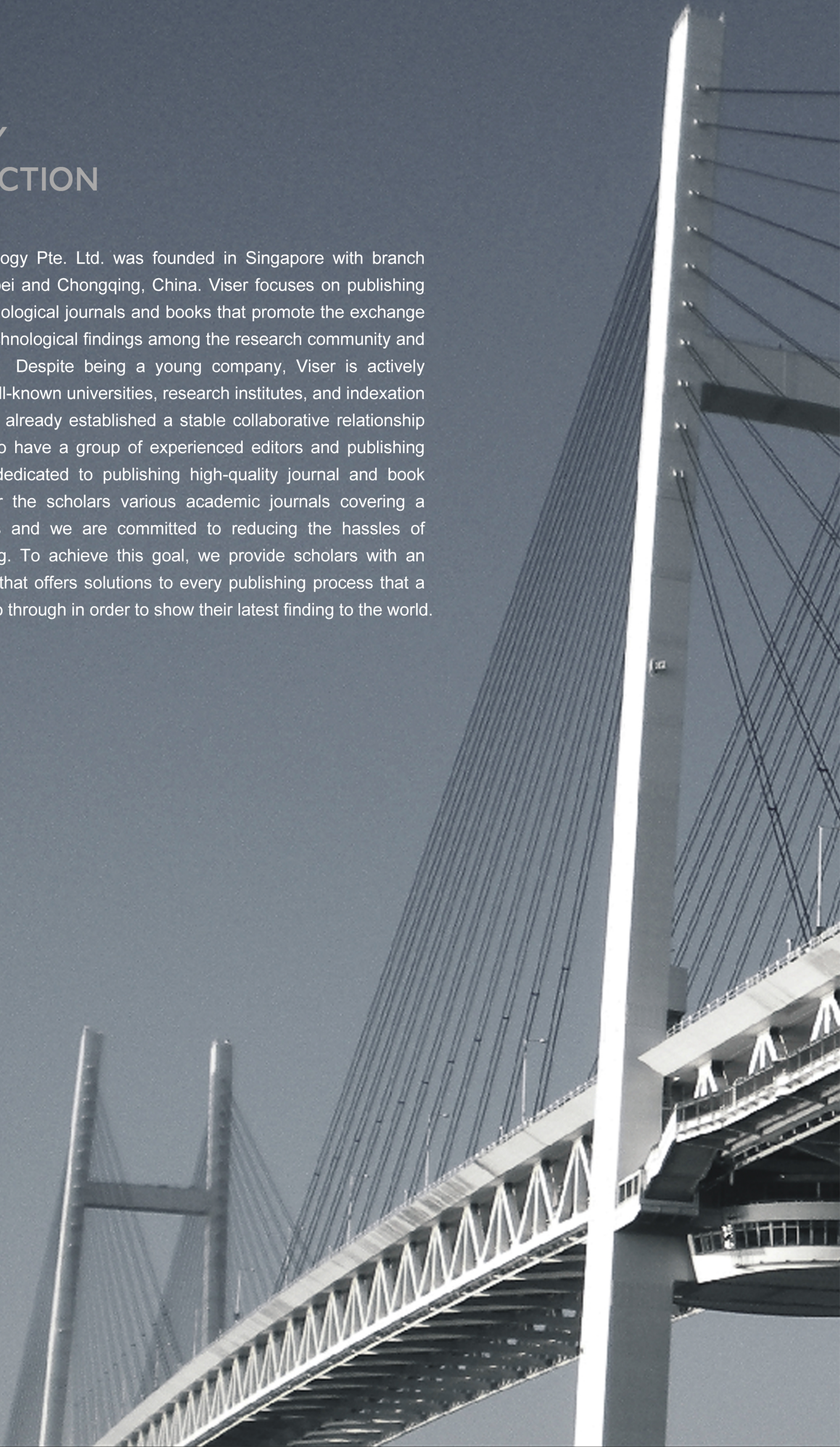

Research and Application of Materials Science

VISER

Publisher: Viser Technology Pte. Ltd.

ISSN: 2661-4464(online)
2661-4456(print)

Frequency: Semi-annual

Add.:21 Woodlands Close, #08-18,
Primz Bizhub SINGAPORE (737854)

https://www.viserdata.com/

Editors:

Yajun Lian
John Wilson
Mart Chen
Debra Hamilton
Jennifer M Dohy
Edward Adam Davis
Yanli Liu
Nike Yough
Qiuyue Su
Xin Di
Xiuli Li
Liangjun Qiu

Designer: Anson Chee

Research and Application of Materials Science

Volume 2 No.1 (2020)

CONTENTS

VISER

Viser Technology Pte. Ltd.
Research and Application of Materials Science
doi: 10.33142/msra.v2i1.1972

Review Article Open Access

Superhydrophobic Light Alloy Materials with Corrosion-Resistant Surfaces

Xiaowei XUN, Rili ZHU, Jiaojiao DONG, Ting PAN, Meiling ZHONG, Richao ZHANG, Dongmian ZANG*

School of Materials Science and Engineering, East China Jiaotong University, Nanchang 330013, P. R. China

***Corresponding Author:** Dongmian ZANG, School of Materials Science and Engineering, East China Jiaotong University, Nanchang 330013, P. R. ChinaE-mail address: zdmian@iccas.ac.cn*

Abstract:
Metals and their alloys are irreplaceable engineered materials showing great importance in our society. Light alloy materials (i.e., Mg, Al, Ti, and their alloys) have tremendous application potential in the aerospace, automotive industries, and biomedical fields for they are lighter and have excellent mechanical properties. The corrosion of light alloys is ubiquitous and greatly restricts their utilization. Inspired by the natural anti-water systems, many new designs and conceptions have recently emerged to create artificial superhydrophobic surfaces with great potential for corrosion resistant of light alloy. This review firstly introduces the concept of superhydrophobicity and strategies of producing superhydrophobic surfaces to inhibit the corrosion of light alloys. In addition, we elaborate the durability of superhydrophobic light alloy materials for commercial and industrial applications, and present their anticorrosion mechanism in the corrosive media.

Keywords: *light alloys; superhydrophobicity; corrosion resistance; mechanical durability*

1. Introduction

Mg, Al, and Ti based alloys are light alloys materials, showing tremendous application potential for the aerospace, automotive industries, and biomedical engineering owing to their light weight, good ductility, and favorable specific strength [1-3]. However, the corrosion of light alloy is ubiquitous and imposes negative effect on the global economy and environment, which greatly restricts their utilization[4, 5]. Constructing a protective coating on the alloy surface is a common anti-corrosion strategy to isolate the substrate from corrosive liquids. There are so many techniques to prepare corrosion resistant coating for protecting the alloy materials from corrosion factors in the environment, such as organic coating[6], inorganic coating[7], and other composite coating[8]. However, most of the coatings are permeable in the corrosion media containing Cl^- leading to the corrosion failure of the substrate. Therefore, developing the robust waterproof coatings on light alloy surfaces can be a more effective mothed to protect the light alloy materials from corrosion.

Inspired by the superhydrophobic surfaces in nature, artificial superhydrophobic coatings have been extensively developed due to its unusual properties including self-cleaning, anti-fogging, anti-icing, and anti-biofilm[9]. Superhydrophobic surface with hierarchical structure and low surface energy significantly reduce the contact area between water and substrate showing little proneness to water. As such, constructing superhydrophobic metallic surfaces has been an effective strategy to prevent the alloys from being corroded[10].Unlike traditional corrosion-resistant coating, superhydrophobic coatings not only provide a barrier between water and alloy material surfaces, but also reduce the residence of excess corrosion solution on the alloy surfaces greatly enhancing capabilities of corrosion protection[11]. Superhydrophobic coatings have been successfully developed as protective films on the surfaces of light alloy materials.

This review briefly introduces the superhydrophobic surfaces in nature and presents the fundamental theories on superhydrophobicity and adhesion behavior. Then, we summarize the strategies for preparing superhydrophobic surfaces on light alloys, and suggest the corrosion protection mechanism for superhydrophobic metallic surfaces in corrosive solution and humid environment. Finally, we elaborate the durability of superhydrophobic corrosion-resistant light alloy materials.

2. Superhydrophobicity

The wettability of solid surface is important in many fields, which is governed by surface chemistry as well as surface architecture. In general, the superhydrophobicity as one of the special wetting phenomena on a certain solid surface, is characterized by apparent water contact angle (CA) greater than 150°[12]. The artificial superhydrophobic surface is attractive and has been applied in various fields. Bio-inspired approaches are necessary to well understand and create superhydrophobic surfaces[13, 14].

2.1 Natural Superhydrophobicity

There are lots of insects, plants, and animals with superhydrophobic surfaces in nature, and the superhydrophobicity is a remarkable superiority for these species to survive and evolve in their surroundings[15-17]. Superhydrophobic surfaces in nature can be divided into two types. One is a self-cleaning superhydrophobic surface with ultralow water adhesion such as lotus leaf. In 1997, Barthlott and Neinhuis discovered the superhydrophobic self-cleaning property of the lotus attributed to the microscale papillae incorporated into hydrophobic epicuticular wax[18] (figure 1a). Subsequently, many scientists deeply studied the self-cleaning superhydrophobic phenomenon of lotus leaf, and found that the micro/nanoscale hierarchical structure and hydrophobic epicuticular wax responsible for the self-cleaning property[19].

The other is the high-adhesion superhydrophobic surface represented by rose petal (figure 1b). Compared to the self-cleaning lotus leaves, rose petals usually keep the spherical water droplet sticking on their surfaces. As such, the small water droplets are prone to pinning on the surface, while the larger ones roll off like raindrops. To reveal the origin of this strong adhesion on the superhydrophobic surface, Feng et al. studied the microstructure of the rose petal[20]. They found that the rose petal surface consists of many micro-papillae with a sea of nanoscale creases at the top of each micro-papilla. This superhydrophobic surface with high CA hysteresis could be illuminated by a impregnating Cassie state: water penetrating into the micro-papillae, and air gaps retaining in the nanoscale folds.

2.2 Wetting and superhydrophobic

Over the last few decades, scientists and engineers have intensely studied the wettability of solid surfaces and physical interactions between the solid and liquid. Young equation, Wenzel equation, and Cassie-Baxter equation are the principal equations in this field[21]. Young equation is the starting point for wetting state resulting from the equilibrium of interface tension along solid-liquid-vapor interfaces[22]. In this context, when the surface tension of water and its environments (usually air) are not changed, decreasing the surface tension of a solid material leads to increasing the static CA. Based on Wenzel equation, making roughness will increase both the hydrophobicity and hydrophilicity[23]. If the CA of the surface is greater than 90°, hydrophobicity is improved by roughness. As such, the surface structure is a critical factor for fabricating superhydrophobicity [24]. In 1944, Cassie modified the theory of wetting by introducing the concept of area fraction and explain the effect of surface roughness on the apparent CA and the improved hydrophobicity and hydrophilicity[25]. In the Cassie state, as the surface roughness is increased, the amount of air trapped in the grooves underneath the liquid is increased and thus the liquid cannot penetrate into the pores due to the trapped air.

Based on the existing wetting theory and superhydrophobic phenomena in nature, several superhydrophobic models have been proposed, which provide theoretical support for the preparation of superhydrophobic materials with specific functions[12]. As to the superhydrophobic surface with strong adhesion to water, the surface wetting state is Wenzel state. In Wenzel state (figure 1c), water droplets and substrates are wet-contacted and the water droplet is sticking on the substrate surface, causing a high CA hysteresis. In this context, when the surface is turned upside down, the water droplet can not drop down from the surface, but adhere to the surface, like a water droplet on a rose petal, this unique wetting state is called the “petal” state. Measuring the difference between the advancing CA and the receding CA or directly measuring the sliding angle (SA) can illustrate the CA hysteresis, which is the reflection on the water adhere to the solid surface. Additionally, as shown in figure 1d, as the water droplets contact part of the rough structure, but not contact the substrate, this is considered as a transitional state between Wenzel and Cassie state.

However, the wetting state of superhydrophobic surface with low adhesion force to water is different and has two main types. In Cassie state (figure 1e), the water droplets hardly wet contact on solid surfaces and can roll well off substrates resulting from air trapped underneath the water droplets. In the case, the small SA greater than 10° can illuminate the wetting functional in Cassie state but not Wenzel state. In addition, the “lotus” state is a special wetting example in Cassie state, for a lotus leaf has the self-cleaning property with micro/nanoscaled hierarchical structures (figure 1f).

According to biological inspiration and the previous wetting theory, there are two ways to prepare superhydrophobic surfaces: one is to roughen the surface of low-surface-energy materials (hydrophobic materials), and the other is to modify the rough surface with low-surface-energy materials. While chemical composition and surface roughness are both two main factors to govern surface wettability, the most importance is making rough surface with micro-nano hierarchical structure for constructing the artificial superhydrophobic surface with low adhesion to water.

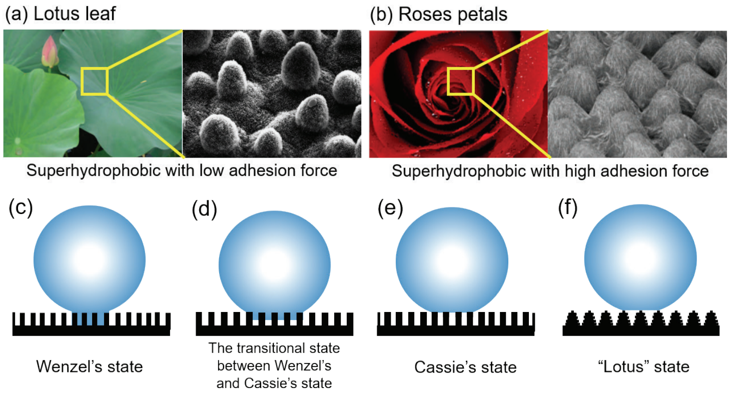

Figure 1. Natural superhydrophobic surfaces and their microstructures. (a) Lotus leaf show the superhydrophobic surface with ultralow adhesion due to randomly distributed micro-papillae covered by nanostructures[13]. Copyright 2008 Royal Society of Chemistry. (b) Red rose petals exhibit superhydrophobicity with strong adhesion and structural color resulting from periodic arrays of micro-papillae covered by nanofolds[20]. Copyright 2008 American Chemical Society. Different states of superhydrophobic surfaces: (c) Wenzel state, (d) the transitional superhydrophobic state between Wenzel and Cassie state, (e) Cassie superhydrophobic state, (f) the "lotus" state (a special case of Cassie superhydrophobic state)[12].

2.3 Fabrication of superhydrophobic surfaces on light alloy

For hydrophilic surface of light alloys, the strategy of constructing superhydrophobic surface is to construct a roughness with micro-nano hierarchical structure on the surface of light alloys (There are two main ways to construct roughness, one is bottom-up, that is to prepare a rough coating on the light alloy surface; the other is top-down by making rough structure by physicochemical method on light alloy), and then to reduce the surface energy to achieve superhydrophobic by chemical modification (long alkyl chain thiols, alkyl or fluorinated organic silanes, perfluorinated alkyl agents, long alkyl chain fatty acids, PDMS based polymers, or their combinations) (figure 2). Of course, these two steps can also be synthesized in one step. As such, various fabrication methods including physical, chemical, and combination of physical and chemical methods have been utilized to obtain superhydrophobic light alloy materials. Here, in this section, we will summarize the progress in the preparation of superhydrophobic light alloy materials and their corrosion resistant applications.

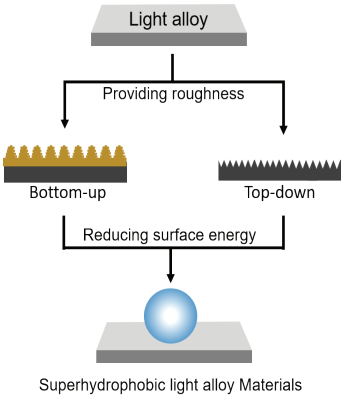

Figure 2. The strategies of producing superhydrophobic light alloy materials.

2.3.1 Etching

Etching is the most simple way to prepare rough surfaces on light alloys[26]. Etching method includes wet chemical etching, ion etching, plasma etching, and photolithography. Wet chemical etching is very common method for light alloys by immersing in chemical etchants and forms the micro/nanostructure surface with high roughness[27]. Then, the superhydrophobic light alloy material can be obtained by low surface energy film self-assemblied on the etching surface. Zang et al. etched Al sheets to achieve the high roughness by using HCl and then modified with stearic acid in N,N'-dimethylformamide (DMF)/water mixture[28]. The obtained Al alloy surface exhibited an excellent superhydrophobicity with high water CA 167.3° and corrosion resistant property. However, the chemical etching was carried out by using of various corrosive acids, which is dangerous and not environmentally-friendly[29, 30].

Recently, Photolithography is considered to be one of the most effective methods to fabricate a controllable surface roughness on the light alloy surface. Boinovich et al. reported a new efficient method based on nanosecond laser treatment for fabricating a superhydrophobic surface on Al alloys[31]. The results indicated that the surface roughness of Al alloy can be significantly increased and the morphology can be controlled. After laser etching, the surface of corrugations and grooves is a kind of fibrous and spherical oxide composed of nanoparticles. In addition, a thick oxide film with high roughness covered by nanoparticles will be formed after several stages of melting and solidifying (figure 3). The etched surface can chemically absorb a hydrophobic agent to obtain the superhydrophobic Al alloy surface with corrosion resistance. Moreover, there are reported strategy to fabricate superhydrophobic Al-Mg alloys with excellent mechanical and chemical properties by combining of functional nanoengineering and nanosecond laser texturing[32].

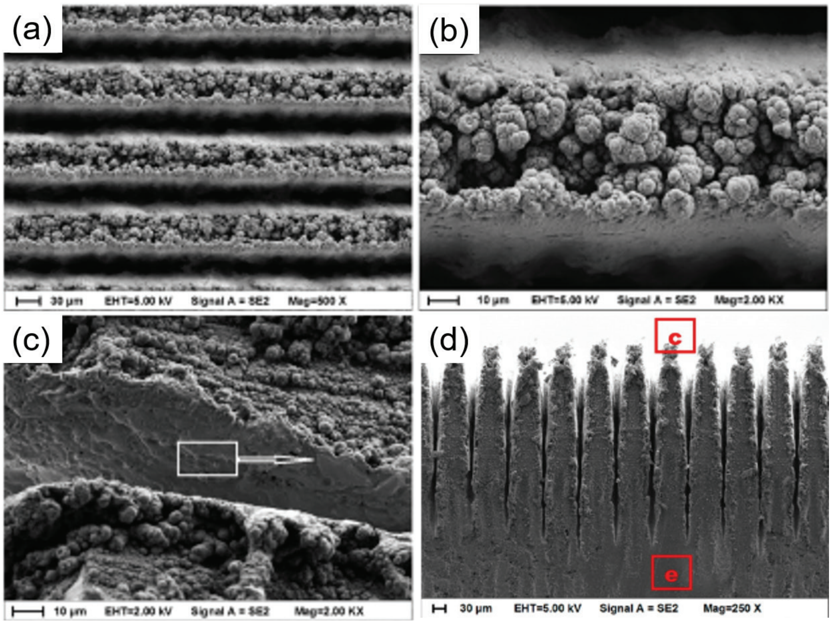

Figure 3. The superhydrophobic oxidized surface fabricated by photolithography on Al alloy[31]. The SEM images of the surface texture obtained by many-fold laser treatment (a, b) top view, (c, d) Side view. Scale bars are (a, d) 30 µm, (b, c) 10 µm. Copyright 2015 American Chemical Society.

2.3.2 Solution immersion

The solution immersion method is a convenient method for the growth of inorganic coating with rough micro-nanostructures on the surface of metal materials, which is inexpensive, environmentally-friendly, and easy to carry out[33, 34]. Qu et al. reported a solution immersion method for fabricating the superhydrophobic surfaces on different metals in a mixed-solution system[35]. The as-fabricated solution immersion superhydrophobic surfaces have long-time stability in corrosive liquids and can withstand various concentrations of salt solution. The excellent superhydrophobic surface is mainly attributed to the micro-nanometer structure made by solution immersion method. Furthermore, a superhydrophobic $Fe(OH)_3$ surface on Mg alloy made by solution immersion process was reported by Zang et al.. And the superhydrophobicity was obtained by stearic acid modified. The resulting superhydrophobic surface had largely improved corrosion resistance of the Mg alloy [36]. Liang et al. immersed the Mg alloy into $CuCl_2$ solution and stearic acid ethanol solution to fabrication a superhydrophobic surface with the CA of 154°[37]. The superhydrophobic Mg alloy surface exhibited excellent durability and corrosion resistance property. The solution immersion method is versatile since it can be applied to various metal materials with complex shapes and different sizes. However, the surface defects and coating adhesion force of solution immersion coating still need to addressed[38].

2.3.3 Hydrothermal

Similar to the solution immersion method, the hydrothermal method is another important bottom-up approach for fabrication of superhydrophobic corrosion proctection coatings on light alloys[39]. Different from the solution immersion method, the hydrothermal method is used to synthesize the coatings with micro-/nanostructure on the alloy surface under high temperature and/or pressure. In previous literatures, the superhydrophobic light alloy materials with micro-structured oxide or hydroxide layers was obtained by using hydrothermally treated and self-assembly of 1H,1H,2H,2H-perfluorooctyltriethoxysilane (PFOTES)[40]. As such, Feng et al. fabricated the superhydrophobic Mg alloy surface using an environment-friendly, facile, and cost-effective one-step hydrothermal process[41]. The as-prepared superhydrophobic Mg alloy surface with rough and hierarchical micro-/nanostructure exhibits excellent corrosion resistance and self-cleaning performance (figure 4).

2.3.4 Electrochemical

The electrochemical process can be employed to control surface morphology of light alloys, even on very large surfaces with various surface morphologies[42]. In this context, there are two strategies to fabricate superhydrophobic surface by electrochemical process. The first is the anodization processes, the anodizing method is one of the well-established electrochemistry to form the oxide layer with micro-nanoscale roughness on the metal surface, which is used for the preparation of superhydrophobic surface. The obtained anodization superhydrophobic surfaces have strong adhesion between the coating and the substrate and have wide applications[43]. Vengatesh et al. reported a superhydrophobic anodic aluminum oxide surface by using anodization process for corrosion protection of Al alloy[44] (figure 5a). The prepared aluminum anodizing film not only has strong surface adhesion to the substrate, but also is important to fatty acids grafting ensuring the stability of superhydrophobic surface with good corrosion resistance.

Secondly, the electrodeposition is a bottom-up approach for depositing the metal and/or metal oxide onto various conductive substrates[45, 46]. It is an effective technique for fabricating high roughness coatings on various substrates, for it can easily form micro-nanostructures by adjusting the electrodeposition parameters. He et al. fabricated the superhydrophobic surfaces with dendritic structures on Ti6Al4V surface by using electrodeposition[47] (figure 5b). The superhydrophobic coating with dendritic hierarchical structure was constructed by electrodepositing and annealing and displaying superhydrophobicity and low adhesion to water because of complex micro/nanostructures.

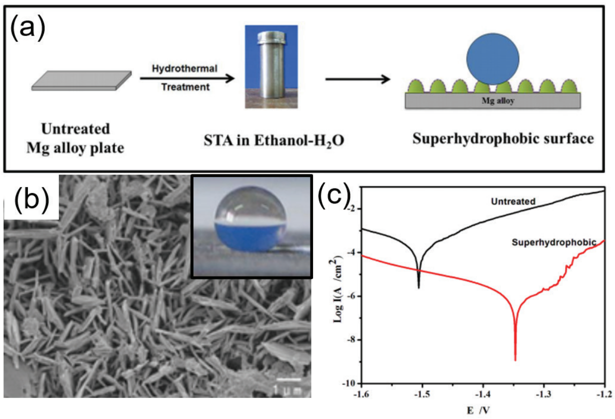

Figure 4. The superhydrophobic surface prepared by hydrothermal process on Mg alloy[41]. (a) Schematic of the fabrication of superhydrophobic surface on Mg alloy with one-step hydrothermal process. (b) The SEM images of one-step hydrothermal coatings. (c) Corrosion behaviors of untreated and superhydrophobic surface fabricated by hydrothermal. Copyright 2017 Elsevier.

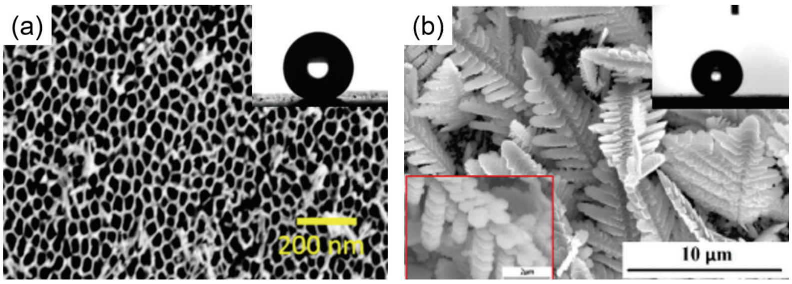

Figure 5. The surface morphologies and wetting behaviors of electrochemical superhydrophobic surface. (a) The SEM image and water CA of anodization superhydrophobic nanoporous Al_2O_3 surface[44]. Copyright 2015 American Chemical Society. (b) SEM images of electrodeposition superhydrophobic Zn/ZnO/TiO_2 surface on surface of Ti6Al4V. The inset is the water CA of corresponding surfaces[47]. Copyright 2017 Elsevier.

3. Durable Superhydrophobic Light Alloy Materials

3.1 Robust superhydrophobic light alloy materials

A myriad of reports have been published on fabricating superhydrophobic light alloy materials with corrosion resistant performance. However, the poor mechanical stability of microscopic surface structure has negative effect on the durability of superhydrophobic surface[48]. Mechanical wear on superhydrophobic light alloy materials usually leads to loss of water repellency property and makes the corrosion of the substrate more easily occur. In this context, the importance of superhydrophobic mechanical durability in applications should be addressed [49, 50].

As we all know, the stability of hierarchical structure on superhydrophobic surface is critically important to the robustness of superhydrophobic. Such hierarchical structure (submicron-sized nanobumps superimposed over microscale roughness) more durable than nanostructure surface[51]. Therefore, it is worth to note that the roughness of superhydrophobic surface should be optimized in the process of preparing superhydrophobic surface to improve its mechanical robustness. Luo et al. reported a superhydrophobic surface which has the robust mechanical durability because of the flexible coral-reef-like hierarchical structure[52] (figure 6). The durability of hierarchical architectures is attributed to the flexible coral-reef-like structure constructed by kinetic spray process. And the self-similar manner of the fluorinated wear-resistant porous oxide layer makes the obtained superhydrophobic coating has good water repellency. Based on combination of the above two strategies, the Cu-based superhydrophobic coating maintains its superhydrophobicity after various harsh mechanical testings. Particularly, the cushion effect of the coral-reef-like hierarchical structure could greatly minimize the mechanical damage from the environment to prevent the loss of superhydrophobic.

Most of the materials are conventionally hydrophilic, so a hydrophobic coating is required to make a superhydrophobic surface. However, the obtained traditional superhydrophobic surface has a disadvantage that the hydrophobic film has poor interface bonding force and rough structure is unstable, which results in the exposure of hydrophilic material after mechanical abration[48]. Then the water sticks to the tops of the abraded surface and the superhydrophobicity is lost. An effective way to deal with the above problem is to prepare the roughness on light alloys by using robust hydrophobic materials. Peng et al. presented all-organic, flexible, and multi-fluorination superhydrophobic nanocomposite coatings, which has strong substrate adhesion and excellent mechanical and chemical robustness[53] (figure 7). The robustness of the superhydrophobic nanocomposite coatings was resultant from a namely multi-fluorination strategy. The epoxy resin, perfluoropolyether, and fluoropolymer nanoparticles give rise to the stable hierarchical hydrophobic structure and help the surface energy, flexibility, and robustness to remain. As such, multi-fluorination coatings can retain superhydrophobicity even subjected to mechanical abrasion.

3.2 Self-healing superhydrophobic light alloy materials

Natural superhydrophobic surface can sustain their permanent water repellency and withstand damage because of their continuous repairing ability. Therefore, the self-healing superhydrophobic coatings have gained widespread interest, which can self-repair the damage caused by external factors and increase the durability of artificial superhydrophobic surface[54]. In addition, the self-healing superhydrophobic coating can ensure the durability of the hydrophobic property of the coating and protect the light alloy substrate from corrosion. Zhang et al. fabricated a self-healing superhydrophobic coating on Mg alloy from a eutectic solvent containing Cr (III)[55] (figure 8). The self-healing superhydrophobic coating was composed of Cr_2O_3 hierarchical microstructure and stearic acid modified layer. The smart superhydrophobic coating had shown excellent corrosion resistance in the NaCl aqueous solution due to the dual corrosion protect function. Compared with the traditional superhydrophobic coating, the second corrosion barrier of self-healing superhydrophobic coating is impressive. When the superhydrophobic coating is destroyed in the corrosion medium, the activated self-healing ability can repair the damage and maintain the durable corrosion resistance.

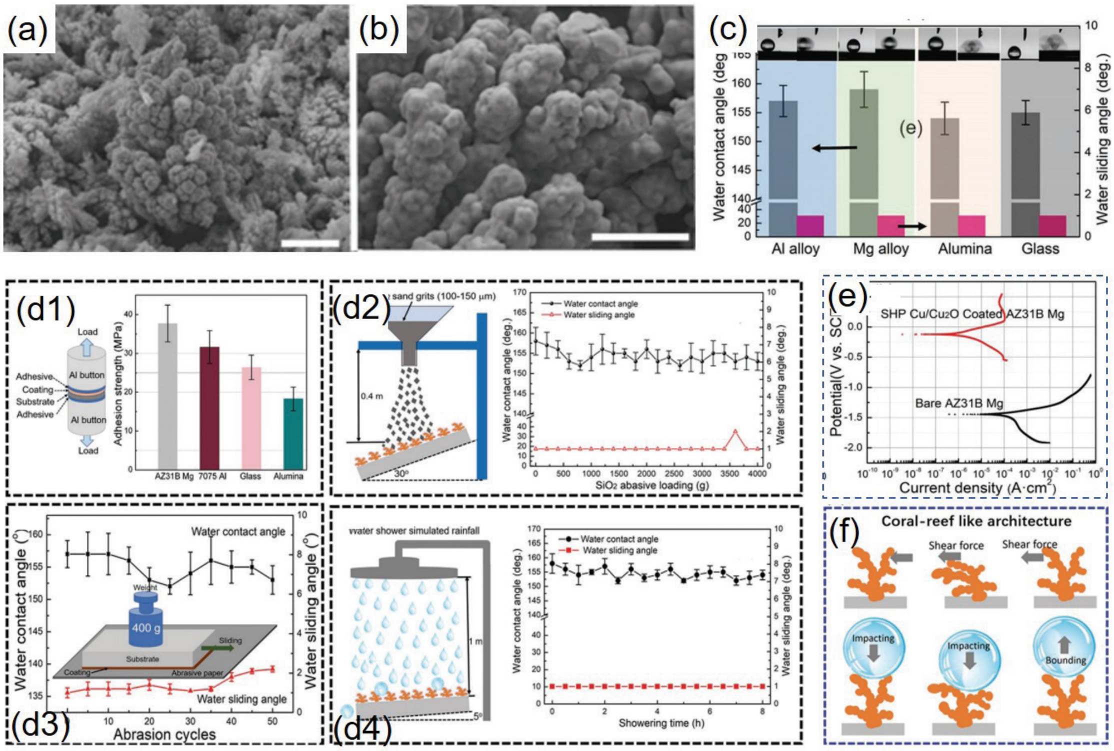

Figure 6. Superhydrophobic surface with a flexible hierarchical rough structure[52]: The surface topography of the flame-oxidized coating (a) and enlarged(b). (c) Superhydrophobicity on various substrates. (d) Mechanical robustness of the Cu-based superhydrophobic coating with flexible hierarchical rough structure. (e) Corrosion resistance test of Cu-based superhydrophobic coating. (f) Schematics showing the responses of flexible microstructure on Cu-based superhydrophobic coating to abration and impact. Copyright 2019 Wiley.

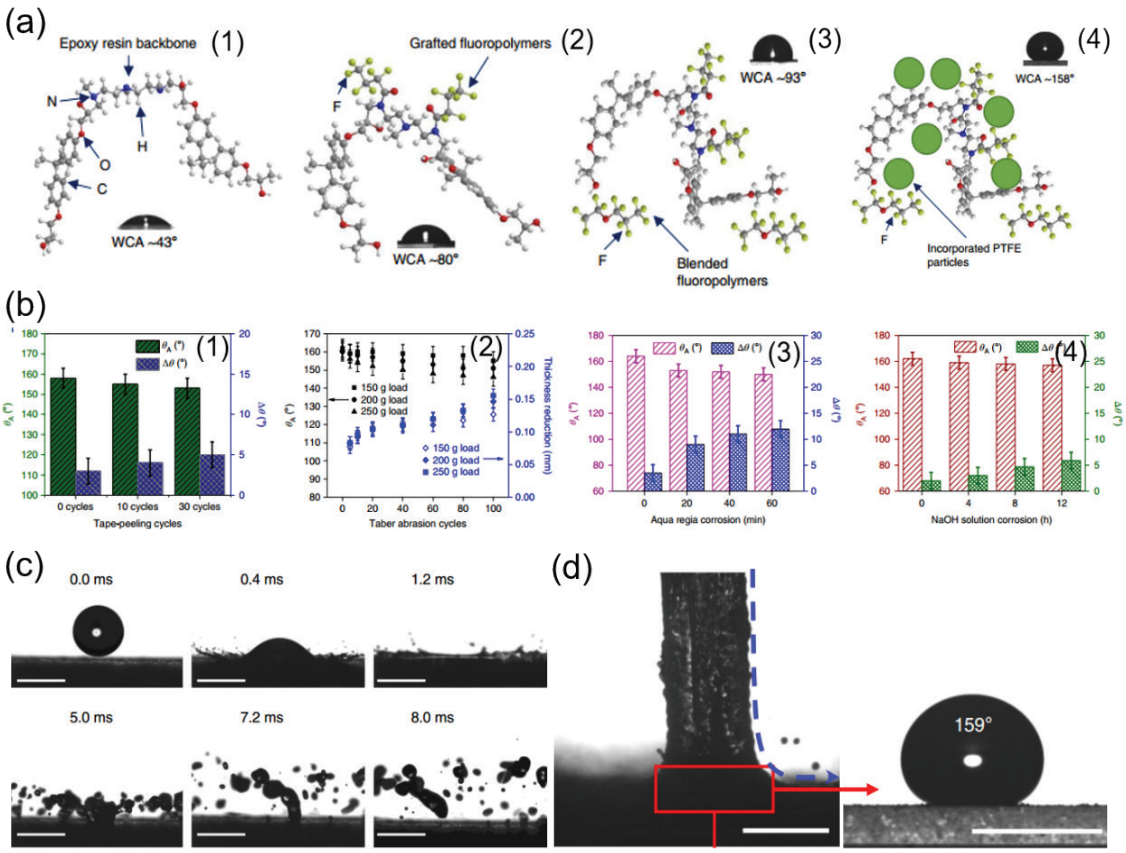

Figure 7. All-organic superhydrophobic coatings[53]: (a) Schematic illustration for the nanocomposite coating with the multi-fluorination strategy. (b) Mechanical robustness and chemical resistance of all-organic superhydrophobic coatings.A high-speed water jet test (c) and a water drop on the all-organic superhydrophobic coatings after water jet (d). Copyright 2018 Nature.

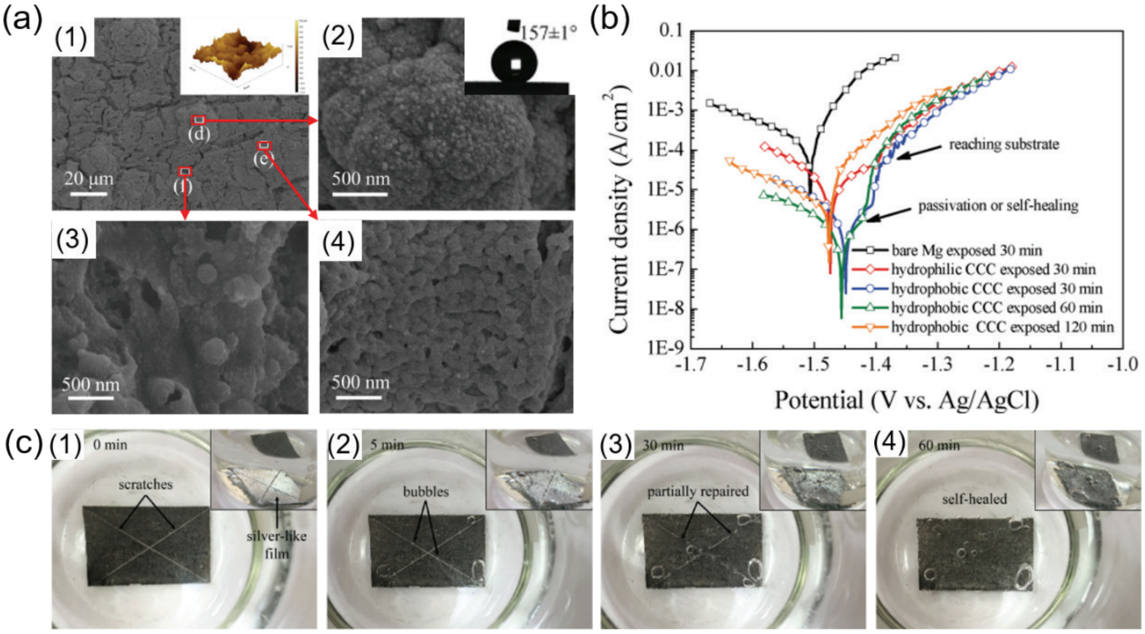

Figure 8. Self-healing superhydrophobic coating on Mg alloy[55]: (a) Surface morphologies and water CA of self-healing superhydrophobic coating. (b) Corrosion resistance of self-healing superhydrophobic coating. (c) The photos of self-healing capability of scratched self-healing superhydrophobic coating on Mg alloy. Copyright 2016 Wiley.

4. Application of Superhydrophobic Surfaces for Corrosion Protection

Metal corrosion is the depletion or destruction caused by the interaction between metal materials and the environment, which changes the original properties and resulting in the loss of its function as engineering materials[56]. Humidity, salt, acids, bases, and solvent are all factors causing corrosion of metal and/or its alloys in real environment. When the metal materials are exposed to corrosion environment and contact with those corrosion media, corrosion will take place on the surface and continues to spread rapidly in the materials.

Various surfaces and coating technologies have been proposed to achieve the corrosion resistance on the light alloy surfaces. Superhydrophobic surfaces on light alloy materials have shown remarkable corrosion-resistance in corrosive solution media during the past two decades[57]. Superhydrophobic coatings, like other coatings, provide a barrier on the surface of light alloys to effectively isolate the corrosion solution from the substrate. It is noted that superhydrophobic light alloy materials with hierarchical structure surface can trapped more air when immersed in the corrosive liquid, thus reducing the contact area between the corrosive solution and the materials surface and greatly reducing the corrosive media attacked to the substrate. The new effective mechanism for corrosion protection is provided[58, 59] (figure 9a). In addition, the self-cleaning properties of the superhydrophobic light alloy materials can also remove the corrosive medium on the surface and further reduce corrosion[60]. The superhydrophobic surface with low surface energy played irreplaceable roles in this process. On the other hand, the nanostructure of hierarchical rough structure on superhydrophobic light alloy materials is very important for preventing nanodroplets from pinning when exposed to humid environment. As can be seen in figure 9b, the condensed droplets are isolated from each other on the hierarchical structure and the electron transfer in the corrosion medium could be impeded, which inhibiting the electrochemical reaction and reducing the possibility of corrosion[61, 62].

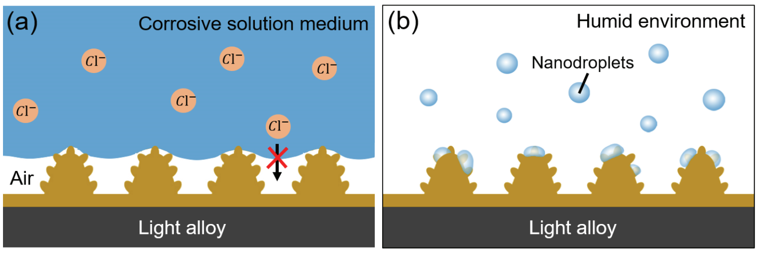

Figure 9. Illustration for corrosion protection of superhydrophobic light alloy materials in a corrosive solution medium (a) and humid environment (b). Copyright 2014 Elsevier.

In addition, different alloys have their own corrosion behaviors because of chemical and electrochemical properties. Mg based material is an active engineering material and has an aggressive driving force for corrosion. In a nature environment, the $Mg(OH)_2$ films on the surface of Mg and its alloys was formed, but they are poorly protective[63]. As such, it is necessary to fabricate a corrosion resistance coating for Mg and its alloys without sacrificing the favorable physical and mechanical properties. There are, however, many pores and cracks on the coated Mg alloy surface, which are difficult to avoid[64]. These defects provide a path for the penetration of corrosive medium and accelerate the corrosion of Mg alloys. Therefore, fabricating water-repellent coatings on Mg alloys has superiority to other systems for corrosion protection.

In the case of Al, the inherent corrosion resistance of Al and its alloy is attributed to its continuous surface oxide layer surface, which can significantly prevent internal corrosion of materials. However, the stable oxide layer on Al can be destroyed and made it extremely vulnerable to corrosion when exposed to strong acid, strong alkaline solutions or solution with aggressive anions. To compensate for the deficiency, preparation of ultralow adhesion superhydrophobic coatings on Al alloy is a promising technique to prevent the damage of oxide layer and materials corrosion [44]. Similarly, Ti and its alloy also have unusual corrosion resistant to alkali, chloride and some strong acids because of the compact oxide film formed spontaneously on surfaces. However, when Ti and its alloy encounter reductive oxygen and HF medium, the corrosion behavior are also arise. Superhydrophobic surfaces on titanium and its alloys can protect the metal materials from corrosion in harsh environment[65].

5. Summary

Making bioinspired superhydrophobic coating is an important method to protect light alloy materials from corrosion in previous studies. In this review, we have shown the researching progress in superhydrophobic light alloy materials with corrosion-resistant surfaces. We summarize the strategies of preparing bioinspired superhydrophobic light alloy materials based on the wetting theory. Superhydrophobic coating and air film trapped in hierarchical structure form double anti-corrosive barrier, which can greatly reduce the possibility of alloy substrate contacting with corrosive liquid and display superior corrosion resistance performances. Furthermore, mechanical durability is a central concern for superhydrophobic light alloy materials. Several studies have addressed this issue by improving the durability and/or possessing self-healing capability for superhydrophobic materials, which contribute to reduce the surface damage and prolong the lifetime of superhydrophobic surfaces.

Conflict of Interest: No conflict of interest was reported by the authors.

Acknowledgments: This work was supported by the National Natural Science Foundation of China (51863008, 51903084), the Natural Science Foundation of Jiangxi Province (20192BAB203008, 20192BAB206015).

References

[1] Ovari F, Tomcsanyi L, Turmezey T. Electrochemical study of the pitting corrosion of aluminum and its alloy— Ⅰ. Determination of critical pitting and protection potentions. Electrochimica Acta 1988; 33(3): 323-326.

[2] Gurrappa I. Characterization of titanium alloy Ti-6Al-4V for chemical, marine and industrial applications. Materials Characterization 2003; 51(2-3): 131-139.

[3] Ballerini G, Bardi U, Bignucolo R, et al. About some corrosion mechanisms of AZ91D magnesium alloy. Corrosion Science 2005; 47(9): 2173-2184.

[4] Devarayan K, Mayakrishnan G, Nagarajan S. Green inhibitors for corrosion of metals a review. Chemical Science Review and Letters 2012; 1(1): 1-8.

[5] Bonita D, Yeojin J, Jeongsoo S, et al. Review on corrosion behavior of metallic materials in room temperature ionic liquids International Journal of Electrochemical Science 2016; 11: 1482-1495.

[6] Voevodin N N, Grebasch N T, Soto W S, et al. An organically modified zirconate film as a corrosion-resistant treatment for aluminum 2024-T3. Progress in Organic Coatings 2001; 41: 287-293.

[7] Sidky P S, Hocking M G. Review of inorganic coatings and coating processes for reducing wear and corrosion. British Corrosion Journal 1999; 3: 171-183.

[8] Chou T P, Chandrasekaran C, Limmer S J, et al. Organic-inorganic hybrid coating for corrosion protection. Journal of Non-Crystalline Solids 2001; 290: 153-162.

[9] Zhang X, Shi F, Niu J, et al. Superhydrophobic surfaces: from structural control to functional application. Jounal of Materials Chemistry 2008; 18(6): 621-633.

[10] Zhang F, Zhao L, Chen H, et al. Corrosion resistance of superhydrophobic layered double hydroxide films on aluminum. Angewandte Chemie International Edition 2008; 47(13): 2466-2469.

[11] Wang P, Zhang D, Lu Z. Advantage of super-hydrophobic surface as a barrier against atmospheric corrosion induced by salt deliquescence. Corrosion Science 2015; 90: 23-32.

[12] Wang S, Jiang L. Definition of Superhydrophobic States. Advanced Materials 2007; 19(21): 3423-3424.

[13] Su B, Tian Y, Jiang L. Bioinspired interfaces with superwettability: From materials to chemistry. Journal of the American Chemical Society 2016; 138(6): 1727-1748.

[14] Darmanin T, Guittard F. Recent advances in the potential applications of bioinspired superhydrophobic materials. Journal of Materials Chemistry A 2014; 2(39): 16319-16359.

[15] Wang S, Liu K, Yao X, et al. Bioinspired surfaces with superwettability: new insight on theory, design, and applications. Chemical Reviews 2015; 115(16): 8230-8293.

[16] Zang D, Zhu R, Zhang W, et al. Corrosion-resistant superhydrophobic coatings on Mg alloy surfaces inspired by lotus seedpod. Advanced Functional Materials 2017; 27(8): 1605446.

[17] Lu X, Cai H, Wu Y, et al. Peach skin effect: A quasi-superhydrophobic state with high adhesive force. Science Bulletin 2015; 60(4): 453-459.

[18] Barthlott W, Nieinhuis C. Purity of the sacred lotus, or escape from contamination in biological surfaces. Planta 1997; 202: 1-8.

[19] Feng L, Li S, Li Y, et al. Super-hydrophobic surfaces: Frim natural to artificial. Advanced Materials 2002; 14: 1857-1860.

[20] Feng L, Zhang Y, Xi J, et al. Petal effect: A superhydrophobic state with high adhesive force. Langmuir 2008; 24: 4114-4119.

[21] Whyman G, Bormashenko E, Stein T. The rigorous derivation of Young, Cassie–Baxter and Wenzel equations and the analysis of the contact angle hysteresis phenomenon. Chemical Physics Letters 2008; 450(4-6): 355-359.

[22] Young T. An essay on the cohesion of fluids. Philosophical transactions of the royal society of London 1805; 95(95): 65-87.

[23] Wenzel R N. Resistance of solid surfaces to wetting by water. Industrial & Engineering Chemistry 1936; 28(8): 988-994.

[24] Callies M, Quéré D. On water repellency. Soft Matter 2005; 1(1): 55-61.

[25] Cassie A B D, Baxter S. Wettability of porous surfaces. Transactions of the Faraday society 1944; 40: 546-551.

[26] Wang Y, Gu Z, Xin Y, et al. Facile formation of super-hydrophobic nickel coating on magnesium alloy with improved corrosion resistance. Colloids and Surfaces A: Physicochemical and Engineering Aspects 2018; 538: 500-505.

[27] Huang Y, Sarkar D K, Grant Chen X. Superhydrophobic aluminum alloy surfaces prepared by chemical etching process and their corrosion resistance properties. Applied Surface Science 2015; 356: 1012-1024.

[28] Zang D, Zhu R, Zhang W, et al. Stearic acid modified

aluminum surfaces with controlled wetting properties and corrosion resistance. Corrosion Science 2014; 83: 86-93.

[29] Liu L, Xu F, Ma L. Facile fabrication of a superhydrophobic Cu surface via a selective etching of high-energy facets. The Journal of Physical Chemistry C 2012; 116(35): 18722-18727.

[30] Feng L, Zhang H, Wang Z, et al. Superhydrophobic aluminum alloy surface: fabrication, structure, and corrosion resistance. Colloids and Surfaces A: Physicochemical and Engineering Aspects 2014; 441: 319-325.

[31] Boinovich L B, Emelyanenko A M, Modestov A D, et al. Synergistic effect of superhydrophobicity and oxidized layers on corrosion resistance of aluminum alloy surface textured by nanosecond laser treatment. ACS Appllied Materials & Interfaces 2015; 7(34): 19500-19508.

[32] Boinovich L B, Modin E B, Sayfutdinova A R, et al. Combination of functional nanoengineering and nanosecond laser texturing for design of superhydrophobic aluminum alloy with exceptional mechanical and chemical properties. ACS Nano 2017; 11(10): 10113-10123.

[33] Liu Y, Lu G, Liu J, et al. Fabrication of biomimetic hydrophobic films with corrosion resistance on magnesium alloy by immersion process. Applied Surface Science 2013; 264: 527-532.

[34] Song J, Lu Y, Huang S, et al. A simple immersion approach for fabricating superhydrophobic Mg alloy surfaces. Applied Surface Science 2013; 266: 445-450.

[35] Qu M, Zhang B, Song S, et al. Fabrication of superhydrophobic surfaces on engineering materials by a solution-immersion process. Advanced Functional Materials 2007; 17(4): 593-596.

[36] Zang D, Zhu R, Wu C, et al. Fabrication of stable superhydrophobic surface with improved anticorrosion property on magnesium alloy. Scripta Materialia 2013; 69(8): 614-617.

[37] Liang M, Wei Y, Hou L, et al. Fabrication of a superhydrophobic surface on a magnesium alloy by a simple method. Journal of Alloys and Compounds 2016; 656: 311-317.

[38] Zhao L, Liu Q, Gao R, et al. One-step method for the fabrication of superhydrophobic surface on magnesium alloy and its corrosion protection, antifouling performance. Corrosion Science 2014; 80: 177-183.

[39] Zheng T, Hu Y, Zhang Y, et al. Formation of a hydrophobic and corrosion resistant coating on magnesium alloy via a one-step hydrothermal method. Journal of Colloid and Interface Science 2017; 505: 87-95.

[40] Ou J, Hu W, Xue M, et al. Superhydrophobic surfaces on light alloy substrates fabricated by a versatile process and their corrosion protection. ACS Applied Materials & Interfaces 2013; 5(8): 3101-3107.

[41] Feng L, Zhu Y, Wang J, et al. One-step hydrothermal process to fabricate superhydrophobic surface on magnesium alloy with enhanced corrosion resistance and self-cleaning performance. Applied Surface Science 2017; 422: 566-573.

[42] Darmanin T, Taffin de Givenchy E, Amigoni S, et al. Superhydrophobic surfaces by electrochemical processes. Advanced Materials 2013; 25(10): 1378-1394.

[43] Wang D, Wang X, Liu X, et al. Engineering a titanium surface with controllable oleophobicity and switchable oil adhesion. Journal of Physical Chemistry C 2010; 114: 9938-9944.

[44] Vengatesh P, Kulandainathan M A. Hierarchically ordered self-lubricating superhydrophobic anodized aluminum surfaces with enhanced corrosion resistance. ACS Appllied Materials & Interfaces 2015; 7(3): 1516-1526.

[45] Wang H, Zhu Y, Hu Z, et al. A novel electrodeposition route for fabrication of the superhydrophobic surface with unique self-cleaning, mechanical abrasion and corrosion resistance properties. Chemical Engineering Journal 2016; 303: 37-47.

[46] Zhang B, Zhao X, Li Y, et al. Fabrication of durable anticorrosion superhydrophobic surfaces on aluminum substrates via a facile one-step electrodeposition approach. RSC Advances 2016; 6(42): 35455-35465.

[47] He G, Lu S, Xu W, et al. Durable superhydrophobic Zn/ZnO/TiO_2 surfaces on Ti_6Al_4V substrate with self-cleaning property and switchable wettability. Ceramics International 2018; 44(1): 638-647.

[48] Verho T, Bower C, Andrew P, et al. Mechanically durable superhydrophobic surfaces. Advanced Materials 2011; 23(5): 673-678.

[49] Zhang D, Wang L, Qian H, et al. Superhydrophobic surfaces for corrosion protection: a review of recent progresses and future directions. Journal of Coatings Technology and Research 2015; 13(1): 11-29.

[50] Xuelin T, Tuukka V, Robin H. A. R. Moving superhydrophobic surfaces toward real-world applications. Science 2016; 352(6268): 142-143.

[51] Li W, Amirfazli A. Hierarchical structures for natural superhydrophobic surfaces. Soft Matter 2008; 4(3): 462-466.

[52] Luo X T, Li C J. Bioinspired mechanically robust metal-based water repellent surface enabled by scalable construction of a flexible coral-reef-like architecture. Small 2019; 15(39): e1901919.

[53] Peng C, Chen Z, Tiwari M K. All-organic superhydrophobic coatings with mechanochemical robustness and liquid impalement resistance. Nature Materials 2018; 17(4): 355-360.

[54] Xue C-H, Ma J-Z. Long-lived superhydrophobic surfaces. Journal of Materials Chemistry A 2013; 1(13): 4146-4161.

[55] Zhang J, Gu C, Tong Y, et al. A smart superhydrophobic coating on AZ31B magnesium alloy with self-healing effect. Advanced Materials Interfaces 2016; 3(14): 1500694.

[56] Montemor M. Functional and smart coatings for corrosion protection: a review of recent advances. Surface and Coatings Technology 2014; 258: 17-37.

[57] Vazirinasab E, Jafari R, Momen G. Application of superhydrophobic coatings as a corrosion barrier: A review. Surface and Coatings Technology 2018; 341: 40-56.

[58] Cui L-Y, Fang X-H, Cao W, et al. In vitro corrosion resistance of a layer-by-layer assembled DNA coating on magnesium alloy. Applied Surface Science 2018; 457: 49-58.

[59] Zhang D, Li L, Wu Y, et al. One-step method for fabrication of bioinspired hierarchical superhydrophobic surface with robust stability. Applied Surface Science 2019; 473: 493-499.

[60] Zheng S, Li C, Fu Q, et al. Development of stable superhydrophobic coatings on aluminum surface for corrosion-resistant, self-cleaning, and anti-icing applications. Materials & Design 2016; 93: 261-270.

[61] Michael N, Bhushan B. Hierarchical roughness makes superhydrophobic states stable. Microelectronic Engineering 2007; 84(3): 382-386.

[62] Wang N, Xiong D. Superhydrophobic membranes on metal substrate and their corrosion protection in different corrosive media. Applied Surface Science 2014; 305: 603-608.

[63] Song G, Atrens A. Understanding magnesium corrosion—A framework for improved alloy Performance. Advanced Engineering Materials 2003; 5(12): 837-858.

[64] Chu Q, Liang J, Hao J. Facile fabrication of a robust superhydrophobic surface on magnesium alloy. Colloids and Surfaces A: Physicochemical and Engineering Aspects 2014; 443: 118-122.

[65] Ou J, Liu M, Li W, et al. Corrosion behavior of superhydrophobic surfaces of Ti alloys in NaCl solutions. Applied Surface Science 2012; 258(10): 4724-4728.

Viser Technology Pte. Ltd.
Research and Application of Materials Science
doi: 10.33142/msra.v2i1.1973

Research Article Open Access

Research Progress of Ceramic Metallization Technology

Yang XIANG [1]*, Xuechong XIONG [2]*, Jin WEN [2], Guangyao ZHAO[3], Zhihang PENG[1], Feng CAO[1]

1 Science and Technology on Advanced Ceramic Fibers and Composites Laboratory, College of Aerospace Science and Engineering, National University of Defense Technology, Changsha Hunan, 410073, P. R China
2 Hunan Provincial Key Laboratory of Fine Ceramics and Powder Materials, School of Materials and Environmental Engineering, Hunan University of Humanities, Science and Technology, Loudi Hunan 417000
3 China Construction Machinery Test Center, Changsha Hunan, 410073, P. R China

***Corresponding Author:** E-mail: 13873149543@163.com (Xiang Yang)*
***Co Author:** 591906841@qq.com (Xiong Xue-chong)*

Abstract:
Due to the wide application of ceramics in electronic device packaging, the performance of ceramic metallization layer directly determines the performance of the whole package device. This paper introduces the main preparation methods of ceramic metallization, discusses the influence of Mo powder size, metallization formula, sintering temperature and other factors on the performance of ceramic metallization layer prepared by activated Mo-Mn method, and introduces several kinds of methods that can be tested to test the performance of ceramic metallized sealing samples. A new research direction of Ceramic Metallization Technology in the advanced field is put forward.

Keywords: *ceramic-metal sealing; metallization of ceramics; preparation method*

1. Introduction

With the deepening of the information age, the rapid development of communication, microelectronics and other industries, high-frequency, high-power electronic devices gradually occupy the mainstream of the market. Ceramic materials are widely used in the packaging of electronic devices because of their extremely stable thermal, electrical and mechanical properties.

However, with the gradual improvement of market requirements, the improvement of ceramic packaging technology is becoming more and more important. The key of ceramic packaging technology lies in the connection between ceramics and metals. Due to the difference of properties between the two materials, there is no good infiltration between ceramics and metals. Therefore, the solution is to deposit or sinter a thin metal layer on the surface of ceramics, which is also called ceramic metallization. At the same time, the performance of ceramic metallization layer directly determines the performance of the whole package device. Ceramic metallization technology was first applied in Germany in 1935. In 1958, China officially studied ceramic metallization, and now has a large-scale industrial chain in Beijing, Shanghai, Hunan, Guangdong and other provinces and cities [1].

Since the development of Ceramic Metallization Technology, the main ceramic materials used in practical production and development and application are: Al_2O_3, SiC, AlN, BeO, BN, etc., of which SiC ceramic has high thermal conductivity, but its high dielectric constant and low insulation voltage limit its use in high frequency field; AlN ceramic has excellent electrical and thermal properties, and the material is hard, which can be used in harsh environment However, due to its complex preparation process and high cost, it greatly limits the large-scale development and application of AlN Ceramics. The characteristics of BeO ceramics are high thermal conductivity, its thermal conductivity can be very close to that of metal materials, and the dielectric constant of BeO is low, the dielectric loss is small, and the process adaptability is strong. However, due to the toxicity of BeO, the preparation process will cause certain impact on the environment The BN Ceramics have high thermal conductivity, the thermal conductivity almost does not change with the temperature, the dielectric constant and the insulation performance are also suitable, but the raw material CBN is expensive, and it is usually not used in large-scale civil production. Al_2O_3 ceramics is the most mature ceramic materials, its advantage is the price Low cost, excellent thermal shock resistance and electrical insulation performance, and the preparation technology is very mature, so it plays a leading role in the electronic ceramic industry.

In recent years, the development of ceramic metallization technology has been the concern of scholars at home and abroad. With the coming of 5g era, the research on Ceramic Metallization Technology will also usher in another round of peak. In this paper, ceramic metallization as the main research content, combined with the actual production process, the preparation method of ceramic metallization, the influence factors and other aspects on the performance of ceramic metallization layer are introduced.

2. Preparation method of ceramic metallization

The commonly used methods of ceramic metallization are Mo-Mn, activated Mo-Mn, direct bonded copper(DBC), active metal brazing(AMB) and magnetron sputtering.

2.1 Mo-Mn method

The metallized layer is obtained by adding a small amount of MnO powder and coating it on the surface of ceramic body with binder and sintering at high temperature. Cao Changwei et al. [2] used the Mo Mn metallization method of Al_2O_3 ceramics for reference to metallize the surface of AlN Ceramics after preoxidation. The ceramic layer, metallized layer and nickel layer are close, and the thermal diffusivity of AlN Ceramics is 3.8% higher than that of AlN Ceramics without preoxidation. The traditional Mo Mn method is suitable for alumina ceramics with high glass content and low alumina content.

2.2 Direct Bonded Copper method (DBC)

The technology of direct copper-clad method originates from oxide (such as Al_2O_3) ceramics. Its principle is that when the temperature is about 1066 ℃ (specifically lower than the melting point of copper 10-17 ℃), copper-oxygen will form a certain amount of eutectic liquid phase containing copper and oxygen, while the existence of eutectic liquid phase will wet the contact copper and ceramic surface, and react with Al_2O_3 at the same time, generate composite oxide as solder, making copper It can be closely connected with ceramics [3].

Zhai Tianlei et al. [4] metallized AlN Ceramics by hot pressing and direct copper coating respectively. When the intermediate phase of Al_2O_3 and Cu_2O exists in direct copper coating, the combination of Cu and AlN Ceramics is closer, which is about 4 times of that of hot pressing. The advantages of the direct copper-clad method lie in the excellent thermal conductivity of the ceramic substrate, the high bonding strength between the metal and the ceramic, and the strong processability [3].

2.3 Active Metal Brazing method (AMB)

AMB appears later than Mo Mn method, but because of its advantages such as simple process, high sealing strength and good structure repeatability, it has been one of the main methods of ceramic metal connection.

Active metal is selected as brazing filler metal in active alloy method, and active metal and ceramic are used to react, so that the two can be connected. At present, the active metals used are mainly Ti, on this basis, Ni based, Au based, Cu based active brazing filler metals are developed [5]. Xiong Liyuan [6] has successfully realized the connection between AlN Ceramics and oxygen-free copper based on the study of the influence of binder composition in Ag Cu Ti active solder paste on the performance of brazing layer, and the shear strength has reached 75.18MPa, which is slightly better than the product obtained by using imported brazing paste.

2.4 Magnetron sputtering method

Magnetron sputtering is a physical vapor deposition method. The main principle of magnetron sputtering is that electrons impact the target under the action of electric field, and the atoms or molecules on the target are deposited on the surface of the substrate. It is characterized by high film-forming rate, low substrate temperature and good adhesion, which can realize large-area coating. Xincl et al. [7] have deposited Ti / Mo bilayer film on the surface of Al_2O_3 ceramics by magnetron sputtering. After high-temperature sintering, the welding strength of the joint with Fe Ni Co is further improved. The welding strength is 69.9MPa, which is much better than the metallized samples at 900 ℃ and 1050 ℃ without obvious TiO.

2.5 Activated Mo-Mn method

Activated Mo Mn method was first improved by American L.H. LaForge on the basis of traditional Mo Mn method in 1956 [1]. In order to reduce the sintering temperature and improve the wettability of the glass phase, the appropriate activator was added into the metallized raw material. For the migration process of glass phase in the activated Mo Mn method, Professor Gao Longqiao put forward different opinions. From the unilateral migration of glass phase in the initial ceramics, he thought that in the activated Mo Mn method, the glass phase in the activator and the glass phase in the ceramics migrate with each other, and when the components of the two glass phases reach the same, the sealing effect of the metallized layer is the best [8]. Xun Yanhong et al. [9] studied the effect of paste of Mo Mn Ti Si Al System on the metallization of alumina ceramics. For 95% Al_2O_3 ceramics using the paste, the welding strength can reach 150MPa.

Activated Mo Mn process is the most mature and widely used ceramic metallization technology.

3. Analysis of factors affecting the properties of ceramic metallized layer

With the continuous development of materials, ceramic metallization technology will keep pace with the continuous progress. Although ceramic metallization technology has been diversified in production and development, there are still many problems for us to further study for these existing technologies. Next, the most widely used and relatively mature activated Mo Mn method will be taken as the research object, focusing on several factors affecting the properties of ceramic metallized layer prepared by activated Mo Mn method.

3.1 Particle size of powder

The effect of powder size on metallization layer is mainly concentrated on Mo powder size. The size of Mo powder particle size will greatly affect the sealing strength of the product. Compared with 3 μm Mo powder, the sealing strength of 1 μm Mo powder can be increased by more than one time, but the smaller the Mo particle size is, the better. In the production process, too fine Mo powder will produce agglomeration, increase viscosity, not easy to form, and the coating is easy to crack [10]. Cui Ying et al. [11] used dry grinding and wet grinding processes to treat Mo powder. The two processes can greatly reduce the particle size of Mo powder. The median particle size of wet grinding is D_{50} = 1.78 μm. the sealing strength of 95% Al_2O_3 ceramics metallized with this Mo powder has been greatly improved, reaching over 350MPa. Li Jingyun et al. [12] found that when fine Mo powder was used to prepare metallized layer, the second metallization process (i.e. nickel plating process) would produce nickel layer blistering, which may be due to the fact that the stress of fine Mo powder could not be effectively released during the sintering process, thus leading to nickel layer blistering. It is suggested that nickel coating and new electroplating process can effectively improve the foaming of nickel layer.

3.2 Metallization formula

The introduction of activator is the key of the whole activated Mo Mn method. Different activators have different effects on metallization. Among them, the "three elements" of activator proposed by Professor Gao Longqiao is generally accepted by domestic scholars. The "three elements" of activator refers to the introduction of three basic oxides MnO, Al_2O_3 and SiO_2 in the design of metallization formula. The function of different oxides in sintering is also different. MnO is used to reduce the viscosity of glass phase at high temperature, so as to promote the migration of glass phase; Al_2O_3 is used to improve the sealing strength and expand the metallization temperature range; SiO_2 can improve the wettability of the framework formed by Mo powder micro oxidation to glass phase, and improve the anti crystallization ability of glass phase [13]. In addition, the introduction of other activators can also improve the performance of metallized layer. Yang Xirui [14] respectively used Bao and ZrO_2 as activators to explore the influence of different activators on the metallized layer of alumina ceramics. The results showed that the tensile strength of the metallized layer could reach 138MPa when the content of Bao was 1.5wt%, and 121MPa when the content of ZrO_2 was 0.2wt%. The activation mechanism of the two activators was not the same. Huang Yigong et al. [15] Based on the ceramic metallization of calcium aluminum silicon high alumina ceramics, explored the role of different components in the activator. The research shows that when the mass ratio of SiO_2 to Mn is between 0.54-0.60, glass can be formed, Al_2O_3 will expand the scope of glass formation, and CaO can reduce the crystal phase in the activator melt.

3.3 Sintering temperature

Ceramic metallization can be divided into several different processes according to different sintering temperatures: low temperature below 1300 ℃, medium temperature from 1300 ℃ to 1450 ℃, high temperature from 1450 ℃ to 1600 ℃, and extra high temperature above 1600 ℃. Different temperatures have their own fields and characteristics [16]. If the sintering temperature is too low, the metallized paste will not form glass phase. If the temperature is too high, the glass phase will overflow to the surface of metallized layer, which will affect the plating and sealing strength. Koto White et al. [17] studied the influence of manganese glass on the sealing strength of the metalized layer, they found that the sintering temperature was also critical to the formation of the glass phase. In the low MnO glass(mass fraction is less than 32%), the average tensile strength varies with temperature rise, in the high MnO glass phase (mass fraction is higher than 43%), the average tensile strength of the highest when the sintering temperature is 1300 ℃, 1450 ℃ in the tensile strength decreased, while the main reason is that 1350 ℃ high MnO glass phase alumina crystal growth affected the tensile strength. Huang Yigong et al. [18] through the research on the influence of wet hydrogen on the quality of metallized layer in BTU horizontal hydrogen furnace, found the cause of the blackening of ceramic glaze layer in the process of ceramic metallization, analyzed the influence of water vapor content in wet hydrogen on the quality of metallized layer, and provided an important idea for improving the strength of metallized layer. Zhong Wei et al. [19] simulated and calculated the instantaneous temperature in the high-temperature hydrogen furnace by establishing the three-dimensional flow and heat transfer mathematical model of alumina ceramic metallization process. The results show that the maximum temperature difference in different positions of the high-temperature hydrogen furnace is 26 ℃, and the setting temperature for metallization is generally low, which also provides an important basis for optimizing the hydrogen furnace structure and further improving the temperature uniformity of the hydrogen furnace. Accurately controlling the sintering process is the key to the success of the ceramic metallization layer. Only fully considering the influence of sintering temperature and other factors on the formation of the metallization layer, can the ceramic metallization layer with better performance be prepared.

3.4 Others

Microstructure：Microstructure directly affects the bonding strength and air tightness of ceramic metal materials. Through the study of microstructure, it can play a guiding role in improving components and optimizing process. The section layer of weldment with better welding performance should be clear. Only when the interface of each interface layer is clear can it be proved that the interface layers are firmly connected by chemical bonding, without forming a fragile middle layer or being damaged. If the structure of the metallized layer is loose, the Ni layer or the solder layer will enter into the metallized layer, which will affect the welding strength, and the air will be released under vacuum due to the poor air tightness [20].For ceramic matrix, the matrix porosity and pore diameter size also influences the glass phase diffusion, manganese content in the aperture size of glass phase manganese content in the capillary force is the main driving force, porosity is directly affecting the manganese content in the matrix of the absorption rate of glass phase, and glass phase content in the matrix affects the manganese content of glass phase diffusion depth, so the metallized layer of organization evolution and mechanics performance change is also affected by the matrix microstructure[21].

Coating method：Coating methods affect the uniformity of metallized paste coating. The existing coating methods mainly include manual coating, screen printing, spray gun spraying, etc. For products with relatively small quantity and inconsistent size and scale, manual coating should be adopted, while for large-scale factory production, screen printing process is generally adopted, with good coating uniformity and basically consistent product thickness. The coating thickness should be 50 μm [22].

Organic components：In the coating process of generic paste, in order to ensure that it has certain process performance: viscosity, rheology, thixotropy, plasticity, etc., it is necessary to add appropriate and appropriate amount of binder, diluent, thixotropic agent, plasticizer and other organic compounds. For different coating methods, the composition of organic matter is different. The paste for manual coating is made of nitric acid fiber as binder, amyl acetate as solvent, and the viscosity of the paste is 1.20-1.40Pa·s; the paste for screen printing is made of ethyl cellulose and terpineol (or ethanol, n-butanol) as solvent, and the viscosity of the paste is about 25Pa·s [1].

4. Performance test method of ceramic metallization

At present, the main testing methods for ceramic metallization are: metallographic microscopy, scanning electron microscopy (SEM) and X-ray fluorescence thickness gauge to observe the microstructure and thickness [23]; EDX energy spectrum analysis to detect the regional elements of metallization layer to understand the reaction process in the sintering process; X-ray diffraction to analyze the phase of metallization layer Test the tensile strength of sealing sample with electronic universal testing machine [24]; test the fatigue resistance of sealing sample with electro-hydraulic servo fatigue testing machine [25]; test the air tightness of sealing sample with helium mass spectrometer leak detector [26].

5. Summary

After decades of continuous development, the application field of ceramic metallization technology continues to expand, from semiconductor chips, auto parts, vacuum switches and other life-related fields to military radar, basic communication, new energy development and other important fields, ceramic metallization technology has gradually become the basis of its development. China's ceramic metallized sealing devices have gradually met the basic needs of the country, but we still need to carry out further research in the high-end field. There are still some problems in Ceramic Metallization Technology to be discussed:

(1) High power, high frequency electronic devices are the main direction of future development, so the development of better performance, higher quality sealing devices still need to be focused on;

(2) The optimization of technological process, the reduction of production energy consumption and production cost, and the realization of large-scale production of products are still to be explored;

(3) The formulation of product quality standards needs to be further improved.

The continuous improvement of ceramic metallization technology is the premise of the progress of ceramic metal sealing technology. I believe that with the continuous efforts of the industry, ceramic metal sealing technology will continue to move forward steadily.

Conflict of Interest: To the best of our knowledge, the productions of this paper are original. All authors have read the paper and agree to this statement of originality. Finally, this paper is our original unpublished work and it has not been submitted to any other journal for reviews. The authors have obtained the necessary authority for publication. If accepted, this paper will not be published elsewhere in the same form, in English or in any other language, without the written consent of the Publisher.

Acknowledgments: The authors are grateful to National Science Foundation of China (51602347) and Hunan Natural Science Foundation (2019JJ50282) for financial support. The authors are also grateful to Aid Program for Innovative Group of National University of Defense Technology and Aid Program for Science and Technology Innovative Research Team in Higher Educational Institutions of Hunan Province.

References

[1] Gao L Q, Liu Z. Progress of Ceramic to Metal Seal Technology in China[J].Shandong Ceramics,2019,42(02):7-12. (In Chinese)

[2] Cao C W, Feng Y B,Qiu T, Liang T. Surface Oxidation and Metallization of AlN Ceramics by Mo-Mn Process[J]. Journal of Synthetic Crystals, 2017,46(03):416-421+432. (In Chinese)

[3] Chen D Q, Lin F, Xiao L R, Qiu T, Cai H P, Jiang X L, Yi D Q. Research and Development of DBC packaging Materials. 2004(06):76-78+82.(In Chinese)

[4] Zhai T L, Lin G A, Yao B, Ding M M, Xie J J, Shi Y Y, Li D S, Wu, Z H. Interface Bonding Properties and Microstructure of AlN/Cu Composite Substrate[J]. Journal of the Chinese Ceramic Society, 2017,45(07):1037-1042.(In Chinese)

[5] Wang Y, Cao J, Zhang L X, Feng J C. Review on active brazing of alumina ceramic and metal[J], Welding & Joining,2009(02):56-60+71.(In Chinese)

[6] Xiong L Y. Preparation and Characterization of Ag-Cu-Ti Active Paste for Brazing[D], Nanjing University of Aeronautics and Astronautics, 2018.(In Chinese)

[7] Xin C L, Liu W B, Li N, et al. Metallization of Al2O3 ceramic by magnetron sputtering Ti/Mo bilayer thin films for robust brazing to Kovar alloy [J]. Ceramics International, 2016,42(8):9599-9604.

[8] Gao L Q, Gao Y Q. Total Process of Glass Phase Migration in Ceramic Metallization[J]. Shandong Ceramics, 2010,33(04):3-5+16.(In Chinese)

[9] Xun Y H, Zhang J X, Chen M L, Gao L Q. Processing of Metallizing Alumina Ceramic with Mo-Mn-Ti-Si-Al System Paint[J]. Vacuum electronics, 2011(01):26-29.(In Chinese)

[10] Gao L Q. Molybdenum Powder and Ceramic Metallizing Technology[J]. Vacuum Electronics, 2012(04):1-5+15.(In Chinese)

[11] Cui Y, Can A F, Chen X H, Huang Y G. The Influence of Mo Powders on Metallizing[J]. Vacuum Electronics,2013(04):88-91.(In Chinese)

[12] Li J Y, Zhao R F. Effects of the Fine Molybdenum Powder on the Quality of 95% Alumina Ceramics Metallizing and the Analysis of Existing Problems[J]. Vacuum Electronics, 2014(04):67-71.(In Chinese)

[13] Gao L Q. Design Principle of the Ceramic Metallizing Formulae[J]. Vacuum Electronics, 2002(03):21-23.(In Chinese)

[14] Yang X R. Preparation and Properties of Metallization Layer used for Packaging Transistors, Shandong University,2016.(In Chinese)

[15] Huang Y G, CaiA F, Liu Y Q, Liu H Q. Various Components of Activating Agent for Molybdenum Manganese Metallization Play the Role in the Formulation[J]. Vacuum Electronics, 2008(04):42-46+59.(In Chinese)

[16] GAO L Q, Recent Development of Ceramic to Metal Seal and Its Relative Technology[J]. Vacuum Electronics, 2000(05):20-26.(In Chinese)

[17] KOTO WHITE, Daniel P. KRAMER. Microstructure and Seal Strength Relation in the Molybdenum-Manganese Glass Metallization of Alumina Ceramics[J]. Materials Science and Engineering, 1985,75(1-2):207-213.

[18] Huang Y G, Liu X F, Liu H Q, The Influence of Hydrogen Humidity on Product Quality of Ceramic Metallization[J]. Vacuum Electronics, 2010(02):54-58.(In Chinese)

[19] Zhong W, Zou G J. Modeling and Simulation of Temperature Field in Al2O3 Ceramic Metallization[J]. 2016,36(06):718-722.(In Chinese)

[20] Zhang J X. Microstructure of Metallized Alumina Ceramics Applied in Vacuum Electronics Comp onents of Domestic and Oversea[J]. Vacuum Electronics, 2003(04):27-28+39.(In Chinese)

[21] Wang L, Kang W T, Guo P Z, et al. Influence of Ceramic Substrate Porosity and Glass Phase Content on the Microstructure and Mechanical Properties of Metallized Ceramics via an Activated Mo-Mn method [J]. Ceramics International, 2020,46(6):8244-8254.

[22] Wang L, Kang W T, Gao P Z, Kang D H, Zhang H H. Research Progress of Methods, Mechanisms and Influencing Factors of Ceramic Metallization[J]. Journal of Ceramics, 2019,40(04):411-417.(In Chinese)

[23] Cheng W Q, Chen J H. Analysis and Discussion on Measuring the Thickness of Ceramic Metallization Layer with Different Testing Equipment[J]. Ceramics Science & Art, 2010,(10):18-20.(In Chinese)

[24] Cheng W Q. Test and Application of Ceramic-Metal Sealing Tensile Strength[J]. Ceramics Science & Art, 2006(02):4-6.(In Chinese)

[25] Shi M, Zheng J X, Gao L Q, Liu Z. Study on Fatigue Behaviors of Metalized Al2O3 Ceramic Seals[J]. Bulletin of The Chinese Ceramic Society, 2012,31(04):1035-1038.(In Chinese)

[26] Qi L J, Zheng J P, Lei H Z. Brazing Process and Application Performance of Monocrystal Al2O3 Ceramic/Nb-1Zr Alloy Sealing Parts[J]. Vacuum Electronics, 2016(01):58-63.(In Chinese)

Viser Technology Pte. Ltd.
Research and Application of Materials Science
doi: 10.33142/msra.v2i1.1974

Research Article Open Access

Three-dimensional Porous Graphene/Polyaniline Hybrids for High Performance Supercapacitor Electrodes

Zhaoxia HOU *, Peng SHI, Shengnan ZOU

Liaoning Province Key Laboratory of Micro-nano Materials Research and Development, School of Mechanical Engineering, Shenyang University, Shenyang 110044, China

***Corresponding Author:** Zhaoxia HOU, School of Mechenical Engineering, Shenyang University, Shengyang, 110044, P. R. China E-mail address:luckyxia2007@126.com*

Abstract:
Graphene-based composites took extensive attraction as electrodes for supercacitors these years. Three-dimensional cross-linking porous graphene (3D rGO-m) was obtained by KOH activation to graphene modified by 1,2,4-triaminobenzene. 3D porous graphene/polyaniline hybrids (3D rGO-m/PANI) was prepared by the in-situ chemical oxidative polymerization. The rGO-m are reconstructed from 2D to 3D porous structure after KOH activation. The PANI nanorod arrays are successfully decorated on the surface of the 3D porous graphene sheets. The specific capacitance of the 3D rGO-m/PANI hybrids reach 985 F/g at 0.5 A/g. The capacitance retention of 3D rGO-m/PANI maintains 90% of its initial capacity after 1000 cycles, while rGO-m/PANI only keeps 83% of its initial capacity, the cycling stability of both hybrids are higher than that of pure PANI (69%).

Keywords: *three dimension; porous graphene; polyaniline; hybrid materials; supercapacitor*

1. Introduction

Compared to conventional capacitors and Li ion batteries, supercapacitors with outstanding charge/ discharge rate and high power capability have attracted considerable research, and will become a promising energy storage device [1]. Electrodes, as the key materials in energy storage devices, determine the performance of the supercapacitors, such as capability, delivery rates and cycling stability [2].

Among carbon based materials, such as active carbon, carbon nanotube, graphene is a highly promising electrode material in Electric double layer capacitor (EDLC) due to its high electrical conductivity, high specific surface area, high charge mobility, favorable flexibility, and good mechanical strength [3]. However, graphene sheets are easy to aggregate due to the strong $\pi-\pi$ interaction. The aggregation of graphene makes the channels among the sheets so narrow that the electrolyte ions are unable to access [4]. Compared to 2D graphene sheets, 3D porous graphene structure can provide larger specific surface area, which will contribute larger contact interfaces between electrode and electrolyte, and provide three-dimensional paths for ionic or electronic transport as well, so 3D porous structure graphene is considered to have excellent electrochemical performance.

Polyaniline (PANI) with low cost, easy synthesis and high pseudocapacitance has become a promising pseudo supercapacitor electrode material. PANI with highly-ordered nanowire arrays are beneficial to facilitate ion transport by shorten transport paths [5]. However, the inevitable volume expansion and contraction during change/discharge will result in mechanical degradation and low cycling stability, which constraint its practical application [6]. So, it is put forward that combining PANI with graphene or other inorganic materials such as metals or metal oxides as scaffold or bracket to confine the volume changes of PANI, hybrid materials will possess both high capacitance and good cycling stability [7-11].

In this work, we proposed an effective method to prepare 3D porous graphene/PANI hybrid materials by KOH activation and in-situ chemical oxidative polymerization methods. Graphene was modified by 1,2,4-triaminobenzene, the modifier serves as molecular spacer that decreases greatly the stacking of the graphene sheets. Graphene modified (rGO-m) is of thin sheets and crumpled morphology. KOH activation was used to etch pores on the rGO-m sheets to construct 3D porous structural graphene (3D rGO-m), and then 3D porous structure rGO-m/PANI hybrid materials was obtained by in-situ polymerization. The microstructure, morphology and electrochemical performance of the 3D rGO-m/PANI hybrid materials were characterized and investigated. The 3D rGO-m/PANI hybrid materials showed high specific capacitance and good rate capability and cycling stability.

2. Experimental

2.1 Materials

Graphite powder (30 μm) was from Nanjing XFNANO Materials Tech Co., Ltd. Aniline (An, AR), ammonium persulfate (APS, AR) were from Tianjin Damao Chemical Agent Company. Sodium carbonate anhydrous (Na2CO3, AR) and potassium hydroxide (KOH, AR) were from Tianjin Bodi Chemical Engineering Corporation. 1,2,4-triaminobenzene dihydrochloride (96%) was from Alfa Aesar. All reagents were used directly without any treatment.

2.2 Preparation of 3D porous rGO-m/PANI hybrids

2.2a 3D rGO-m: Graphene oxide (GO) was prepared by a modified Hummers method according to the reference [12]. Graphene modified by 1,2,4- triaminobenzene (rGO-m) was prepared according to the reference [13]. rGO-m were soaked in aqueous KOH solution with the mass ratio of KOH:rGO-m=7 for 24 h, and then heat treated at 500 ℃for 5 h. After activation, samples were sequentially washed by acetic acid and deionized water and further dried at 60 ℃ for 12 h. Samples obtained are named as 3D rGO-m. In comparison, the rGO was synthesized via the same procedure as rGO-m but without 1,2,4-triaminobenzene.

2.2b 3D porous rGO-m/PANI hybrids: The 3D rGO-m/PANI hybrids were synthesized by in-situ chemical oxidative polymerization method with aniline as a monomer in the presence of 3D rGO-m. The procedures were as followed: 3D rGO-m was ultrasonically dispersed in 1 M HCl for 0.5 h, and aniline and polyving akohol with 1:0.000075 molar ration were added into 3D rGO-m suspension and performed another 0.5 h sonication and then decreased the temperature to 0 ℃. A certain amount of APS was dropped in and kept stirring at 0 ℃ for 8 h. The hybrid materials were filtered and washed repetitively with DI water and ethanol, until the filtrate became colorless. In order to comparison, pure PANI and inactivated rGO-m/PANI hybrids (marked as rGO-m/PANI) were synthesized, respectively, via the same procedures as reported above.

2.3 Materials Characterization

The electrodes were prepared by active materials with 10% binder (polytetrafluoroethylene, PTFE). The two-electrod system was assembled with a cellulose paper as separator, carbon fibre paper as current collector and 1M H_2SO_4 aqueous as electrolyte.

X-ray diffraction (XRD, PANalytical) was analyzed with Cu Kα radiation (λ = 0.15418 nm) from 5° to 60°. Foutier transform infrared spectrometer (FT-IR, Bruker EQUNOX 55) was recorded at room temperature from 400 cm^{-1} to 4000 cm^{-1} at a resolution of 2 cm^{-1}, KBr powder pellet. The microstructure was observed by the Field Emission Scanning Electron Microscope (FE-SEM, Hitachi S4800).

All the electrochemical performance was studied on a PARSTART 2237 electrochemical workstation. Cyclic voltammetry (CV) and electrochemical impedance spectroscopy (EIS) and galvanostatic charge-discharge (GCD) measurments were carried out in a two-electrode system. CV and GCD measurements were conducted within the potential range of 0–0.8 V. CV curves were tested at a scan rate of 5, 10, 25, 50 and 100 mV/s. GCD curves were set in the range from 0.01 Hz-100 kHz at different current densities.

The specific capacitance (Cs) of the active electrode material was determined from the GCD curves using the equation:

$$C_S = \frac{4I\Delta t}{m\Delta V} \qquad (1)$$

Where, I is discharge current (A), Δt is the discharging time (s), m is the total mass of active electrode material (g), and ΔV is the voltage drop (V) upon discharging (excluding the IR drop). The energy density E was calculated by

$$E = \frac{C_S \cdot \Delta V^2}{8} \qquad (2)$$

where the specific capacitance (Cs) was derived from GCD measurement. The same ΔV was used as that in Cs calculation from GCD. The power density P was calculated by

$$P = \frac{E}{\Delta t} \qquad (3)$$

where E referred to the energy density, Δt was the same as that in calculation of E.

3 Results and Discussion

3.1 Microstructure and morphology

After a hydrothermal reaction, rGO without modified appears flat and inter-stacked sheets under a FE-SEM (figure 1(a)).The rGO-m appears crumpled sheets (figure 1(b)). Some sheets are translucent, indicating that their thickness in the low side. The rGO-m with crumpled morphology suggests that the amino groups of 1,2,4-triaminobenzene are chemically bonded with grapheme, which results in the morphology change of the rGO-m sheets. Typical FE-SEM images of activated graphene samples of 3D rGO-m are shown in figure 1(c), it can be seen clearly that the sample activated by KOH is reconstructed from 2D to 3D structure, and highly porous morphology can be observed as well. Restructuring among carbon fragments is due to the dangling bonds resulted from KOH activation. In the activation process, the etching of rGO-m matrix via redox reaction between C and KOH leaves defects and planar pores, and produces graphene fragments with a lot of C dangling bonds. Thus, the restructure of graphene fragments occurs.

Pure PANI is random relatively long rod with 400 nm in length and 60 nm in diameter (figure 2(a)). The FE-SEM images of rGO-m/PANI shows the structure of rGO-m supported PANI nanorod arrays with 100 nm in length and 50 nm in diameter (figure 2(b)), and the rGO-m sheets are obviously visible. 3D rGO-m/PANI shows the similar structure with rGO-m supported PANI nanorod arrays, but owing to the 3D cross-linking structure of rGO-m after KOH activation, the hybrids of rGO-m/PANI is also cross-linked (figure 2(c)), the morphology of nanorod array and cross-linking sheets is favor for the fast ion or electron transport and expected to increase the specific capacitance, which will be illustrates later.

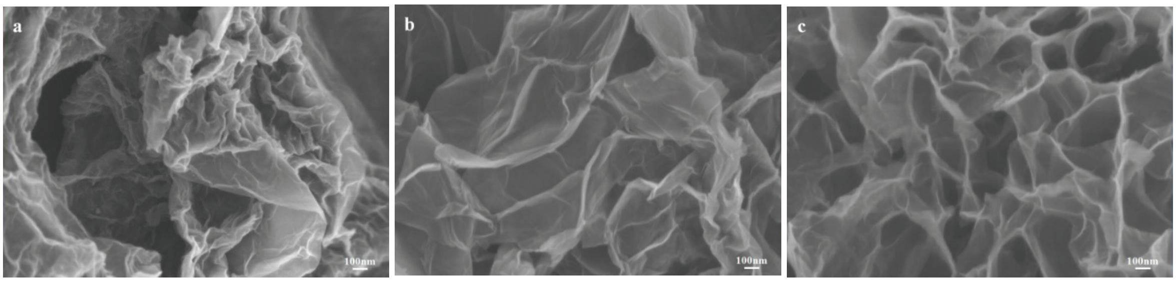

Figure 1. SEM images of (a) rGO, (b) rGO-m and (c) 3D rGO-m.

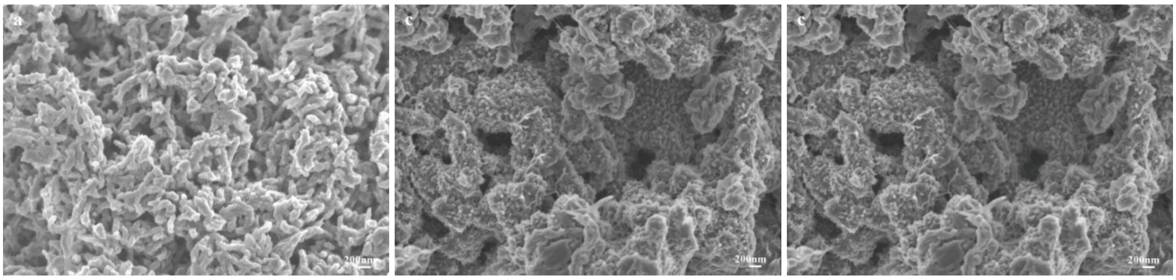

Figure 2. SEM images of (a) PANI, (b) rGO-m/PANI and (c) 3D rGO-m/PANI.

Figure 3 represents the XRD patterns of GO, rGO-m, PANI, rGO-m/PANI and 3D-rGO-m/PANI. A broad and intense peak appears at $2\theta = 11.0°$ is attributed to the (001) plane basal diffraction of GO, with an inter-layer spacing of 0.80 nm in the layer-like GO sheets. After modification, the major peak of rGO-m is shifted to 26.4° (0.34 nm), it is indicated that rGO-m has poor stacking order, and some single layer rGO were formed by completely exfoliation, and fewer layer rGO and/or even loosely stacked layers exist as well [14].

As for rGO-m/PANI and 3D rGO/PANI hybrids, four broad peaks centered at $2\theta = 9.6°$, 15.1°, 20.3° and 25.2° can be observed, which are corresponded to (001), (011), (020) and (200) planes of PANI in an emerraldine salt form, respectively [15]. XRD patterns of rGO-m /PANI and 3D rGO/PANI hybrids are similar with PANI, and the peaks of rGO at around 26.4° and around 43.1° still can be observed in rGO-m /PANI and 3D rGO/PANI hybrids. This indicates that rGO is fully contacted with PANI and PANI is successfully coated on the rGO sheets with π-stacking between themselves [16].

Figure 4 gives the FT-IR spectra of GO, rGO, rGO-m, PANI, rGO-m/PANI and 3D-rGO-m/PANI. The spectrum of GO shows the absorption peak of carbonyl C═O ($\nu_{C=O}$ at 1722 cm^{-1}), benzenoid C═C ($\nu_{C=C}$ at 1574 cm^{-1}), epoxy C—O—C (ν_{C-O-C} at 1044 cm^{-1}), hydroxyl C—OH(ν_{C-OH} at 1224 cm^{-1}) and O—H (ν_{O-H} at 3427 cm^{-1}) [17-19]. After reduction, the O—H peak at 3427 cm^{-1} still can be observed, while the carboxyl peak at 1722 cm^{-1} is unobvious. 1631 cm^{-1} is corresponding to the bending vibration of C═C. 1631 cm^{-1} peak in rGO-m is obviously stronger than that in rGO, and C—O—C peak around 1044 cm^{-1} is adverse, and a new peak at 1405 cm^{-1} appeared in the spectrum of rGO-m, which is due to the C═C stretching vibration in benzenoid rings, which further indicating that rGO-m is reduced more completely under alkaline condition. The rGO-m shows the N—H wagging vibration at 830 cm^{-1} of secondary amine group [20], and two new peaks 1270 and 1127 cm^{-1} in the spectrum of rGO-m are correponed to the stretching vibration of C—N and C═N, respectively [21], demonstrating the amino functionalization result of rGO-m [48,49]. Compared with rGO-m, the new peak 1572 cm^{-1} in the spectra of rGO-m/PANI and 3D-rGO-m/PANI is attributed to the C═C stretching vibration in the quinoid, and the stretching of C═N at 1127 cm^{-1} is obviously intense and broad, which is due to the stretching vibration of C—N·$^{+}$ in the polarized PANI structure, indicating the oxidation state existence in PANI [22]. 3D-rGO-m/PANI shows less absorption peaks of oxygen-containing functional group than rGO-m/PANI since the KOH activation at high temperature removed some of oxygen-containing functional group in rGO-m. All the above peaks observed in the spectrum of 3D rGO-m/PANI suggest that the PANI net-works are successfully decorated on graphene sheets.

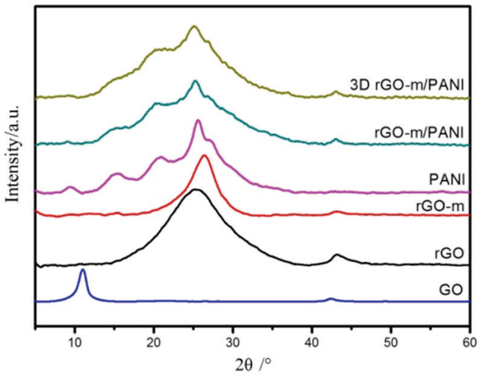

Figure 3. XRD patterns of GO, rGO, rGO-m, PANI, rGO-m/PANI and 3D rGO-m /PANI.

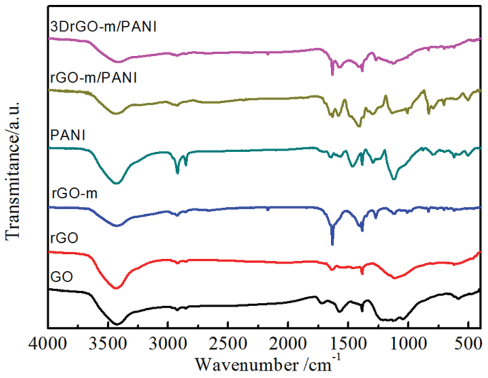

Figure 4. FT-IR spectra of GO, rGO, rGO-m, PANI, rGO-m/PANI and 3D rGO-m/PANI.

3.2 Electrochemical performance

Figure 5(a) shows the CV curves of the 3D rGO-m/PANI hybrid at a scan rate of 5, 10, 25, 50 and 100 mV/s in a 1 M H_2SO_4 solution, respectively. 3D-rGO-m/PANI hybrid presents redox peaks, which are corresponding to the structural conversions of emeraldine/pernigraniline and leucoemeraldine/ emeraldine. These results indicate good pseudo- capacitance characteristics. The mirror-like and symmetrical image in 0.5 A/g galvanostatic charge -discharge (GCD) curves indicates that the reversible redox reaction proceed in 3D rGO-m/PANI, rGO-m/PANI and PANI (figure 5(b)). The specific capacitance of 3D rGO-m/PANI calculated from GCD curves is 985 F/g at 0.5 A/g, which is higher than that of rGO-m/PANI (633 F/g) and PANI (405 F/g).

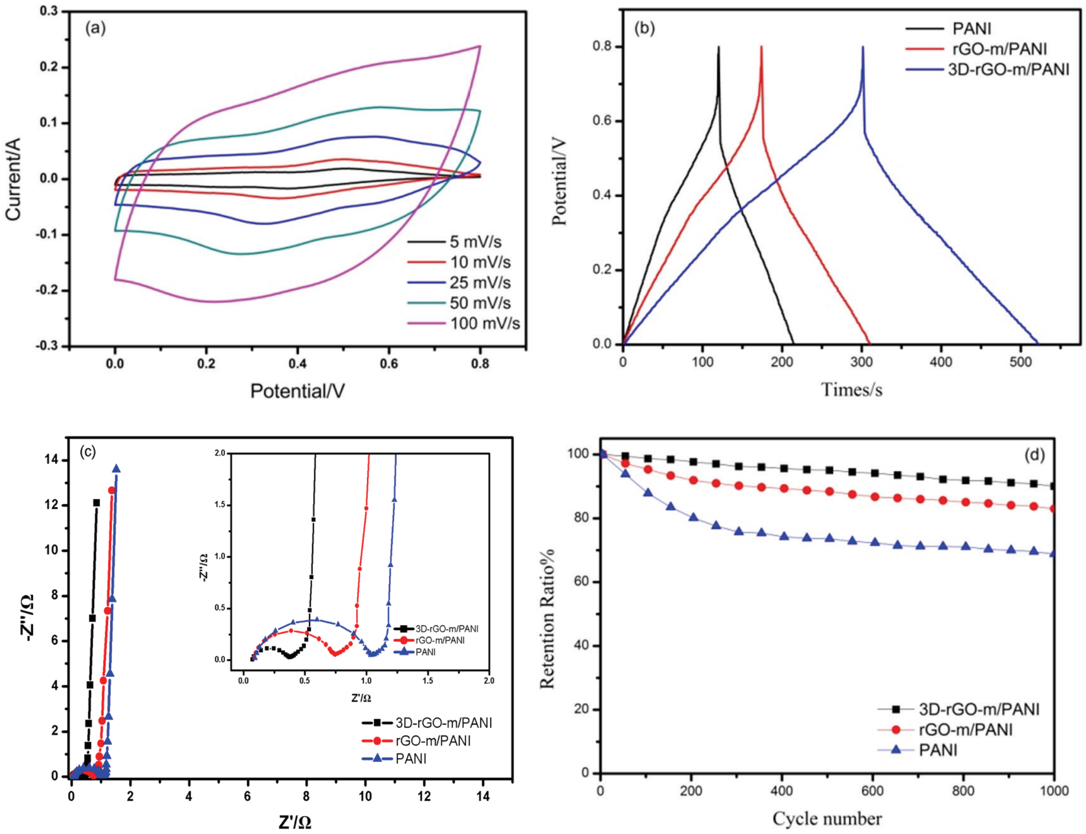

Figure 5. (a) CV curves of 3D rGO-m/PANI, (b) GCD curves at 0.5 A/g, (c) Nyquist plots and (d) cycling stability of 3D rGO-m/PANI, rGO-m/PANI and PANI.

Figure 5(c) depicts the Nyquist plots of 3D rGO-m / PANI and rGO-m/PANI hybrids. The obvious semicircle at the high frequency region can be seen. The straight line at the low frequency region is almost parallel to the vertical axis, which reflects the good capacity owing to the fast and reversible redox of PANI nanorod array. The first intersect of the Nyquist curve to the Z′ axis represents equivalent series resistance (R_s), and the diameter of the semicircle represents charge transfer resistance (R_{ct}) at the electrode/electrolyte interface. It can be seen that the 3D-rGO-m/PANI has lowest R_{ct} (0.3 Ω) and R_s (0.07 Ω) than that of rGO-m/PANI (R_{ct}=0.7 Ω, R_s =0.08 Ω) and PANI (R_{ct}=1.0 Ω, R_s =0.09 Ω). The low R_s and R_{ct} mean good electrical conductivity and fast charge transfer at the electrode and electrolyte interface, which can explain the high specific capacitance of 3D-rGO-m/PANI at a high current density. 3D rGO-m/PANI presents the energy density of 40.53 Wh/kg at the power density of 0.66 kW/kg.

Figure 5(d) is the cycling stability of the cell based on the 3D-rGO-m/PANI and rGO-m/PANI hybrids at 1 A/g for 1000 cycles. The capacitance of 3D rGO-m/PANI after 1000 cycles still reaches 90% of its original one, while rGO-m/PANI only maitains 83% of its original one, the cycling stability of both hybrids are higher than that of pure PANI (69%), so it is concluded that the cycling stability of 3D-rGO-m/PANI has been inhanced after KOH activation to rGO. The improved cycling stability could be attributed to two aspects: (1) the three-dimensional cross-linking structure of 3D-rGO-m/PANI is favorable for the ion transport through a 3D continuous channel; (2) the electrode's volume and structure changes during the charge-discharge cycling are controlled to lower degree by 3D porous structure.

4. Conclusions

In summary, 3D cross-linking porous graphene was prepared by KOH activation to the 1,2,4-triaminobenzene modified graphene precursor (rGO-m). After in-situ chemical oxidative polymerization, 3D porous rGO-m/PANI hybrids were obtained. The resulted 3D porous rGO-m/PANI hybrids possess PANI nanorod array on the 3D porous rGO-m. The 3D cross-linking porous structure provides high specific surface area, short and fast electrolyte diffusion pathways. The ion-diffusion and charge-transfer resistances of the 3D porous rGO-m/PANI hybrids are decreased. The specific capacitance is enhanced markedly compared to inactivated rGO-m/PANI hybrids and pure PANI. The maximum specific capacitance is 985 F/g at 0.5 A/g. Therefore, 3D porous rGO-m/PANI hybrids maybe become promising electrode materials for application in supercapacitors.

Acknowledgements: This work was financially supported by the Program of National Natural Science Foundation of China (No. 51472166) and Liaoning BaiQianWan Talents program.

References

[1] Zhang L L and Zhao X S. Carbon-based materials as supercapacitor electrodes[J]. Chem. Soc. Rev., 2009, 38(9):2520-2531

[2] Chen S, Xing W, Duan J J, et al. Nanostructured morphology control for efficient supercapacitor electrodes[J]. J Mater. Chem. A, 2013,1:2941-2954

[3] Stoller MD, Park S, Zhu Y, et al. Graphene-based ultracapacitors[J]. Nano Lett., 2008, 8(10):3498-3502

[4] Zhao B, Liu P, Jiang Y, et al. Supercapacitor performances of thermally reduced graphene oxide[J]. J Power Sources, 2012,198: 423-427

[5] Li L, Raji A R, Fei H, et al. Graphene oxide-based benzimidazole-crosslinked networks for high-performance supercapacitors[J]. ACS Appl. Mater. Interfaces, 2013, 5(18): 8367-8374

[6] Ćirić-Marjanović G. Recent advances in polyaniline research: polymerization mechanisms, structural aspects, properties and applications[J]. Synth Met., 2013, 177: 1-47

[7] Liu Y, Ma Y, Guang S Y, et al. Facil fabrication of three-dimentional highly ordered structural polyaniline-graphene bulk hybrid materials for high performance supercapacitor electrodes[J]. J Mater. Chem. A, 2014, 2(3): 813-823

[8] Zhao X, Gnanaseelan M, Jehnichen D, et al. Green and facile synthesis of polyaniline/tannic acid/rGO composites for supercapacitor purpose[J]. Journal of Materials Science, 2019, 54(15):10809-10824.

[9] Hu R, Zhao J, Zhu G, et al. Fabrication of flexible free-standing reduced graphene oxide/polyaniline nanocomposite film for all-solid-state flexible supercapacitor[J]. Electrochimica Acta, 2018, 261:151-159.

[10] Wang X, Zhao J, Li Z, et al. Effects of preparation conditions on the supercapacitor performances of MnO2-PANI/titanium foam composite electrodes[J]. Journal of Nanoparticle Research, 2019, 21(6):119-133.

[11] Kaushal I, Sharma A K, Saharan P, et al. Superior architecture and electrochemical performance of MnO2 doped PANI/CNT graphene fastened composite[J]. Journal of Porous Materials, 2019, 26(5):1287-1296.

[12] Lu X, Li L, Song B, et al. Mechanistic investigation of the graphene functionalization using p-phenylenediamine and its application for supercapacitors[J]. Nano Energy, 2015, 17: 160-170

[13] Li L Y, Song B, Maurer L, et al. Molecular engineering of aromatic amine spacers for high-performance graphene-based supercapacitors[J]. Nano Energy, 2016, 21:276-294

[14] Kumar N A, Baek J B. Polyaniline-grafted reduced graphene oxide for efficient electrochemical supercapacitors[J]. ACS Nano, 2012, 6(2): 1715-1723

[15] Yan J, Wei T, Fan Z J, et al. Preparation of graphene nanosheet/carbon nanotube/polyaniline composite as electrode material for supercapacitors[J]. J Power Sources, 2010, 195(9): 3041-3045

[16] Yan J, Wei T, Shao B, et al. Preparation of a graphene nanosheet/polyaniline composite with high specific

capacitance[J]. Carbon, 2010, 48(2): 487-493

[17] Raghu A V, Lee Y R, Jeong H M, et al. Preparation and physical properties of waterborne polyurethane/functionalized graphene sheet nanocomposites[J]. Macromolecular Chemistry and Physics, 2008, 209(24): 2487-2493

[18] Shin H J, Kim J, Benayad A, et al. Efficient reduction of graphite oxide by sodium borohydride and its effect on electrical conductance[J]. Advanced Functional Materials, 2009, 19(12): 1987-1992

[19] Titelman G, Gelman V, Bron S, et al. Characteristics and microstructure of aqueous colloidal dispersions of graphite oxide[J]. Carbon, 2005, 43(3): 641-649

[20] Liu Y, Ma Y, Guang S Y, et al. Polyaniline-graphene composites with a three-dimentional array-based nanostructure for high performance supercapacitors[J]. Carbon, 2015, 83: 79-89

[21] Li G C, Jiang L, Peng H R. One-dimensional polyaniline nanostructures with controllable surfaces and diameters using vanadic acid as the oxidant[J]. Macromolecules, 2007, 40(22): 7890-7894

[22] Hu H, Liu S W, Hanif M, et al. Three-dimentional cross-lingked carbon network wrapped with ordered polyaniline nanowires for high-performance pseudo-supercapacitors[J]. Journal of power sources, 2014, 268: 451-458

Viser Technology Pte. Ltd.
Research and Application of Materials Science
doi: 10.33142/msra.v2i1.1975

Research Article Open Access

Research Status and Application Prospect of Aluminum Matrix Composites

Wanwu DING[1]*, Yan CHENG[1], Taili CHEN[1], Xiaoyan ZHAO[1], Xiaoxiong LIU

[1] School of Materials Science and Engineering, Lanzhou University of Technology, Lanzhou 730050, People's Republic of China

****Corresponding Author:*** *Wanwu DING, School of Materials Science and Engineering, Lanzhou University of Technology, Lanzhou 730050, People's Republic of China; dingww@lut.cn*

Abstract:
Aluminum matrix composite is one of the most attractive metal matrix composites. It is a kind of material with strong vitality emerging in response to the needs of modern scientific development. Compared with traditional materials, aluminum matrix composites have the advantages of low density, good electric conductivity and heat conductivity, good wear resistance and oxidation resistance, high specific strength and stiffness, high temperature resistance, good heat treatment performance and flexible preparation process, which make them widely used in the fields of aviation, aerospace, and automobile. In this paper, the factors affecting the properties of aluminum matrix composites, the strengthening mechanism, classification and preparation methods of aluminum matrix composites are summarized. The research status, development direction and application prospect of aluminum matrix composites are briefly introduced.

Keywords: *aluminum matrix composites; research status; application prospect*

1. Introduction

Metal matrix composites (MMCs) are composite materials with metal or alloy as matrix and fiber, whisker or particle as reinforcement phase [1,2]. With the increasingly serious threat of energy and environmental problems to human survival, people's demand for lightweight high-strength metal matrix composites with multiple structures and functions is growing [3]. Aluminum matrix composites (AMCs) have been paid more and more attention because of their advantages, such as low density, good conductivity and thermal conductivity, good wear resistance and oxidation resistance, high specific strength and stiffness, high temperature resistance, good heat treatment performance and flexible preparation process. As early as 1924, Schmit studied the preparation of Al_2O_3/Al composite by sintering. In the 1960s, aluminum matrix composites became an important branch of composites. In the 1980s, Toyota first applied ceramic fiber reinforced aluminum matrix composite to the piston of diesel engine and achieved some success. In recent years, aluminum matrix composite materials have attracted much attention, which benefits from its unique, light, hard and strong characteristics for engineers in many fields. Compared with alternative materials that may be considered in the same type of application, aluminum matrix composite materials have many advantages, such as high strength and rigidity, corrosion resistance and wear resistance and can be produced and prepared by common equipment [4]. Alvant, a British company famous for exploring liquid pressure forming (LPF) as a process for manufacturing aluminum matrix composite materials, announced in 2018 that at the invitation of the project leader of Safran landing systems, a first-class system and equipment supplier in the aerospace and defense industry, it will participate in a two-year £ 28 million project entitled "future large landing gear" [5]. At present, a large number of researchers and research institutes at home and abroad have carried out research on aluminum matrix composites [6-9]. In this paper, the factors that affect the properties of aluminum matrix composites, the strengthening mechanism of aluminum matrix composites, the classification and preparation methods of aluminum matrix composites, the application at home and abroad, as well as the application prospect and development trend at home and abroad are reviewed and the future development direction and application prospect of aluminum matrix composites are predicted.

2. Factors affecting the properties of Aluminum Matrix Composites

The properties of composite materials have a great relationship with the types of matrix alloys and reinforcements (including microstructure, distribution and volume fraction of reinforcements, etc.) [10,11].

2.1 Selection of matrix

At present, Al-Cu, Al-Mg and Al-Si are the main aluminum matrix. Different aluminum matrix has different properties, so the wettability, performance complementarity and practical application requirements of the matrix material are mainly considered in the selection[12].

In the process of preparing aluminum matrix composite, both pure aluminum and aluminum alloy can be used as the matrix, but generally, aluminum alloy is selected because there are alloy elements in aluminum alloy, which can not only strengthen the matrix alloy, but also form metal compound precipitates with the matrix metal. In addition, aluminum alloy also has advantages of corrosion resistance, good conductivity and thermal conductivity, good recycling and no low temperature brittleness [13].

The selection of matrix is generally as follows: if the strength of the matrix is required to be high, aluminum copper alloy can be used; if the matrix is required to be light, aluminum lithium alloy can be used; if the matrix is required to have a high heat-resistant temperature, aluminum iron alloy can be used.

2.2 Selection of enhancement phase

The microstructure of the base alloy is changed by the addition of reinforcement phase, so as to improve and make up the deficiency of base metal. The influence of the properties of the reinforcing phase on the composite is due to the following factors: the interface bonding state between the matrix and the reinforcing phase, the interface reaction and wettability and the need for the properties of the aluminum matrix composite. Particle reinforced aluminum matrix composites are widely studied for their low density, high strength weight ratio, superior physical properties, high rigidity, good wear resistance and other mechanical properties at relatively low cost [14]. At present, the commonly used reinforcing particles are SiC, Al_2O_3, TiC, Si_3N_4, B_4C and graphite. Table 1 describes some reinforced ceramic particles and their related properties [15].

Table 1. Enhanced Ceramic Particles and Some Properties

Grain	performance			
	Density (g /cm^3)	Coefficient of thermal expansion (10^{-6} /℃)	Strength (MPa)	Modulus of elasticity (GPa)
B_4C	2.25	6.08	2579(24℃)	448(24℃)
SiC	3.21	5.40	–	324(1090℃)
TiC	4.93	7.60	55(1090℃)	269(24℃)
ZrC	6.73	6.66	90(1090℃)	359(24℃)
Al_2O_3	3.98	7.92	221(1090)	379(1090)
SiO_2	2.66	< 1.08	–	73
MgO	3.58	11.61	41(1090℃)	317(1090℃)
BeO	3.01	7.38	24(1090℃)	190(1090℃)
ZrO_2	5.89	12.01	83(1090℃)	132(1090℃)
AlN	3.26	4.84	2069(24℃)	310(1090℃)
Si_3N_4	3.18	1.44	–	207

The properties of aluminum matrix composites are also related to the content, morphology and distribution of reinforcing phases. For example, Quan Gaofeng et al. [16] took SiC particles as reinforcement phase, 2024 aluminum alloy, 7075 aluminum alloy and pure aluminum as matrix respectively and studied the influence of reinforcement phase content on the mechanical properties of aluminum matrix composite. The results showed that with the increase of reinforcement phase content, the elastic modulus of SiCp/2024Al increased, other strength indexes increased and the reinforcement efficiency of SiCp on Al and 2024 aluminum alloy was higher, while that of 7 aluminum alloy was higher. In addition, the fracture elongation of three composites decreased with the increase of content of reinforcement phase. Wang Tao et al. [17] studied the influence of shape and distribution of the reinforcement phase on mechanical properties of the aluminum matrix composite with 6061 aluminum alloy as the matrix, SiC particles and Si_3N_4 as the reinforcement phase. The results showed that the elastic modulus of uniformly strengthened aluminum matrix was the same while the content of SiCp reinforcement phase was the same. The yield strength of the double structure is higher than that of the uniform particles, but the modulus of network Si_3N_4 is similar.

Generally speaking, while using long fiber as reinforcement, the matrix mainly plays a fixed role and the matrix with larger strength deviation can be selected; while using short fiber as reinforcement, the matrix mainly plays a bearing role and the matrix with higher strength should be selected .

2.3 Compatibility and interface between matrix and reinforcing phase

The compatibility of the interface between matrix and reinforced phase is a very important factor affecting properties, especially when the aluminum alloy is used as the matrix, the enrichment of oxide elements often occurs on the interface and sometimes chemical reactions occur to form new phases, such as Al_4C_3, Al_3Ti, etc. In addition, due to the different thermal expansion coefficient between matrix and the reinforcing phase, the mismatch stress will induce high-density dislocation, grain size change, residual stress, etc. in the matrix. Therefore, it is often necessary to adjust composition of matrix alloy according to the different reinforcing phases, so as to avoid the reaction between interface and formation of harmful substances. It is a common method to enhance the compatibility of the matrix and reinforced phase by surface treatment, adding other components to the matrix or choosing a suitable molding method.

In addition, the interface bonding between the matrix and reinforcing phase also has an important influence on the properties of aluminum matrix composites [18]. The temperature time interface reaction is the main reason that most aluminum matrix composites can not play their best performance. The interface structure and performance is the key to form stable interface combination and obtain higher strength, so the interface optimization is needed. In general, the methods of matrix alloying, surface coating of reinforcing phase and changing adhesive are used to optimize the interface.

3. Strengthening mechanism of aluminum matrix composite

At present, the strengthening mechanisms of aluminum matrix composites are mainly Orowan strengthening, fine grain strengthening, solid solution strengthening and dislocation strengthening. These strengthening mechanisms can be expressed as [1]:

$$\sigma_{\text{composite}}=\sigma_{\text{Orowan}}+\sigma_{\text{grain}}+\sigma_{\text{solution}}+\sigma_{\text{dislocation}} \qquad (1\text{-}1)$$

3.1 Orowan enhancement

The strength improvement of the composite is partly due to dispersion strengthening (Orowan mechanism). In the process of Orowan strengthening, the nanoparticles in the matrix grains restrain the dislocation movement. The finer the particles and the smaller distance between them, the more effective strengthening mechanism is. The particle spacing can be expressed by the following formula:

$$\lambda=D\left[\frac{\pi}{6V_{\mathrm{f}}}-\frac{2}{3}\right]^{\frac{1}{2}} \qquad (1\text{-}2)$$

D is the average diameter of the particle; VF is the volume fraction. According to [19]:

$$\sigma_{\text{Orowan}}=\frac{2Gb}{2\pi(1-\upsilon)^{\frac{1}{2}}}\frac{1}{\lambda}\ln\left(\frac{D}{\mathrm{b}}\right) \qquad (1\text{-}3)$$

Where G is the shear modulus of the matrix, B is the Berger's vector and Poisson's ratio. Formula (1-4) can be obtained from formula (1-2) and (1-3):

$$\sigma_{\text{Orowan}}=\frac{2Gb}{2\pi(1-\upsilon)^{\frac{1}{2}}}\frac{1}{D\left[\frac{\pi}{6V_{\mathrm{f}}}-\frac{2}{3}\right]^{\frac{1}{2}}}\ln\left(\frac{D}{\mathrm{b}}\right) \qquad (1\text{-}4)$$

According to the Orowan mechanism, the yield strength increases with the increase of the content or the decrease of the size of the reinforcing phase. Among many strengthening mechanisms, Orowan strengthening contributes the most to the composite. Generally, it is suitable for particle reinforced aluminum matrix composite with size less than 10 μm.

3.2 Fine grain strengthening

Fine grain means that there are many grain boundaries in the material, which can effectively prevent dislocation movement. According to hall Petch formula, the effect of grain size on strength is [20]:

$$\sigma_{\text{grain}}=\sigma_0+\mathrm{kd}^{-\frac{1}{2}} \qquad (1\text{-}5)$$

Where, σ_{grain} is the yield strength of the grain; σ_{grain} is the friction resistance of dislocation movement in the grain; k is the material constant; d is the average radius of the grain. The equation shows that the smaller d is, the larger σ_{grain} is. No matter in the strengthening mechanism of any kind of material, the strength and hardness increase while the grain refinement, but the plasticity and toughness do not decrease obviously, so the fine grain strengthening is the most popular strengthening method. This strengthening method plays an important role in strengthening of micron particle reinforced aluminum matrix composites.

3.3 Solution strengthening

The additional atoms can not only block the dislocation movement, but also produce lattice distortion, which results in stress field and interaction with dislocation. The increase of yield strength caused by solution strengthening depends on the concentration of solute atoms, the difference of shear modulus between solute and matrix and the difference of size between solute and solvent atoms (causing lattice distortion as an obstacle to dislocation movement). No matter what kind of solid solution, there is a symmetrical stress field. According to literature [21], the interaction between stress field and dislocation can be expressed as follows:

$$\sigma_{\text{solute}}=\mathrm{G}\varepsilon\sqrt{\frac{\mathrm{X_f}}{4}} \qquad (1\text{-}6)$$

Where, G is the shear modulus; ε represents the change rate of the diameter difference between the foreign atom and the matrix atom; X_f is the concentration of the foreign atom. It can be seen from formula (1-6) that the larger the ε or X_f is, the stronger the solution strengthening ability is. However, due to the limited number of solution atoms and the priority of solution atoms is grain boundary and dislocation, the effect of solution strengthening on aluminum matrix composites is not obvious.

3.4 Dislocation strengthening

Due to the different thermal expansion coefficients between the matrix and the reinforcing phase, during the preparation process, those with large thermal expansion coefficients (generally the matrix) will produce plastic deformation and form high-density dislocations, thus strengthening the effect [22-24]. The increment of dislocation density can be expressed by the following formula [25,26]:

$$\Delta\rho=\frac{NS\Delta\gamma\Delta G}{\mathrm{b}} \qquad (1\text{-}7)$$

Among them, $\Delta\gamma\Delta G$ is the thermal mismatch strain; N is the number of particles; S is the total surface area of a single particle; b is the Bernoulli vector. The increase in strength due to the proliferation of dislocations can be expressed as:

$$\Delta\sigma=\mathrm{a}G_P\mathrm{b}\sqrt{\Delta\rho} \qquad (1\text{-}8)$$

Where G_p is the elastic modulus of the reinforced particles and a is the coefficient.

It can be seen that for large particles, the greater the difference between the thermal expansion coefficient of the reinforced particles and the matrix, the better the strengthening effect; however, because the reinforced phase of small particles may not meet the size requirements of dislocation nucleation, it is impossible to judge whether there is dislocation. Zhang et al. [27] found that the theoretical value of yield strength calculated under the condition of neglecting dislocation strengthening is almost the same as the experimental result when the particles of strengthening phase are very small, but it is still widely used. It is usually used in aluminum matrix composites reinforced by whiskers and particles (about 10-100nm) with aspect ratio less than 4.

4. Classification and preparation of Aluminum Matrix Composites

4.1 Classification of Aluminum Matrix Composites

There are many classification methods of aluminum matrix composites, the most commonly used classification method is divided into continuous fiber reinforced aluminum matrix composites and discontinuous particle reinforced (short fiber or whisker, particle) aluminum matrix composites. according to the different reinforcement phases.

4.1.1 Continuous fiber reinforced aluminum matrix composite

At present, the main continuous fiber reinforcements are boron fiber, carbon fiber, silicon carbide and alumina. Boron fiber is the first reinforced fiber, but the diameter of boron fiber is large, the composite material made of boron fiber has poor performance and the manufacturing cost is quite high. The room temperature properties of aluminum alloy and boron fiber composite with different components are shown in Table 1 [1].Carbon fiber has light weight, high strength, good lubrication and wear resistance and its price is about one tenth of that of boron fiber [28,29]. In the graphite fiber reinforced aluminum matrix composite, the transmission electron microscope is shown in figure 1 [30].

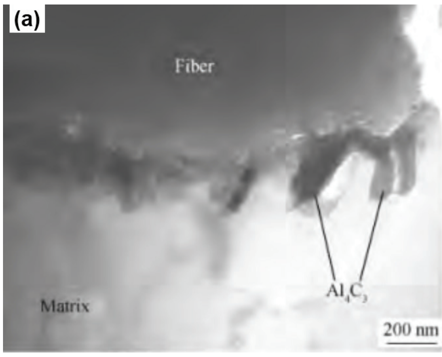

(a) Morphology of interface product

(b) Electron diffraction pattern

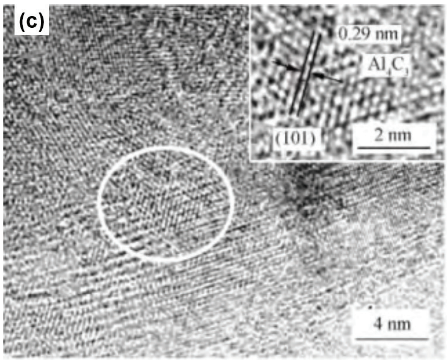

(c) Photograph with high magnification for Al_4C_3

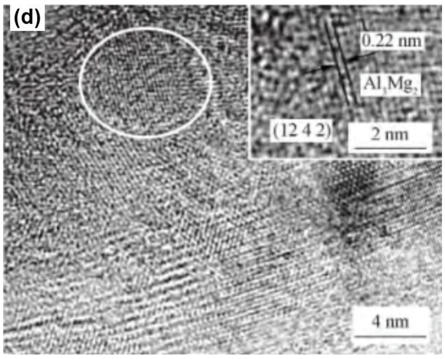

(d) Photograph with high magnification for Al_3Mg_2

Figure 1. TEM analysis of M40 / ZL301 composites

Because of its high tensile strength and modulus of elasticity, good high temperature strength and heat resistance, excellent wettability with metal and small fiber diameter, SiC fiber can be used as reinforcement fiber of heat-resistant materials and various matrix materials [31].

Al_2O_3 generally has two forms of α-Al_2O_3 and γ-Al_2O_3. Compared with carbon fiber, the strength of alumina fiber is slightly lower, but its high-temperature mechanical properties and corrosion resistance, electrical insulation and high-temperature stability are excellent [32]. The application and development of fiber-reinforced aluminum matrix composites are restricted due to the complex preparation process, high cost and unstable performance level of materials.

Table 2. Longitudinal Tensile Properties of Aluminum/Boron Fiber Composites at Room Temperature

Matrix	Volume fraction of boron fibers/%	Tensile strength /MPa	Modulus of elasticity /MPa	Longitudinal fracture strain/%
2024	47	1421	222	0.795
	64	1528	276	0.72
2024(T6)	46	1459	229	0.81
	64	1924	276	0.755
6061	48	1490	217	–
	50	1343	–	–
6061(T6)	51	1417	232	0.735

4.1.2 Discontinuous particle reinforced aluminum matrix composite

Discontinuous particle reinforced aluminum matrix composite has the advantages of simple preparation process, low cost and isotropy. Particle reinforced aluminum matrix composites are widely used because of their high modulus of elasticity, good wear resistance, good thermal conductivity and low coefficient of thermal expansion. At present, the commonly used particle reinforcements are silicon carbide, titanium carbide, titanium diboride and alumina. In recent years, graphene has also been used as reinforcement particles in aluminum matrix composites.

SiC is the most widely used reinforcement because of its high strength and high modulus. SiC particle reinforced aluminum matrix composite has the advantages of high strength, high modulus, high damping, high temperature resistance, wear resistance, fatigue resistance, good dimensional stability, small thermal expansion coefficient [33,34], which is often used to manufacture components of missiles and spacecraft, engine parts, aircraft tail balancer, etc. The microstructure of short carbon fiber and SiC particle reinforced aluminum matrix composite is shown in figure 2 [35].

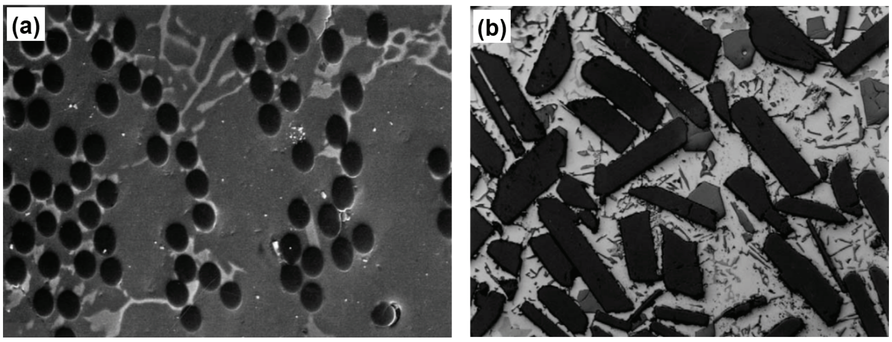

(a) short carbon fibers (×1000)

(b) SiC particulates (×400)

Figure 2. Microstructures of pressure-cast Al MMCs reinforced with [35]

TiC particles have the characteristics of high hardness, high modulus and high bending strength. It is an ideal reinforcement material for aluminum alloy, but its disadvantage is that the compatibility of TiC and Al matrix is poor. Therefore, various wettability methods are usually used to obtain good particle distribution. Lekatou et al. [36] added submicron WC particles, K_2TiF_6 and Al powder into the Al melt uniformly according to a certain proportion, so that the molten salt played an auxiliary role in the uniform distribution of TiC. The research shows that the sliding wear performance, corrosion resistance and fracture resistance of the aluminum matrix composite reinforced by WC, TiC and aluminide particles are significantly improved.

TiB_2 has the characteristics of high melting point, good wear resistance and oxidation resistance [37]. TiB_2 as reinforcement has been widely used in AMCs, ceramic materials, cemented carbide and other mechanical and electronic fields. Bij et al. [38] prepared TiB_2 reinforced 7075 aluminum matrix composite by laser cladding. The results show that the hardness of alloy increases first and then decreases with the increase of TiB_2 content. The SEM of different times is shown in figure 3; Zhang et al. [39] prepared TiB_2/6063Al composite by high energy ball milling and in-situ synthesis. Compared with the traditional method, the temperature of TiB_2 /6063Al composite is lower and the reaction time is shorter. Its strength in as cast state is about 23% higher than that of 6063Al.

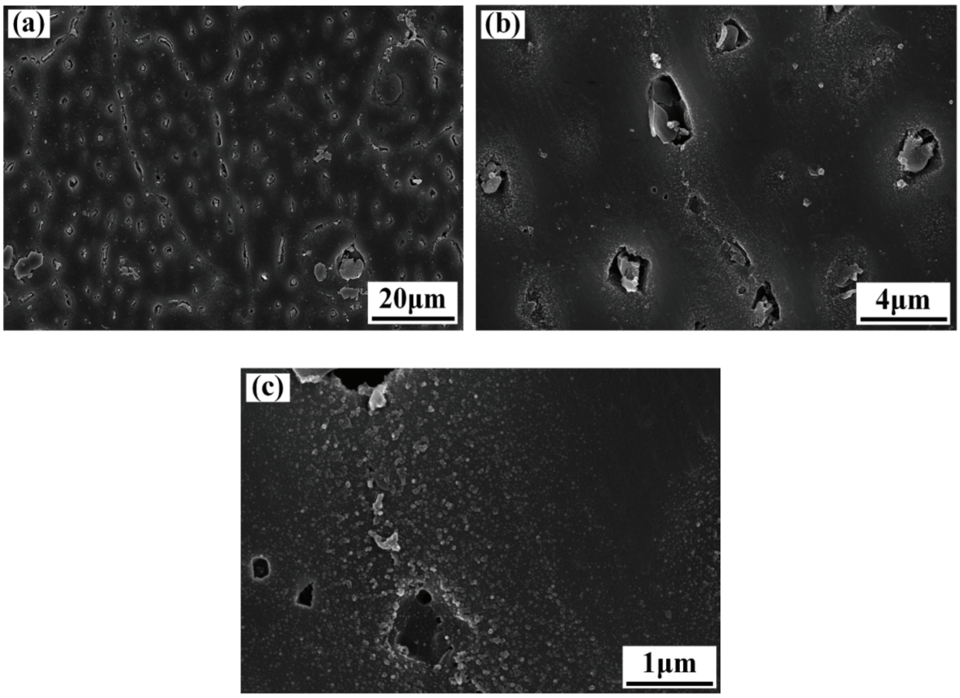

Figure 3. Different magnifications of SEM images of the etched 2wt% TiB_2 /7075 AMCs sample: (a) ×1000, (b) ×5000, and (c) ×20000 [39]

The aluminum matrix reinforced by Al_2O_3 has the advantages of high strength weight ratio, high tensile strength and high fracture toughness. If submicron or nano particles are used for strengthening, the effect is better, the hardness increases by 92% and the tensile strength increases by 57% [40] compared with pure aluminum. Compared with the matrix aluminum alloy, the Al_2O_3 particle reinforced aluminum matrix composite does not have a very high improvement at room temperature, but it will be significantly higher than the matrix aluminum alloy at a higher temperature, so it is commonly used in the manufacture of automobile drive shafts.

Graphene is the first two-dimensional (2D) material. The hexagonal honeycomb like flat film composed of carbon atoms has only one thickness of carbon atoms. The applicability research in various applications has a growing prospect in the field of materials science and shows a very high strengthening quality. Graphene is a kind of efficient conductor with good fire resistance and flexibility, which is 200 times stronger than steel and ultra light materials. It is the thinnest and hardest nano material known to human beings. Chen et al. [41] found that in the preparation of graphene reinforced aluminum matrix composite, the dispersion is poor and interface reaction is easy to occur, so this is an urgent problem to be solved in the future research of graphene reinforced aluminum matrix composite, [43] found that the addition of graphene to aluminum alloy will increase the strength and hardness of the material, increase the thermal conductivity, and maintain the ductility of aluminum alloy, so graphene reinforced aluminum matrix composite has a good prospect.

4.2 Preparation method of aluminum matrix composite

Aluminum matrix composites can be divided into two types: ex situ and in situ. The so-called exogenous type refers to that the reinforcement phase is directly added to the matrix and then mixed with the matrix by some appropriate process methods, but it has the problems of high cost, complex process and poor compatibility between the matrix and the reinforcement phase; the endogenous type is also called autogenous type, which is to mix the component materials of the reinforcement phase and the matrix and then form thermodynamically stable through in-situ chemical reaction under certain conditions. The reinforcement phase is dispersed in the matrix. The advantages of this method are small size of the reinforcement phase, good compatibility with the matrix and high interface bonding strength. Therefore, the endogenetic preparation method is commonly used in the preparation of aluminum matrix composite [1].

4.2.1 Preparation of aluminum matrix composite by exogenesis

The common processes of exogenic mold preparation include powder metallurgy, squeeze casting, liquid stirring, spray deposition and so on. These processes are described as follows:

① Powder metallurgy. Gatti A first used this method to prepare reinforced iron-based composite in 1959. It was not until the 1970s that Gatti A began to receive widespread attention. It is the most common process in preparation of aluminum matrix composite. This method has the advantages of small particle size, uniform distribution and good interface combination, but the process is complex and the cost is high. Slipenyuk et al. [44] prepared SiCp/Al composite by powder hot extrusion process, the results showed that the tensile strength and yield strength of the composite increased with the increase of SiC content and the elongation decreased. Youjiang et al. [45] selected the same powder hot extrusion process to prepare SiCp/Al composite, the results showed that SiC particles were evenly distributed in the matrix aluminum alloy, only a very small area appeared agglomeration.

② Squeeze casting. It is a kind of casting technology that extrudes the alloy into the mold smoothly at a lower speed and a larger flow rate and pressurizes the alloy instantaneously, so that the alloy can accurately duplicate the mold and solidify under high pressure, which is also called liquid forging. This method combines the advantages of press forging and die forging, reduces the defects in the casting process, has high production efficiency, but requires high superheat, promotes the interface reaction and affects the properties of composite materials. Ding et al. [46] prepared SiC particle reinforced aluminum matrix composite by squeeze casting method. The results show that proper extrusion can reduce the content of harmful gases in the composite and obtain high-quality composite with almost no shrinkage porosity and porosity.

③ Liquid agitation. After the metal is melted, the reinforcing phase is added and the blade made of appropriate material is selected for stirring. This method can speed up diffusion of reinforcement phase, promote reaction and the process is simple and efficient, but the high temperature and long time make the chemical reaction easy to occur and then reduce the properties of composite materials. Ma Ying et al. [47] prepared CuO/Al composite by liquid agitation method and the properties of the composite were improved by the formation of Al_2O_3. The results showed that with the increase of CuO content, the strength and hardness first increased and then decreased. When the content was 10%, the properties reached the optimal value.

④ Spray deposition. It was first put forward and reported by Professor singer in 1970. It is a technology between powder metallurgy and traditional casting process. The principle is to melt the metal, atomize the metal with inert gas and then rapidly solidify the atomized metal to deposit on the substrate. It can be used to prepare copper base, nickel base and magnesium base composite, but the most commonly used one is the preparation of aluminum base composite. This method has the advantages of simple preparation process, low cost, excellent properties, high porosity, long contact time between reinforcement and matrix and easy to produce harmful substances through interface reaction. Yang et al. [48] prepared TiC/Al composite by spray deposition method. The results show that compared with the matrix alloy, the silicon particles in the composite with 5% TiC are obviously refined (2 mm), which shows that adding TiC can reduce the coarsening rate of silicon particles and improve the properties of the composite.

4.2.2 Preparation of aluminum matrix composite by endogenetic method

The common endogenetic processes are self propagating high temperature synthesis, radiation dispersion, contact reaction, gas-liquid reaction and mixed salt reaction.

① Self propagating synthesis (SHS). It was first proposed by Merzhanov, a famous scientist of the former Soviet Union, in 1967, which was mainly used for the synthesis of high-temperature refractory materials. It was not used for the preparation of metal matrix composites until the end of 1980s. This method has the advantages of simple equipment, short cycle, high efficiency, low energy and material consumption, good product quality, but it is difficult to control because of its high porosity, low density and too fast reaction process. LI et al. [49] prepared TiC particle reinforced aluminum matrix composite by SHS method. It was found that Al content had the most significant effect on the size of SHS tic in Al-Ti-C system.

② RADIODIFFUSION method (XD^{TM}). It was first proposed by Martin of the United States in 1983 and improved on the basis of self propagating synthesis. This method has the advantages of high density and low cost, but the working procedure is multi period and long, the raw material must be powder and can not be directly poured. ZHU et al. [50] synthesized aluminum matrix composite by XD method and found that the elongation increased and the tensile strength decreased.

③ Contact reaction (CR). It is developed on the basis of the first two processes. The principle is that the component elements of the reinforcement phase, or compounds containing the component elements of the reinforcement phase, which are fully mixed and pressed into the matrix alloy liquid for direct contact and chemical reaction to generate the reinforcement phase and then mechanically stirred to make it disperse. This method has the advantages of low cost, full contact and reaction between matrix and reinforcing phase, and is the most popular technology at present.

④ Gas liquid reaction synthesis (VLS). It is a patented technology invented by Koczak. The advantages of this method are low cost, short reaction time and small grain size, but the types of strengthening phases are limited and the required temperature is very high[1].

⑤ Mixed salt reaction (LSM). It is a patented technology of London & Scandinavian Metallic (LSM) Company in UK. This method has the advantages of simple process, short cycle, wide source of salt and low cost, but TiB_2 will be coated by salt film, which will reduce the reinforcement effect, low volume fraction of particles and corrosive to experimental tools[1].

5. Application of aluminum matrix composite

5.1 Application of foreign aluminum matrix composite materials

In the late 1990s, electronic grade SiCp/Al composites with high volume fraction were widely used in advanced aerospace vehicles, which attracted worldwide attention

[51]. Alvant, a British company that led the development of aluminum matrix composite materials, was initially established as CMT in 2003. The goal is to explore the potential of liquid pressure forming (LPF) as a process for manufacturing aluminum matrix composite materials, so advanced liquid pressure forming (ALPF) [52] has been produced.

The SiCp/Al composite prepared by DWA company in the United States by Pressureless Infiltration meets the performance requirements for microelectronic packaging substrate. The SiCp/Al Composite replaces the original printed circuit board core and reduces the weight by 70%. In addition, the company also uses SiCp/6092Al alloy composite material for the fuselage and tail of jet fighter. The high-speed flying aircraft is more stable and the wing life will also be improved [53]. Boing replaced graphite / polymer composites with aluminum matrix composites for engine guide vanes, thus improving the impact damage of foreign objects (such as birds) [54].

British Aerospace metal matrix composite company (AMC) prepared SiC and Si mixed particle reinforced aluminum matrix composite by mechanical alloying method, which was applied to the civil helicopter produced by Eurocopter company in France due to its high modulus and fatigue resistance [55, 56]. Cercast used SiC/A357Al instead of titanium alloy to make aircraft steering frame, which not only reduced the cost, but also reduced the overall weight of the aircraft [57].

It can be seen that the United States, Britain and other developed countries have started to produce aluminum matrix composite materials in different scales as commodity supply and have been widely used in aerospace, automobile industry, sports equipment and other aspects [58].

5.2 Application of aluminum matrix composite in China

Chinese research on aluminum matrix composite materials is close to the international advanced level. It can not only be applied in the field of aerospace, but also some products have been mass produced. For example, in 2018, Chalco Shandong Branch successfully developed particle reinforced SiCp aluminum matrix composite, whose density is only one-third of that of steel, but its specific strength is higher than that of pure aluminum and medium carbon steel. It is the first large-scale production of aluminum matrix composite in China, breaking the long-term dependence on imports in China. Then, the fatigue performance of SiCp/Al aviation parts developed by Beijing General Research Institute of non ferrous metals. It has reached the international advanced level and has been applied to the aircraft; SiCp/Al composite material is used by Changchun Institute of optics, precision machinery and physics of Chinese Academy of Sciences to prepare the main bearing frame of the aircraft, which depends on the excellent thermal control function and bearing function of the material and it is also prepared to be applied to key components [59]. With increasing temperature in service (missile body parts, high-speed flying aircraft fuselage), the requirements for materials are also increasing and aluminum matrix composite materials can withstand temperatures above 300 ℃, which makes the research and use of this material more reasonable.

The launch of chang'e-3 probe on December 12th, 2013 further proves the rapid development of science and technology in China. The mobile subsystem of Yutu lunar rover and the optical system of chang'e-3, which were separated on the 15th, are a variety of high-performance aluminum matrix composite materials and components developed by the state key experiment of metal matrix composite materials of Shanghai Jiaotong University, which not only makes great contribution to the development and progress of national science and technology, but also establishes the international status of Chinese aluminum matrix composite materials.

In addition, with the development trend of today's era, UAV platform has become an emerging unmanned war weapon, which can not only conduct close detection, but also carry out the impact. At this time, high-performance aluminum matrix composite materials more meet the requirements of researchers for key components of UAV, with a good market prospect [60].

6. Application prospect and development trend of aluminum matrix composite

After decades of hard research and development, continuous fiber-reinforced aluminum matrix composite materials have made great progress in basic theory, preparation process and performance test [61]. Many materials have been used in aerospace, automobile industry, weapons and other military industries, which are increasingly used in civil applications [62]. However, compared with traditional materials, the preparation process of fiber-reinforced aluminum matrix composite is complex, the fiber price is high [63] and there are many uncertainties in its performance, such as porosity [64].

Particle reinforced aluminum matrix composites have been favored by most researchers. Not only the preparation methods and mechanical properties, including the strength, modulus of elasticity, ductility and fracture [65], but also strengthening mechanism, fracture mechanism and solid-state phase transformation, phase equilibrium relationship, phase transformation direction and driving force of particle reinforced aluminum matrix composites are studied from physical and thermal dynamics directions. At present, from material performance, plastic deformation of components, precision machining of parts to application test, particle reinforced aluminum matrix composite has made a major breakthrough [66]. However, there are still some problems such as high cost, low preparation efficiency, uncertainty of reliability and stability.

Aluminum matrix composite materials are essential for the development of high-tech technology and the realization of four modernizations in China. We should pay close attention to the development trend of foreign countries and strive to develop aluminum matrix composite materials in China. The future development should mainly focus on the following aspects:

(1) In order to improve the properties of the composite,

the interface of the composite was studied deeply;

(2) Optimize the preparation process of aluminum matrix composite. Reduce the damage and consumption in the process of processing and preparation, reduce the manufacturing cost and promote the production and application of engineering;

(3) Develop new preparation technology. Looking for a new method with low cost, high efficiency and controllable reliability;

(4) Innovate in composition to make it more customized and multifunctional;

(5) Further study on composite materials with large size and complex shape, uniformity of distribution and by-products of reaction are also urgent problems to be solved. It can be combined with laser melting, mechanical stirring, high-pressure torsion and other processes to promote the dispersion distribution and grain refinement of the reinforcement phase and improve the mechanical properties.

After nearly 30 years of efforts and exploration, the fiber-reinforced aluminum matrix composite has made great progress in basic theory, preparation process, performance level, etc. It is the first to be applied in aerospace, aviation and weapons and the application in civil industry is also increasing. However, its application is not as wide and deep as people expect and it is impossible to completely replace the traditional metal materials in a short period of time. There are still many problems to be solved, such as the complex preparation process of this material, high fiber price and unstable performance level of the material, which restrict its application and development [67]. In order to further improve the properties of the material, reduce its manufacturing cost and accelerate its industrialization process, the following basic issues need to be further studied: (1) around the economical, effective and easy to operate surface coating technology of fiber reinforced body; (2) the influence of the alloying of aluminum and aluminum alloy on the interface stability and structure; (3) fiber reinforced body and aluminum alloy influence of the interface bonding strength of the gold matrix on the properties of the material; (4) the practical research and application of preparation process of the fiber-reinforced aluminum matrix composite.

7. Concluding remarks

Aluminum matrix composite is an ideal structural material for aerospace vehicles, which has been widely used in the field of aerospace. In the high-tech war with aircraft and missile as the main means of combat, aluminum and aluminum alloy occupy a very important position, which has been listed as one of the key light structural materials for the key development by the country. At the same time, it is considered as a new generation of materials that can improve the performance of aluminum and increase the use range of aluminum materials, which will become the candidate materials for ultra high speed aerospace vehicles and the next generation of aeroengines. However, there are still some problems in the preparation of aluminum matrix composites, such as uneven distribution of reinforcement phase, poor surface wettability, interface reaction between particles and matrix and so on. Therefore, future research should focus on these problems and on the basis of solving these problems, further optimize all aspects of the performance of aluminum matrix composite to make it more customized and multifunctional [68].

Author Contributions: Wanwu DING is responsible for the overall idea, design and revision of the paper. Yan CHENG write and modify. Data collected and written by Taili CHEN, Xiaoyan ZHAO and Xiaoxiong LIU.

Conflicts of interest: There are no conflicts to declare.

Acknowledgments: Thanks for the support of the National Natural Science Foundation of China (51661021). Thanks for the support of Key Research and Development Projects of Gansu Province (18YF1GA061) and China Postdoctoral Science Foundation (2019M653896XB).

References

[1] ZHAO Y T. In-situ synthesized aluminum matrix composites [M]. Beijing: Science Press, 2016.

[2] HUO X Y, ZHAO Y T, CHEN G, et al. Dry sliding wear properties and mechanism of high silicon aluminum alloy and its in-situ composites. Casting, 2007, 56 (4): 375-379.

[3] ZHANG S, DONG X, ZHAO Y, et al. Preparation and wear properties of TiB_2/Al-30Si composites via in-situ melt reactions under high-energy ultrasonic field. Transactions of Nonferrous Metals Society of China, 2014, 24(12):3894-3900.

[4] LE Y K, ZHANG Y Y. Research status of particulate reinforced aluminum matrix composites [J]. Development and application of materials, 1997 (05): 33-39.

[5] NICK B, Aluminum matrix composites [J], Reinforced Plastics, 2019.

[6] BRENDEL A, POPESCU C, SCHURMANN H, et al. Interface modification of SiC-fiber/copper matrix composites by applying a titanium interlayer [J]. Surface and Coatings Technology, 2005, 200(1-4):161-164.

[7] YOU J H, BOLT H. Prediction of plastic deformation of fiber-reinforced copper matrix composites [J]. Journal of Nuclear Materials, 2002, 307(1):74-78.

[8] EZHIL V S, VIZHIAN S P. Dry sliding wear behavior of basalt short fiber reinforced aluminum metal matrix composites [J]. Applied Mechanics & Materials, 2014, 592-594:1285-1290.

[9] SU H, GAO W, FENG Z, et al. Processing, microstructure and tensile properties of nano-sized Al_2O_3 particle reinforced aluminum matrix composites [J]. Materials & Design, 2012, 36(none):590-596.

[10] CHOU T W, NOMURA S, TAYA M, A self-consistent approach to the elastic stiffness of short-fiber

composites. J Comp Mater,1980,14:178-188

[11] MICHAL B, JOZEF I LADISLAV K. Influence of Al_2O_3 particles volume fraction on fracture mechanism in the Cu-Al_2O_3 system [J]. Materials Letters, 2000, 46(2).

[12] XIAO R L, ZHENG H A, FU D S, et al.Preparation and Application Progress of Aluminum Matrix Composites[J]. Foundry technology, 2015 (5): 1118-1121.

[13] ZHAO L Z, YANG M. Study on particle reinforced aluminum matrix composites [J]. Hot Processing Technology, 2011, 40 (20): 107-110.

[14] KANG Y C, CHAN L I. Tensile properties of nano-metric Al_2O_3 particulate-reinforced aluminum matrix composites [J]. Materials Chemistry and Physics, 2004, 85(2-3):438-443.[15] IBRAHIM I A et al. Journal of Materials Science, 1991; 26: 1137-1156.

[16] QUAN G F, CHAI D L, SONG Y J, et al. Effect of reinforcement phase type and content on mechanical properties of metal matrix composites [J]. Journal of Composites, 1999,16(2): 62-66.

[17] WANG T, ZHANG F, ZHOU X L, et al. Effect of reinforcement phase morphology and distribution on mechanical properties of aluminum matrix composites [J]. Hot Working Process, 2009, 38 (16).

[18] ROSCOE A N. The viscosity of suspensions of rigid spheres. British Journal of Applied Physics, 1952, 3:267-269.

[19] ZHANG Q, XIAO B L, WANG W G, et al. Reactive mechanism and mechanical properties of in-situ composites fabricated from an Al- TiO_2 system by friction stir processing. Acta Materialia, 2012, 60(20): 7090-7103.

[20] HSU C J, CHANG C Y, KAO P W, et al. Al-Al_3Ti nanocomposites produced in-situ by friction stir-processing. Acta Materialia, 2006, 54: 5241-5249.

[21] VERHOEVEN J D. Fundamentals of physical metallurgy. New York: John Wiley & Sons, Inc., 1975.

[22] EVANS A G, HUTCHINSON J W, MCMEEKING R M. Stress-strain behavior of metal matrix composites with discontinuous reinforcements [J]. Scripta Metallurgica Et Materialia, 1991, 25(1):3-8.

[23] ARSENAULT R J, SHI N. Dislocation due to differences between the coefficients of thermal expansion [J]. Materials Science and Engineering, 1986, 81:175-187.

[24] ARSENAULT R J, WANG L, FENG C R. Strengthening of composites due to microstructural changes in the matrix[J]. Acta Metall Mater, 1991, 39(1):47-57.

[25] XUE J, WANG J, HAN Y F, et al. Behavior of CeO_2 additive in in-situ TiB_2 particles reinforced 2014 Al alloy composites [J]. Transactions of Nonferrous Metals Society of China, 2012, 22:1012-1017.

[26] RAM N R, PRASADA R A K, DUTTA G L. et al. Forming behavior of Al-TiC in-situ composites [J]. Materials Science Forum, 2013, 765:418-422.

[27] ZHANG Q, XIAO B L, WANG W G, et al. Reactive mechanism and mechanical properties of in-situ composites fabricated from an Al–TiO_2 system by friction stir processing [J]. Acta Materialia, 2012, 60(20):7090-7103.

[28] HAO X, NIE H, YE Z, et al. Mechanical properties of a novel fiber metal laminate based on a carbon fiber reinforced Zn-Al alloy composite[J]. Materials Science & Engineering A, 2018.

[29] FENG G, LI Z, JACOB R J. et al. Laser-induced exothermic bonding of carbon fiber/Al composites and TiAl alloys [J]. Materials & Design, 2017, 126:197-206.

[30] NIE M M, XU ZH F, YU H, et al. Effect of matrix alloy on fiber damage and fracture mechanism of continuous M40 graphite fiber / Al composite [J]. Journal of composite materials, 2016 (12).

[31] PAWAR P B, WABALE R M, UTPAT A A. et al. A comprehensive study of aluminum based metal matrix composites: Challenges and Opportunities. Science Direct. 2018: 23937–23944.

[32] YANG O, JIAN J W, XIN R D. et al. Experimental investigation on characteristics of pulsed plasma thrusters with the propellant samples of modified PTFE filled Si, Al and Al_2O_3 [J]. Vacuum, 2019: 163-171,

[33] HASSAN S, HOSSEIN R B, MOHAMAD R N. The influence of volume fraction of SiC particles on the properties of Al/SiCp nanocomposites produced by powder metallurgy with high energy ball milling [J]. Russian Journal of Non-Ferrous Metals, 2016, 57(7).

[34] SIVAIAH B, SARAVANAN M, AJAY D. Nano-indentation and Wear Characteristics of Al 5083/SiCp Nanocomposites Synthesized by High Energy Ball Milling and Spark Plasma Sintering[J]. Journal of Materials Science & Technology,2012,28(11):969-975.

[35] HUANG G Q, WU J, HOU W T, et al. Microstructure, mechanical properties and strengthening mechanism of titanium particle reinforced aluminum matrix composites produced by submerged friction stir processing [J]. Materials Science & Engineering A, 2018:353–363.

[36] LEKATOU A, KARANTZALIS A E, EVANGELOU A, et al. Aluminum reinforced by WC and TiC nanoparticles (ex-situ) and aluminide particles (in-situ): Microstructure, wear and corrosion behavior [J]. Materials & Design, 2015, 65:1121-1135.

[37] XI L X, ZHANG H, WANG P, et al. Comparative investigation of microstructure, mechanical properties and strengthening mechanisms of Al-12Si/TiB_2, fabricated by selective laser melting and hot pressing[J]. Ceramics International, 2018: S0272884218316729.

[38] BI J, LEI Z L, CHEN X, et al. Microstructure and mechanical properties of TiB_2-reinforced 7075 aluminum matrix composites fabricated by laser melting deposition [J]. Ceramics International, 2019:5680–5692.

[39] ZHANG S L, YANG J, ZHANG B R, et al. A novel fabrication technology of in-situ TiB2/6063Al composites: High energy ball milling and melt in-situ reaction [J]. J Alloys Compound, 2015, 629:215.

[40] IBRAHIM I A et al. Journal of Materials Science, 1991;

26: 1137-1156.

[41] CHEN X, FU D, TENG J, et al. Hot deformation behavior and mechanism of hybrid aluminum-matrix composites reinforced with micro-SiC and nano-TiB_2 [J]. Journal of Alloys & Compounds, 2018.

[42] ZHOU C,JI G,CHEN Z,et al. Fabrication interface characterization and modeling of oriented graphite flakes/Si/Al composites for thermal management applications[J]. Materials and Design,2014(63):719-728.

[43] YAN S J,DAI S L,ZHANG X Y,et al. Investigating aluminum alloy reinforced by graphene nano-flakes[J].Materials Science & Engineering A,2014(612):440-444.

[44] SLIPENYUK A, KUPRIN V, MILMAN Y, et al. Properties of P/M processed particle reinforced metal matrix composites specified by reinforcement concentration and matrix-to-reinforcement particle size ratio[J]. Acta Materialia, 2006, 54(1):157-166.

[45] YOU J, LIU Y Z, GU C X, et al. Microstructure and mechanical properties of SiCp/2024 aluminum matrix composites by hot extrusion of powder [J]. Science and Engineering of Powder Metallurgical Materials, 2014 (1).

[46] DING Z L, REN D L, QI H B, et al. Squeeze casting process of SiC particulate reinforced aluminum matrix composites [J]. Special casting and non-ferrous alloys, 1999 (s1): 64-65.

[47] MA Y, HAO Y, KOU S Z, et al. Preparation and mechanical properties of CuO/Al reactive in-situ composites [J]. Journal of Material Heat Treatment, 2003 (1): 37-40.

[48] YANG B, WANG F, ZHANG J S. Microstructural characterization of in situ TiC/Al and TiC/Al-20Si-5Fe-3Cu-1Mg composites prepared by spray deposition[J]. Acta Materialia, 2003, 51(17):4977-4989.

[49] LI X L, CHEN Y B, YANG B L, et al. Morphology evolution of TiC particulates formed by self-propagating high-temperature synthesis in Al-Ti-C system[J]. Journal of Hebei University of Science and Technology,2010(06):88-93.

[50] ZHU H G, WANG H ZH, XIONG D SH, et al. Microstructure and mechanical properties of aluminum matrix composite synthesized by XD method [J]. Acta metalica Sinica, 2005 (08): 47-52.

[51] SATISH T, SHARMA V K, MOHANTY R M, et al. Microstructure, adhesion and wear of plasma sprayed Al Si-SiC composite coatings [J]. Journal of Surface Engineered Materials and Advanced Technology, 2012, 2(3): 227-232.

[52] QIANG Y H, WANG X H, FENG P Z. Research progress of SiCp reinforced metal matrix composites [J]. Light metals, 2003 (7): 49-51.

[53] SREEKUMAR V M, HARI B N, ESKIN D G, et al. Structure-property analysis of in-situ Al-$MgAl_2O_4$ metal matrix composites synthesized using ultrasonic cavitation[J]. Materials Science and Engineering: A, 2015, 628:30-40.

[54] CHAWLA N, C HAWLA K K. Metal matrix composites [M]. New York: Springer Science Business Media Inc, 2006:353-355.

[55] TAHA M A, EL M N, EL S A. Some experimental data on workability of aluminum particulate-reinforced metal matrix composites [J]. Journal of Materials Processing Technology, 2008, 202(1/3): 380-384.

[56] RAMACHANDRA M, RADHAKRISHNA K. Effect of reinforcement of flyash on sliding wear, slurry erosive wear and corrosive behavior of aluminum matrix composite [J]. Science Direct, 2007, 262(11/12): 1450-1462.

[57] SEYED S M, REIHANI. Processing of squeeze cast Al6061-30vol% SiC composites and their characterization [J]. Materials and Design, 2006, 27(3): 216-222.

[58] HAN H H, WANG A Q, XIE J P. Research status of SiC and Si particle reinforced aluminum matrix composites [J]. Powder metallurgy industry, 2015, 25 (06): 66-71.

[59] CHENG Z F, ZHANG B, WANG P, et al. Application of SiC/A composite material in airborne photoelectric stabilization platform [J]. Journal of Changchun University of Technology (Natural Science Edition), 2011, 34 (1): 130-133.

[60] NIE J H, FAN J Z, WEI S H, et al. Development and application of aeronautical powder metallurgy particle reinforced aluminum matrix composites [J]. Aviation manufacturing technology, 2017 (16): 26-36.

[61] WANG T, ZHAO Y X, FU S H, et al. Development and key issues of continuous fiber reinforced metal matrix composites [J]. Journal of Aviation Materials, 2013, 33 (02): 87-96.

[62] MENG L. Research status of fiber reinforced aluminum matrix composites [J]. Science and technology information, 2009 (18): 437-438.

[63] ZHONG L, HAN X, ZHOU S Q. Research progress of fiber reinforced aluminum matrix composites [J]. Mechanical engineering materials, 2002 (12): 12-14.

[64] ZHOU T, ZHOU X Y, DA J C, et al. Research progress of carbon fiber reinforced metal matrix composites [J]. Hot processing technology, 2016, 45 (18): 31-32+37.

[65] XUE Y, SONG M, XIAO D H. Preparation and mechanical properties of particulate reinforced aluminum matrix composites [J]. Natural Journal, 2015, 37 (01): 41-48.

[66] FAN J Z, SHI L K. Research and application development of particulate reinforced aluminum matrix composites [J]. Aerospace materials technology, 2012, 42 (01): 1-7.

[67] HUANG G Q,WU J,HOU W T, et al. Microstructure, mechanical properties and strengthening mechanism of titanium particle reinforced aluminum matrix composites produced by submerged friction stir processing [J]. Materials Science & Engineering A, 2018:353–363.

[68] PAN L W, LIN W D, TANG J F, et al. Preparation methods and research status of particulate reinforced aluminum matrix composites [J]. Material report, 2016, 30 (S1): 511-515.

Viser Technology Pte. Ltd.
Research and Application of Materials Science
doi: 10.33142/msra.v2i1.1976

Research Article Open Access

Review Study on the Accumulation and Release of Trace Metal Elements on Aluminum Containing Sediments in Drinking Water Distribution System

Xiaoni ZHANG[1], Jinghua MENG[1], Li CHEN[1], Huanhuan ZUO[1], Wendong WANG[2]

1 School of Civil Engineering, City College of Science and Technology Chongqing University, Chongqing, China
2 School of Human Settlements and Civil Engineering , Xi`an Jiaotong University, Xi`an, China

**Corresponding Author:* *Wendong WANG, No.28, Xianning West Road, Xi`an, Shannxi, 710049, China; wdwang@xjtu.edu.cn*

Abstract:
Accumulation and releasing of trace metal elements on aluminum containing sediments of inner drinking water pipe is discussed, as studied from five variations effecting: raw water quality, chemical reagents, solution pH and drinking water flow condition . In order to decrease the release of trace metal elements, and to ensure the pipe operation and human safety, water quality adjustment is suggested to avoid aluminum containing sediments formation in drinking distribution system. The maximum amounts of accumulation of common trace metal elements are given. Future trends of development in this field are also proposed.

Keywords: *drinking water distribution system; aluminum containing sediments; trace metal elements; accumulation; release*

1. Introduction

There are serious corrosion and deposition on the inner wall of water supply network. Scale deposits containing aluminum (aluminum) on the pipeline corrosion and the release of pollutants plays a protective role, as well as a variety of trace metal elements important substrate adsorption accumulation, have a positive impact on water supply security [1]. However, sudden release of metal elements may occur when water quality conditions change or sediment structures are damaged. As a result of trace metal elements in pipe network in the sediment accumulation and sudden release has caused a serious impact on the health of residents drinking water [2], the attention of the safety of drinking water is one of the change of the water treatment process, make the existing network of aluminized sediments off the steady probability and harm degree.

2. Accumulation and release of trace metal ions by aluminum-containing deposits

2.1 Accumulation of metal ions by aluminum-containing deposits

Aluminum deposits can effectively store various metallic elements under the action of adsorption and coprecipitation. Taking lead ion as an example, before aluminum salt was used for coagulation treatment, the lead ion concentration in the Hemlock waterworks was 15-38μg/L. two and a half months after the use of aluminum salt, the concentration of lead ions in the effluent can be decreased to 5-15μg/L, the pH of the solution is relatively stable in the process. At the same time, with the decline of water distribution capacity of the pipe network.The composition analysis shows that there are a lot of aluminum elements in the sediments, mainly silica-aluminate.

The accumulation of trace metal elements in pipe network sediments is related to factors such as sampling location, pipeline material and corrosion degree (Table 1). The contents of arsenic, aluminum and zinc in copper pipe sediments were 2100 mg/kg, 68-200 mg/kg and 52-6510 mg/kg respectively, while the contents in lead pipe were 229 mg/kg, 36,000 mg/kg and 36900 mg/kg respectively. At the same time, the storage capacity of metal elements in the sediments formed by the same pipe in different pipe network systems is quite different.

2.2. Destabilization release of metal ions

Most metal ions can be stored in the pipe network by physical and chemical actions such as adsorption, precipitation and coprecipitation. However, as a large reservoir of various pollutants, changes in hydraulic and water quality conditions may also have adverse effects on its stability, leading to the sudden release of pollutants

[21-22].A pipe network system in Wales, England, no used lead pipe material, a large number of metal elements such as lead, copper, zinc and tin was detected in the water of the pipe network[23]. Investigation revealed inside the pipe wall there is a layer of green pipe scale, main ingredients for aluminum (68-200 mg/kg), lead (574-2940 mg/kg), chromium (32-112 mg/kg), tin (11-273 mg/kg), cadmium (5.4 mg/kg), antimony (0.4 1.7 mg/kg), zinc (52-510 mg/kg). When the coagulant was changed from aluminum salt to iron salt, the composition of the aluminum-containing sediments changed accordingly. Considering the safety of water supply and residents' drinking water, it is necessary to investigate the influence of changes in water hydraulic and quality conditions on the stability of aluminum deposits in the pipe network and the release characteristics of various trace elements.

Table 1. Summary of the characteristics of aluminum containing sediments and their adverse effects researched in published studies

Study	Date	Observation	Ref.
Baylis	1953	After the South District Filtration Plant was put in operation, a soft gelatinous coating was formed in the pipe line. It consisted mainly of aluminum hydroxide, with considerable silica.	3
Hudson	1966	Regardless of the type of pipe material, when coagulation and filtration operation was not proper, aluminum hydroxide could be formed. Very thin aluminum deposits could reduce its carrying capacity notably.	5
Cooper & Knowles	1975	Within 5 years operation, 2 mm thick whitish-grey substance formed on the pipe surface of a 42-inch main in London. The sediments were mostly amorphous interspersed with fine silica, and composed by 20-23% Al_2O_3, 25-40% SiO_2, 4-8% CaO, 6-10% MgO, 3-10% Fe_2O_3.	4
Hoff	1978	Aluminum phosphate particles and clay were believed to be representative particles in many drinking water distribution systems.	6
McGinn & Briggs	1979	Slimy deposits, containing 80-90% aluminum, with small amounts of iron, magnesium, silica and organic carbon, were found in the pipe line.	7
Qureshi & Malmberg	1985	Aluminum post precipitation occurred in the distribution mains of Fridley Filtration Plant, Minneapolis, Minnesota.	8
Fitch & McCollum	1986	A 10 mm thickness gelatinous precipitate that composed predominantly of aluminum and silicon oxide was found, which might contribute to the rapid loss in transmission capacity.	9
Zimmerman	1986	Increased energy consumption and approximately 25% loss of transmission capacity accompanied the aluminum containing sediments precipitation. When the drinking water pH increased, it would become unstable.	10
Fuge et al.	1992	Reduction in finished water Al concentration caused soluble and particulate aluminum release from a in a Wales distribution system network and domestic piping.	11
Shea	1993	A white powder scale was discovered in Green Bay, Wisconsin pipe line. Laboratory analysis indicated that it was mainly aluminum silicate. The addition of orthophosphate did not cause any improvement.	12
Lauer & Lohman	1994	The main sediment composition of Denver distribution system, storage reservoir and lead pipe wall were 36-42% Al_2O_3, 24-29% SiO_2, 1-3% CaO.	13
Kriewall et al.	1996	The transmission capacity decreased notably after a new filtration plant put into operation, which might connected with the aluminum containing colloidal or particles.	14
Kirmeyer et al.	1999	Reddish and reddish-grey deposits were found in the control loop of pipe. Analysis of the material showed 15% Al and 50% organic matter on a dry basis.	15
Havics	2001	The white precipitates formed in the drinking water distribution system of Georgia contained substantial concentrations of aluminium and phosphorus, and sometimes associated with Si, Fe and other elements.	16
Snoeyink et al.	2003	Summarized the sources and characteristics of aluminium containing sediments, and presented new data on the elemental composition of scales found in selected systems in the USA.	2
Schock et al.	2005	Pointed out that the accumulation of inorganic pollutants, including aluminum should be received much attention. Their suddenly release was as serious as that caused by organic matters.	2
USEPA	2006	Summarized aluminum containing sediments and other sediments accumulation in drinking water supplying system, their effects on drinking water quality, and factors affecting pollutants accumulation and release.	17

Table 2. Summary of trace metal elements accumulation occurrences in published studies

Contaminant	Sample Source	Contaminant concentration (mg/kg)	Potential for MCL exceedance† (mg scale or sediment per litre)	Ref.
Antimony	Lead line	100	60	18
	Flush water	0.027	-	19
	Reservoir sediment	48	125	20
	Lead line	229	44	18
	Flush water	0.151	-	19
	Reservoir sediment	300	33	20
Barium	Lead line	88	22700	18
Beryllium	Lead line	460	8.7	18
	Lead line	290	13.8	18
Cadmium	Lead line	76.8	65.1	18
Chromium	Lead line	65.4	1529	18
Copper	Lead line	350	3714	18
	Lead line	1100	182	18
	Flush water	1.37	-	19
	Reservoir sediment	830	18.1	20
Mercury	Lead line	1.24	1613	18
Selenium	Lead line	7.8	6410	18
Thallium	Lead line	12.7	157	18
Aluminum	Lead line	121000	0.41-1.65	18
	Lead line	36000	1.4-5.6	18
Nickel	Lead line	164	610	18
Silver	Lead line	1.3	76900	18
Vanadium	Lead line	182	-	18
Zinc	Lead line	36900	135.5	18
	Reservoir sediment	13000	385	20
Rare Earth Elements	Lead line	4478	-	18
	Lead line	794	-	18

2.2.1. Influence of water flow status

The rapid change of the flow conditions, such as pipe flushing, peak flow and fire flow may damage the structure stability of the sediment, cause the release of trace metal elements, and the change range of flow and sediment state of aggregation on the release of aluminum content has an important influence. When the flow rate increases from 1.7m /s to 1.9m /s, loose deposits with large sand content in the pipe network can enter the main water phase in the form of suspended state. For loose deposits with high content of metal elements, the flow velocity should be increased from 1.9m /s to 4.0m/s to achieve the same scouring effect. When the flow rate increases to over 4 m/s, the scale on the pipe wall and some pipe materials will also enter the water[24]. Experience showed that the traditional hydrant flushing technology is undesirability for removing impurities in pipelines including aluminum deposits due to the reciprocating change of flow direction, while one-way flushing removed most of the sediment. In addition, the structural characteristics of sediments have some influence on their stability. Due to oxidation, corrosion and other effects of the formation of benign tumors, pipe scale and other structures relatively stable, the flow rate and flow direction change less impact on it; aluminum deposits are more prone to structural damage.

2.2.2. Effects of raw water quality

The water quality of most surface water bodies is characterized by seasonal variation. In addition, in the season with high turbidity, groundwater is often used to replace surface water sources. The difference in water quality between water sources will also lead to changes in water quality of water supply. When the water quality of raw water fluctuates greatly, if the water purification process cannot be adjusted in a timely manner, the chemical stability of the pipe network sediments will be damaged and a large number of metal elements will be released. Before 1990, a water system in central Wales used surface water as its source. The concentration of aluminium ions in raw water is between 0.15 mg/L and 0.30 mg/L. Considering the high residual aluminum content in the treated water, a centralized cleaning of the pipe network was carried out in 1990, and the water source was switched to groundwater with low aluminum content. The residual aluminum concentration in the pipe network decreased significantly after the water source was switched over. However, with the increase of water transmission distance, the concentration gradually increased. When the water delivery distance is 3.1 miles, the aluminum ion concentration in the pipe network is 0.017 mg/L. The aluminum ion concentration was 0.05mg /L after the water delivery distance increased to 11.2 miles, indicating that there was the release of aluminum ion in the pipeline sediments, and the water source switching process damaged the stability of the original aluminum pipe scale [23].

2.2.3. Effect of solution pH

Under short-term water supply conditions, the pH of the solution fluctuate within 0.5 pH units. PH fluctuation is more pronounced during seasonal changes or when water is switched. In order to improve the treatment efficiency of coagulation precipitation and reduce the corrosion of metal pipes in the process of water distribution, some water plants still need to adjust the pH of the treated water. When pH changes by more than 1 pH unit, aluminum deposits deposited in pipes such as lead pipes, copper pipes and iron pipes will be destroyed, resulting in the release of metal ions[26]. Munk et al. believed that the minimum pH change of metal ions in aluminium-containing sediments was about 0.2 pH units. Therefore, even under the normal pH condition of water distribution, the release of zinc, copper, nickel, molybdenum, cadmium and other elements still exists [27]. Kendall partial correlation analysis showed that the adsorption of metal ions, such as copper and chromium, on the surface of sediments is mainly related to the content of aluminum in sediments, but is less affected by iron and manganese [28].

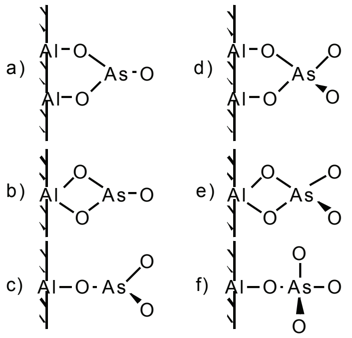

Figure 1. Molecular configurations of As(Ⅲ) and As(Ⅴ) inner-sphere surface complexes [25]

The storage and release of arsenic in sediments is related to its valence state and solution pH[2]. When the pH > 5.5, trivalent arsenic and amorphous aluminum hydroxide surface between the outer and inner layer with two kinds of combination way, and with the ionic strength of solution is reduced, the outer with more pronounced; When the pH value is less than 5.5, the inner layer coordination modes, such as dual-teeth dual-core, dual-teeth monocytes and single-tooth monocytes, are mainly adopted (figure 1). As the pH of the solution increases, the binding capacity of the two increases continuously, which is conducive to the storage and precipitation of arsenic trivalent. The combination of arsenic pentavalent and amorphous aluminum hydroxide is mainly the inner double dentate biconuclear coordination, the adsorption strength of arsenic on the solid surface decreases with the increase of pH.

2.2.4 Use of chemical agents

The use of polyphosphates and other masking agents can effectively increase the chemical stability of iron, calcium, aluminum, manganese, magnesium and other metal ions and reduce the formation of pipeline sediments. The enhanced solubility will destroy the chemical stability of existing aluminum-bearing sediments, leading to the desorption and redissolution of trace metal elements. For the water distribution system using asbestos-cement pipe, under the competition and softening effect of polyphosphate, the aluminum precipitation of pipeline material is serious. In order to prevent corrosion of metal pipes, orthophosphate is often added to the treated water. Davis et al. investigated the effect of corrosion inhibitors such as orthophosphate on metal ion release in the actual pipe network by using simulation system, the concentration of arsenic in the main flow is 0.010 mg/L, after 3 hours of stable operation, 1 mg/L of orthophosphate was added at the inlet of the pipe network, it was found that the arsenic content in the outlet water of the pipe network increased significantly after the addition of orthophosphate, 1.6 to 15 times of the background concentration and up to 1.5mg/L[29].

3. Conclusions and prospects

Deposits containing aluminum is very common in the pipe network under the effect of adsorption and coprecipitation and other physical and chemical, for the accumulation of the trace metal elements in the water has obvious effect, and when the raw water quality, water treatment agent, pipe network water pH and flow state changes, will damage deposits containing aluminum structure stability, can cause a sudden release of trace metal elements. Based on the review of previous work, this paper gives the control release quantity within the scope of acceptable concentration, trace metal elements in the sediments of the maximal common allow volume (Table 2). It is suggested that the production of aluminum-containing sediments should be controlled to reduce the amount of metal elements accumulated and to reduce the water quality impact caused by the sudden release of metal elements. However, as an important part of pipeline sediment in water distribution system, the existing literature mainly comes from the operation and management practice of water plants. The related test phenomena and research conclusions are mostly based on lead pipe and copper pipe, and less attention is paid to iron pipe, steel pipe and other iron pipe materials. And the pipe network of more than 90% are made by cast iron pipe and stainless steel pipe laying, appeared on deposits containing aluminum and the water quality deterioration caused by the report is far less than is given priority to with lead tube and copper tube, the formation mechanism of proven deposits containing aluminum as well as the influence on the process of piping material way will be the development direction in the future.

Author Contributions: Co-author Wen-dong WANG is the main director of the researcher project, including the study objective and its significance. The first author Xiaoni ZHANG is in charge of analyzing characteristics of accumulation and release of trace metal to aluminum containing scale in drinking water pipe, Jing-hua MENG, Li CHEN and Huan-huan ZUO are in charge of finding and references.

Conflict of Interest: The authors declares that there is no conflict of interest regarding the publication of this paper.

Acknowledgments: This work was supported by City Collage of Science and Technology. Chongqing University and Chongqing HaiRun institute of energy saving research.

References

[1] Snoeyink V L, Schock M R, Sarin P, et al. Aluminum-containing scales in water distribution systems: Prevalence and Composition. Journal of Water Supply: Research and Technology - AQUA, 2003, 52(7):455-474

[2] Schock M R. "Distribution Systems as Reservoirs and Reactors for Inorganic Contaminants." Ch.6 in: Distribution System Water Quality Challenges in the 21st Century. Denver, CO: American Water Works Association, 2005. 105-140

[3] Baylis J R. J. Cast-iron pipe coatings and corrosion. Am. Wat. Wks Assoc., 1953, 45(8):807-822

[4] Cooper R E, Knowles W L. Loss in capacity of a large diameter water pipeline. American Water Works Association 95th Annual Conference. Minneapolis, Minnesota: American Water Works Association Research Foundation, 1975. 2-3

[5] Hudson W D. J. Am. Wat. Wks Assoc., 1966, 58(2):157-164

[6] Hoff J C. The relationship of turbidity to disinfection of potable water. Evaluation of the Microbiology Standards for Drinking Water. Washington, DC: US Environmental Protection Agency, 1978

[7] McGinn R A, Briggs B. Am. City & County, 1979:49-53

[8] Qureshi N, Malmberg R H. J. Am. Wat. Wks Assoc., 1985, 77(10):101-108

[9] Fitch D E, McCollum G. R. J. Am. Wat. Wks Assoc., 1986:35-38

[10] Zimmerman J A. AWWA Seminar on Water Quality Concerns in the Distribution System. Denver, Colorado: American Water Works Association, 1986. 41-70

[11] Fuge R, Pearce N J G, Perkins W T. Unusual sources of aluminum and heavy metals in potable waters. Environ. Geochem. Health, 1992, 14(1):15-18

[12] Shea R D. 'Pig' cleaning water transmission pipelines. Publ. Wks, 1993, 124:54-59

[13] Lauer W C, Lohman S R. American Water Works Association Water Quality Technology Conference. San Francisco, California: American Water Works Association, 1994. 1753-1760

[14] Kriewall D, Harding R, Naisch E, et al. Publ. Wks, 1996, 127(12):28-30, 67

[15] Kirmeyer G J, Pierson G, Clement J, et al. Distribution System Water Quality Following Corrosion Control Strategies. Denver, Colorado: American Water Works Association Research Foundation, 1999

[16] Havics A A. Microscope, 2001, 49(1):1-8

[17] USEPA. Inorganic Contaminant Accumulation in Potable Water Distribution Systems. Office of Groundwater and Drinking Water, 2006

[18] Schock M R. Proceedings Inorganics Contaminants Workshop, Reno, NV, 2004

[19] Clement Bob, Carlson G. Inorganic Contaminants Workshop. Reno, Nevada: AWWA, 2004

[20] Scanlan L. Distribution system water quality changes: A challenge. Annual conference and exposition. Denver, Colorado: American Water Works Association, 2003

[21] Dodge D J, Francis A J, Gillow J B, et al. Association of uranium with iron oxides typically formed on corroding steel surfaces. Environ. Sci. Technol., 2002, 36:3504-3511

[22] USEPA. Potential contamination due to cross-connections and backflow and the associated health risks - an issues paper. USEPA, Office of Groundwater and Drinking water, (8/3/2004).

[23] Fitch D E, McCollum G. R. J. Am. Wat. Wks Assoc., 1986:35-38

[24] Friedman M J, Kathy M, Andrew H, et al. Establishing Site-Specific Flushing Velocities. Denver, Colorado: American Water Works Association Research Foundation, 2003

[25] Havics A A. Microscope, 2001, 49(1):1-8

[26] Munk L, Faure G. Appl. Geochem., Effects of pH Fluctuations on Potentially Toxic Metals in the Water and Sediment of the Dillon Reservoir, 2004, (19):1065-1074

[27] Chen J, Wang F. GeoJournal, Chemical composition of river particulates in eastern China. 1996, 40:31-37

[28] Copeland R, Dionysiou D. Arsenic desorption from drinking water distribution system solids and iron/activated alumina based column media. Proceedings of the 2005 AWWA Annual Conference. San Francisco, 2005

[29] Arai Y J, Evert J E, Donald L S. Journal of Colloid and Interface Science, 2001, 235:80-88

Viser Technology Pte. Ltd.
Research and Application of Materials Science
doi: 10.33142/msra.v2i1.1977

Research Article Open Access

Basic Properties of Pyrolysis Carbon Black of Waste Tyres and Application of Pyrolysis Carbon Black in Transition Layer Rubber of All Steel Radial Tire

Qi LIU[1], Hui LI[1, 2], Jian LI[3]

1.Shenzhou Tires in Ningxia, PingLuo, 753400,China
2.China University of Mining and Technology, Beijing 100039,China;3. Key Laboratory of Intelligent Control and Rehabilitation Technology of the Ministry of Civil Affairs, National Research Center for Rehabilitation Technical Aids, Beijing 100176, China

Abstract:
The main chemical composition of pyrolysis carbon black of waste tires is C, O, Cu, Zn and so on. The content of ash and fine powder in pyrolysis carbon black is high, and the 300% elongation stress is high. The difference between pyrolysis carbon black and furnace black N326, which is commonly used in rubber, is obvious compared with chemical property. The pyrolysis carbon black was used to replace furnace black N326 in the transition layer of all steel load Radial tire rubber through experimental study. It was found that the compression heat generation and dynamic loss (Tanδ) of the blend rubber before and after aging were obviously reduced, the elongation at break and resilience increased, while the tensile stress and tear strength decreased by 100% and 300% , but the hardness and tensile strength changed little before and after aging. According to the latest raw material price calculation, 15 used tire pyrolysis carbon black instead of furnace carbon black N326 used in all steel Radial tire transition layer rubber application, excluding labor costs, electricity and equipment depreciation, a ton of blended rubber saves about $22.86 in production costs.

Keywords: *waste tyre; pyrolysis carbon black; all steel radial truck tire; the transition layer formula; mixing rubber*

With the rapid development of automobile industry and road transportation industry, the demand for tires is increasing day by day, which leads to a sharp increase in the quantity of waste tires [1]-[2]. It is a very promising project to process waste tires into pyrolyzed carbon black for reuse. Through experimental analysis of pyrolyzed carbon black from waste tires, it is found that its main chemical components are C, O, Cu, Zn, S and so on, the ash content is up to 15.0 % , and the 300% tensile stress is up to 7.5 MPA. Compared with the furnace carbon black N326 commonly used in rubber, the chemical property difference is very obvious [3]-[8]. The pyrolysis carbon black of waste tires can greatly reduce the production cost without affecting the basic physical and mechanical properties and processing properties of rubber blends.

1. Experiment

1.1 Main raw materials

Natural rubber :SMR20#, Malaysia; Carbon black :N326, black cat carbon black co., LTD. Pyrolysis carbon black: environmental protection level, shandong Qingdao qindu industry and trade co., LTD. Composite active zinc oxide: nanometer ≥47.0%, fuyang hongli chemical co., LTD. Sulfur accelerator: DZ, shandong shangshun chemical co. LTD.

1.2 Test formulations

The formula of transition layer: SMR20# 100 phr, N326 + Cracked black 58 phr, Zinc oxide 8 phr, Antioxidant RD 1.0 phr, Insoluble sulphur 5.0 phr, Adhesive RA-65 5.0 phr, Accelerator 1.2 phr, other 2.5 phr.

Experimental Protocol (N326/ Pyrolysis carbon black): 1#Scheme: 58 / 0 phr; 2#Scheme: 48 / 10 phr; 3#Scheme: 43 / 15 phr; 4#Scheme: 38 / 20 phr.

1.3 Major equipment and instruments

Qingdao xianrui mechanical & electrical company: XK-160 type mill, XLB-800 type plate vulcanizing machine; Kobe steel, Japan: BB-2 miniature mixer; American alpha: rubber processing analyzer RPA2000, meney viscometer MV2000, rotor-free sulfur transformer MD2000; Brabender company, Germany: carbon black oil absorption meter type C; American strong company: electronic tension machine; Beijing jingwei gaobo co., LTD. ; special surface area tester for carbon black; Oxford, UK: INCA-Energy

X-ray Spectrometer; Scanning electron microscope, Japan: JSM-6700F.

1.4 Sample preparation

The samples were mixed with a closed rubber mixer and an open rubber mixer. First, the samples were mixed in a closed rubber mixer (with a rotating speed of 60 $r\cdot min^{-1}$). The order of feeding was as follows: raw rubber → medicine → carbon black → rubber drainage (with an interval of 40s, rubber drainage at 140℃ or 260s). The curing agent (roller temperature: 45±5℃) was added to the open rubber refining machine, the medicine was completely eaten, the thin pass was taken out 8 times, the sample was left in place for 8 hours, and the vulcanization was carried out on the flat curing machine (curing condition: 151℃*30min).

1.5 Performance testing

All properties of rubber are tested in accordance with national or enterprise standards.

2. Outcomes and discussions

2.1 Comparison of the Chemical Properties of Carbon Black

The comparison of pyrolysis and furnace black chemical property N326 is shown in Table 1. The test results show that. The iodine value and specific surface area of nitrogen adsorption of pyrolysis carbon black NSA (multi-point) were obviously lower than that of furnace black N326. The oil absorption values of pyrolysis carbon black DBP, compressed DBP and 300% elongation stress were higher than those of furnace carbon black N326. The ash content of the pyrolyzed carbon black is obviously higher at 825℃ because it contains not only elements such as C, O, but also metallic elements such as Cu and Zn.

Table 1. Comparison of Chemical Properties of Different Carboniferous Black

Project	Carbon Black N326	Pyrolysis carbon black
Iodine absorption value g/kg	86.68	46.00
DBP Absorption value $10^{-5}m^3/kg$	72.00	86.00
Compressed DBP Absorption		
Value $10^{-5}m^3/kg$	70.10	75.00
Heating reduction 125℃ %	0.53	1.30
Ash content 825℃ %	0.33	15.00
Sieve residue 45μm %	0.05	0.50
300% constant tensile stress Mpa	-2.90	7.50
Nitrogen adsorption ratio surface		
Area NSA（multiple spot）$10^3m^2/kg$	76.68	54.00
Fine powder content %	4.48	130.60

As can be seen from figure 1, In addition to c element, the main components of cracked carbon black are O, SI, S nonmetal and Four metallic elements, Zn, Cu, Ni, AI, The mass fractions of each element was 85.84% C, 4.48% O, 0.12% Si, 2.18% S, 6.54% Zn, 0.38% Cu, 0.36% Ni and 0.10% AI. The Zn element is mainly from zinc oxide, and the S element is mainly from sulfur.

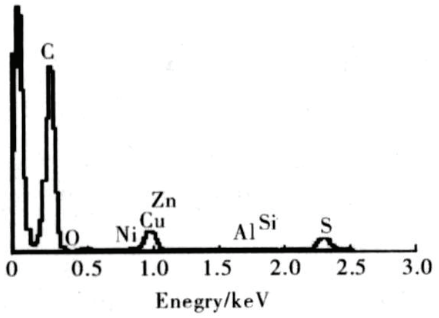

Figure 1. x-ray energy spectrum of pyrolysis carbon black

The SEM images of pyrolysis carbon black of waste tires and furnace carbon black N326(as shown in figure 2) show that the aggregate size of pyrolysis carbon black is obviously larger than that of furnace carbon black N326, and the size of pyrolysis carbon black is about 10 m, the aggregate size of furnace black N326 is about 1.5 m. In comparison, the size distribution of N326 particles is narrow, and the particles of both pyrolysis and furnace carbon black N326 are spherical, but the particles of pyrolysis black are smaller and more closely arranged.

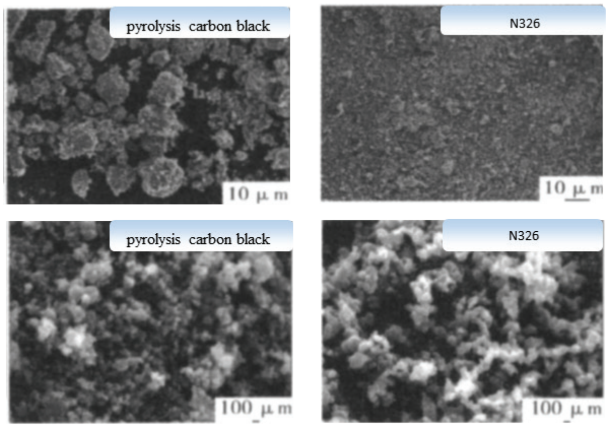

Figure 2. EM SCAN (pyrolysis carbon black, N326 carbon black)

2.2 Performance comparison of blended rubber

2.2.1 Comparison of sulfur mutators

Table 2 sulfur changed instrument test results show that with pyrolysis carbon black in full steel loading meridian tyre transition layer rubber, with the increase of adding amount of mixing rubber Mooney viscosity increasing, the scorch time and T5 (or t10) in pyrolysis carbon black and other attachments instead of furnace black N326 increased to 15 # (scheme 3) when the longest, largest torque MH decrease is sulfide 3 # scheme for the longest time.

2.2.2 Physical performance comparison

The physical and mechanical performance test results of mixed rubber are shown in table 3. With the increase of the number of carbon black added to the rubber in the transition layer of all-steel load radial tire, the constant elongation stress and tear strength of mixed rubber significantly decreased by 100% and 300%. Elongation at break and rebound increase before and after aging; The change of hardness and tensile strength before and after aging is not obvious. With the increase of the amount of pyrolysis carbon black, the compression heat of mixed rubber decreased first and then increased. When pyrolysis carbon black was added to 15 parts (such as scheme 3#), the compression heat of mixed rubber was the lowest. The results show that the dynamic loss factor (Tanδ) decreases with the increase of the amount of carbon black added at the same scanning temperature, and the dynamic loss factor Tan decreases with the increase of scanning temperature, the dynamic loss factor (Tanδ) of rubber blends with the same amount of pyrolysis carbon black was decreased.

Table 2. Comparison of sulfur mutators for mixed rubber under test scheme

Project	Formula number			
	1# Scheme	2# Scheme	3# Scheme	4# Scheme
Menny viscosity [ML(1+4)100℃]	62	64	63	65
Mengniao t5(130℃)/min	17:45	18:12	18:40	18:36
Sulfur meter (151℃*60min)				
ML/(dN·m)	2.14	2.24	2.19	2.10
MH/(dN·m)	30.04	27.87	25.89	25.13
t10 /m:s	04:23	05:00	05:17	05:12
t30 /m:s	06:47	07:31	07:55	07:56
t60 /m:s	10:40	11:16	11:49	11:52
t90 /m:s	19:35	19:35	20:19	20:06

Table 3. Comparison of Physical Properties of Mixed Rubber under Test Scheme

Project	Formula number			
	1# Scheme	2# Scheme	3# Scheme	4# Scheme
vulcanization time (151℃)/min	30	30	30	30
Ageing	Front / Back	Front / Back	Front / Back	Front / Back
Shaw hardnessA	78/87	77/87	77/86	77/86
100 % constant tensile strength /MPa	5.5/0.0	5.3/0.0	4.9/0.0	4.7/0.0
300 % constant tensile strength /MPa	16.4/0.0	15.7/0.0	14.8/0.0	14.0/0.0
Tensile strength /MPa	21.1/6.7	21.3/8.3	21.5/7.1	21.1/7.6
Tear off the elongation /%	396/54	428/74	441/69	449/73
Tear strength /kN/m	80/31	77/27	75/27	75/28
elasticity /%	36/32	36/33	39/36	40/37
proportion /g/cm3	1.174	1.175	1.172	1.174
Compression heat /℃	27.5/34.5	23.0/29.0	22.0/25.5	28.5/32.0
Lag lossTanδ				
40℃	0.194	0.188	0.179	0.169
50℃	0.188	0.181	0.171	0.169
60℃	0.181	0.174	0.163	0.152
70℃	0.175	0.168	0.157	0.145
80℃	0.168	0.160	0.150	0.139
90℃	0.157	0.151	0.141	0.130
100℃	0.145	0.139	0.130	0.119

Remarks: 1) Compression heat generation: stroke 4.45 mm; Load 1MPa; Temperature 55 ℃. 2) Aging conditions: 100 ℃ * 48h.

2.3 Costing of mixed rubber

According to the latest raw material price accounting (as shown in Table 4)，in all-steel load-bearing Radial tire rubber

According to the latest raw material price accounting (as shown in table 4) , when the carbon black of waste tires is used to replace furnace carbon black N326 added to 15 parts in the transition layer rubber of all-steel load Radial tire, without taking into account labor costs, electricity charges and depreciation of equipment, each ton of blended rubber can save about us $22.86 in production costs.

Table 4. Latest price and cost accounting of raw materials

NO.	material	Unit price (USD / kg)	Experimental formulation	Unit price of experimental formula	Current formulation	Unit price of current formula
1	SMR20#	1.25	100.00	125.00	100.00	125.00
2	N326	0.87	43.00	37.30	58.00	50.32
3	Pyrolyss black	0.63	15.00	9.38	0.00	0.00
4	ZnO	2.07	8.00	16.54	8.00	16.54
5	Antiager RD	2.14	1.00	2.14	1.00	2.14
6	Antiager 4020	2.35	0.50	1.18	0.50	1.18
7	Homogenizing agent	0.70	0.50	0.35	0.50	0.35
8	Cobalt decanoate	14.00	0.80	11.20	0.80	11.20
9	Imports HD OT20	2.27	3.00	6.80	3.00	6.80
10	China HD OT20	1.71	2.00	3.42	2.00	3.42
11	RA-65	1.37	5.00	6.86	5.00	6.86
12	DZ	5.08	1.20	6.09	1.20	6.09
13	CTP	4.38	0.20	0.88	0.20	0.88
Total			180.20	227.13	180.20	230.77
Mixed rubber USD/kg			1.26		1.28	
Price differential USD/t			22.86			

3. Conclusion

1) the chemical properties of pyrolysis carbon black and furnace carbon black N326 are significantly different. Pyrolysis carbon black not only contains C, S, O and other elements, but also contains Cu, Zn and other metal elements; The particle size and structure of pyrolysis carbon black are different from that of furnace carbon black N326.

2) transition layer in full steel loading meridian tyre pyrolysis carbon black used in rubber, when pyrolysis carbon black added to 15, mixing rubber compression born before and after aging heat and dynamic loss were significantly lower, higher elongation at failure, the springback, stretch stress and tear strength decreased, other physical properties such as hardness, tensile strength did not change significantly relative.

3) The addition of pyrolysis carbon black from used tyres to the transition layer rubber of Radial tire can save about us $22.86 per ton of blended rubber when equal parts of carbon black are added to 15 parts of carbon black in place of furnace method.

References

[1] zhao wen-jin, liu jia, new progress in pyrolysis recycling of waste tires (2009), rubber technology and equipment 36 (7) : 9-15

[2] cheng yuan, a new bright spot of waste tire recycling -- negative pressure cracking (2008), proceedings of forum on recycling of waste tire resources in China, 2008.11

[3] Shen bo-xiong, Lu feng, Liu ting, modification of carbon black cracking of waste tires (2009), Chemical Journal 60(9): 2327-2331

[4] Du ai-hua, Su chang-yan, Chen Hong, Leng hai-yan, Waste Tire Rift Carbon Black Basic Properties and Its Application in Butyrene Rubber (2009), Synthetic Rubber Industry 31(6): 446-449

[5] Xiao guo-liang, Peng xiao-qin, Gai guo-sheng, ultra-fine crushing and surface modification of carbon black cracking of waste tires and application in NR (2004). Rubber Industry 51(2): 78-82

[6] Peng xiao-qin, Xiao guo-liang, deep processing and application of carbon black cracking of waste tires (2004), Polymer Materials Science and Engineering 20(4): 142-145

[7] guo ying-chen, qiao zhan-ping, waste rubber preparation of fuel oil and carbon black (2001), environmental pollution and prevention 28 (2) : 82-83

[8] liu bao-qing, jiang jia-ling, liu xiao-long, vertical cracking tower for recycling carbon black and fuel oil from waste tires (2004), synthetic rubber industry 27 (1) : 17-20

Viser Technology Pte. Ltd.
Research and Application of Materials Science
doi: 10.33142/msra.v2i1.1978

Research Article Open Access

Effects of Si Content on Microstructure and Mechanical Properties of 8079 Aluminum Alloy

Linhui ZHANG, Xiaoshu KANG, Binnian ZHONG*

Qinghai Provincial Key Laboratory of New Light Alloys, Qinghai Provincial Engineering Research Center of High Performance Light Metal Alloys and Forming, Qinghai University, Xining, 810016, PR China

***Corresponding Author:** *Binnian ZHONG, Qinghai Provincial, China; bnzhong@qhu.edu.cn*

Abstract:
Because of high strength and low breaking rate, 8079 aluminum alloy has become the main material of double zero aluminum foil. However, there are still many problems in the manufacturing process, such as broken belt, pinhole and so on. As the main influencing element, Si has a great influence on the alloy. In this work, the influences of Si with various contents on microstructural evolution and mechanical properties of 8079 aluminum alloy were analyzed by energy dispersive spectrometer (EDS), optical microscope (OM), X-Ray diffraction analyzer (XRD), universal testing machine and Vickers hardness tester. The results showed that the primary Si phase was tiny and dispersed in the alloy when the content of Si is less than 1.3%. As the second phases dispersion strengthening, the Si phase can improve the strength of the alloy. However, when the Si content was too high, the Si phase increased and coarsened. Meanwhile, Fe-rich phase which increased by Si decreased the fine grain strengthening and the second phases strengthening mechanism. The coarse Si phase and the Fe-rich phase are brittle phase, which are easy to become the crack source in the process of material deformation and reduce the strength and toughness of the alloy. The mechanical property test shows that the performance of 8079 aluminum alloy is the best when the Si content is 1.3%.

Keywords: *8079 aluminum alloy; Si; microstructure; mechanical properties*

1. Introduction

8079 aluminum alloy which replaced 1235 aluminum alloy [1] has become the main raw material of double zero aluminum foil (thickness 5~7 μm) due to many advantages such as high tensile strength, small number of pinholes and good elongation [2-4]. But in the actual production process, there are many quality defects such as scratch, microcrack or foreign impurity pressing on the surface of the foil during the last pass of rolling [5,6], which greatly improve the production cost and increase the safety risks of the foil material. What on earth is the cause of these? On the one hand, the operation technology is not mature. The casting parameters and rolling parameters are optimized to change the center segregation and obtain the appropriate thickness of foil products. On the other hand, it is related to the proportion of components. The content of Fe and Si has a greater impact on the comprehensive performance of 8079 aluminum alloy [7].

The mechanical performance of 8079 aluminum alloy depends on the morphology, size and distribution of α-Al and other phases [8]. Fe and Si are the main elements of 8079 aluminum alloy [9-11], which have significant influence on its microstructure and mechanical properties. The solubility of Fe in 8079 aluminum alloy is relatively low, and the second phases mainly composed of Al_3Fe will be enriched at the grain boundary of the alloy [12]. The Fe-rich phases with needle like or platy shape are leading to matrix splitting, and then making the plasticity of aluminum foil decrease during rolling. The Fe-rich phase also becomes the source of crack propagation which develops into pinhole [13,14]. However, proper Fe content has the effect of fine grain strengthening and second phases strengthening, which makes 8079 aluminum foil have higher tensile strength, elongation and reduces surface defects such as pores and pinholes. At the same time, Si can also reduce the number of pinholes in aluminum foil. It has been shown that the residual amount of solid solution Si in the alloy is less, and most of Si is easy to form (AlFeSi) phase with A1 and Fe [15,16].

The second phases in the double zero aluminum foil blank mainly consists of α-(AlFeSi) phase of skeleton and round particles, β-(AlFeSi) phase of needle and disk, and θ-($A1_3Fe$) phase of needle compound. The θ phase is the only Al-Fe equilibrium phase, and the α-(AlFeSi) phase is easy to be broken in the process of aluminum foil deformation [17,18]. The solubility of larger acicular β-(AlFeSi) phase in aluminum matrix is smaller during homogenization. During the rolling process of 8079 aluminum alloy foil, the hardness and strength of the foil increase with work hardening, while the plasticity decreases. When the size of the acicular phase (β, θ) is larger than 5 μm, it is easy to become a crack source and then expand into a pinhole. In addition, the rolling performance is also related to the distribution of the second phases in the Al matrix. If the distribution of the second phases in the matrix is not uniform, the deformation will be uneven, then pinholes will be formed, and the work hardening rate of the alloy will be increased [19]. For aluminum foil materials, the grains are two-dimensional distribution and the grain boundary is plane network distribution. A small amount of the second phases at the grain boundary will still destroy its overall continuity. So the precipitation of the second phases at the grain boundary should be minimized in the production of aluminum foil [20].

Therefore, the effective way to improve the mechanical properties of 8079 aluminum alloy foil is to reduce the grain size and control the generation of harmful second phases [21]. The content of Si in 8079 aluminum alloy is small. The purpose of this paper is to study the effect of Si content on the microstructure and mechanical properties of 8079 aluminum alloy, improve the comprehensive properties of 8079 aluminum alloy, optimize the composition range of 8079 aluminum alloy aluminum foil blank, and steadily improve the quality of aluminum foil.

2. Experimental

The Al and Al-Mg, Al-Si, Al-Fe, Al-Cu alloys ingots with a mass fraction of Si were 0% and 1.1%~1.5% were melted up to 750℃ in a 5 kg ceramic crucible by using an electrical resistance furnace. After they were completely melted, being stirred and cleaned off, the melt was poured into a steel mold that was preheated to 200℃. The casting (φ40mm, approximately 2kg) was subsequently cut into 10 ×10 ×10 mm and dog-bone-shaped blocks by wire cutting machine. Each square specimen was polished and then etched by Keller's reagent for about 40 s at room temperature.

The microstructures of the specimens were examined by optical microscope (OM). The distribution of the elements in some of the samples was investigated by energy dispersion scope (EDS). The phase composition in 8079 aluminum alloys was measured by X-Ray diffraction analyzer (XRD). The Vickers micro-hardness of the samples was tested by the Vickers Indenter (HR-150B) at room temperature with a load of 200 g and a dwell time of 10 s. After the bone sample was polished, tensile experiments were carried out at room temperatures using an Instron machine with a constant displacement rate of 0.5 mm/min. In this work, the number of tested samples was three to five.

3. Results and discussion

3.1 Microstructure analysis

Figure 1 is XRD pattern of 8079 aluminum alloy with different Si content. It can be observed that there is α-Al phase in the all alloys. When the Si content is less than 1.4%, there is only the peak of aluminum phase in the diffraction pattern, the content of other phases below detection range in the alloy is less. When the Si content is 1.5%, the peak strength of α-Al phase decreases obviously, the Si phase and (AlFeSi) phase increase. It may be that the Si phase grows up and the aggregation of Si particles often blocks the continuous contact of Al phase and produces more (AlFeSi) phase with the increase of Si content.

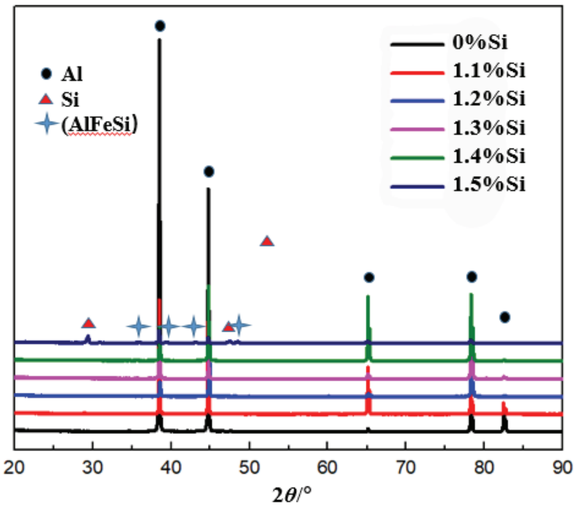

Figure 1. The XRD pattern of 8079 alloy with different Si content.

Figure 2 illustrates the evolution of the size and morphology of α-Al and Si phases in 8079 aluminum alloy with different Si content. Figure 2A indicates the size of α-Al is about 80μm, most of the grains are columnar implies that the property of alloy worse than that of equiaxed crystal. Figure 2B shows the Si phase with needle like is less and mostly distributed in the intergranular as the second phases with 1.1%Si. When the Si content increased to 1.2% and 1.3%, the grain size decreases obviously, while the Si phase with needle or particle increases, and distributed in the intergranular and grain boundary as shown in figure 2B and 2C. Further increasing the Si content (figure 2D), the grain size of the Al phase will not change any more, but the Si phase will grow up. When the Si content is 1.5% (figure 2E), the grain size of the α-Al phase is about 50 μm, and the Si phase with the size of growth and the number of increases distributed in the intergranular and the grain boundary. That is to say, the more Si content, the more conducive to the growth of Si phase.

Figure 3 shows the EDS images of 8079 aluminum alloy with 1.3% Si content. It can be seen that some casting defects in the sample, Mg and Cu are evenly distributed in the alloy, and they form stable intermetallic compounds. The distribution of Al, Si and Fe is uneven, and the segregation of Si and Fe are the segregation to the grain boundary which contrary to Al. It may be that, with the increase of Si content, the number of Si rich particles or Si phase formed causes the increasing of Si phase. The

Al phase cannot well stabilize the Si phase, which lead to uneven particle distribution and the formation of iron Fe second phases. Moreover, the deposited Si particles may block the connection structure of Al matrix, resulting in more defects in the material.

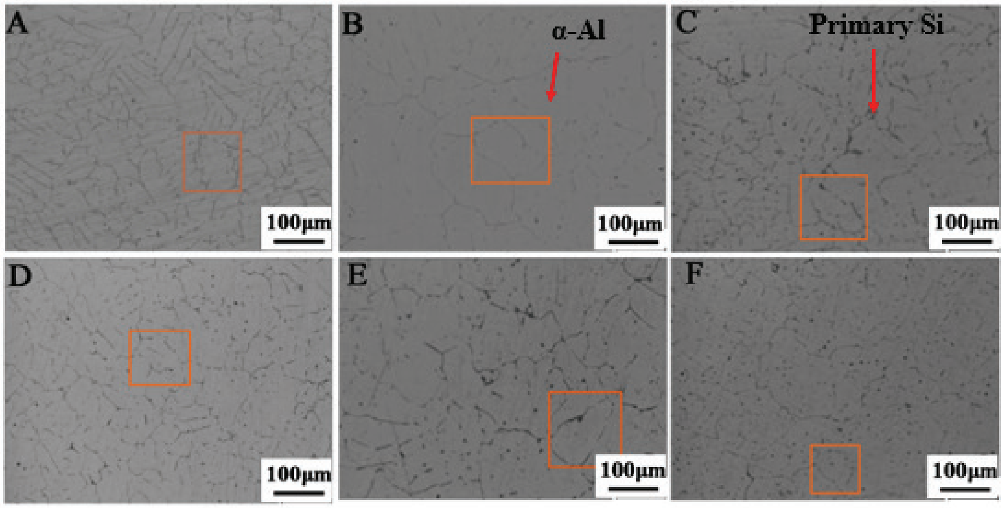

Figure 2. OM images of the 8079 alloy with different Si content, A: 0%Si B: 1.1%Si, C: 1.2%Si, D: 1.3%Si, E: 1.4%Si, F: 1.5%Si.

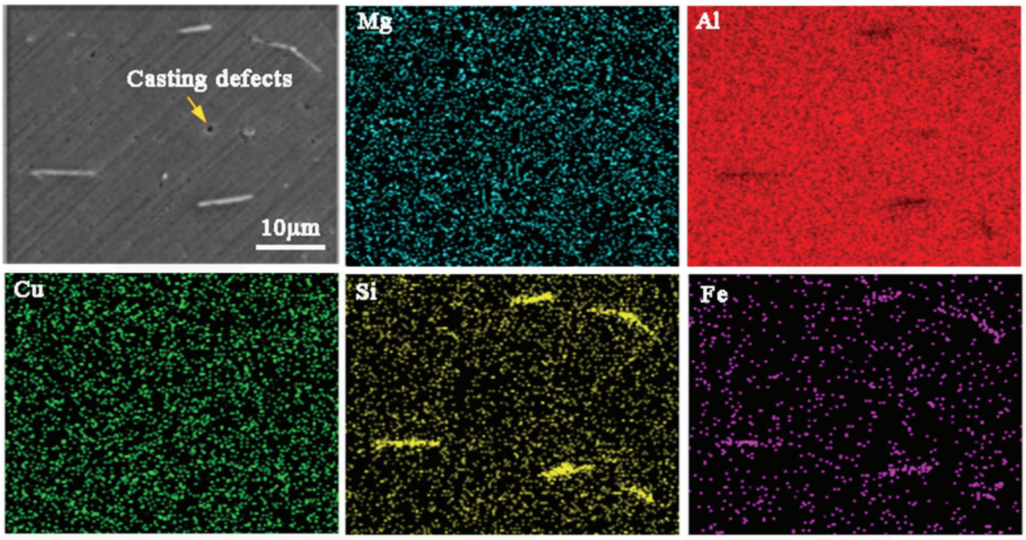

Figure 3. EDS analysis of 8079 alloy with 1.3% Si content.

3.2 Mechanical properties

Figure 4 indicates the tensile strength and elongation of 8079 aluminum alloy with different Si content. The alloy has high plasticity and low strength without Si. The tensile strength and elongation of the alloy with 1.1% Si content are about 130 MPa and 28%, respectively. The tensile strength of the alloy with 1.2% Si content rise to 143 MPa, and the elongation is similar (about 28%). When Si content is 1.3%, the tensile strength and elongation are 152 MPa and 35%, respectively. Compared to the 1.1%Si alloy, the tensile strength and elongation of 8079 aluminum alloy are enhanced by 16.9% and 25%, respectively. However, the tensile strength of the alloy with 1.4% and 1.5% Si content are reduced to 135 MPa and 130 MPa, and the elongation reduced to about 33%. So the tensile strength and elongation of 8079 aluminum alloy are first increase and then decrease with the increase of Si content. When the Si content is small, the primary Si is mostly in the alloy, its microstructure is fine, and its distribution is even or dispersive. The Si phase can be used as the second phases of dispersion distribution, which greatly improving the strength of the alloy. When the Si content is higher than 1.3%, the fine grain strengthening and the second phases strengthening mechanism which play the main role in alloy will decrease because of the increase of Si phase, coarsening and Fe-rich phase. The coarse Si phase and the Fe-rich phase (AlFeSi) are brittle phase, which are easy to become the crack source in the process of material deformation.

In addition, with the increase of Si content, there are more voids which exists stress concentration in the alloys are suitable for the formation and growth of microcracks, which leading to the fracture of materials and reducing the strength and toughness of the alloy.

The hardness of 8079 aluminum alloy with different Si content are indicated in Table 1. It is shown that the hardness of alloy with 1.1%Si is 36.8$HV_{0.2}$ is like without Si. When the Si content is 1.2% and 1.3% , the hardness of alloys is raised to 41$HV_{0.2}$. But there is a downward trend when the Si content increase, the growth trend of Si phase is larger, and the partial segregation of Si particles in the material is easy to occur. This kind of segregation often blocks the continuous contact of Al phase, and the Al liquid fills the pores between Si particles. This phenomenon leads to obvious defects in the material, then the mechanical properties of the material is declined.

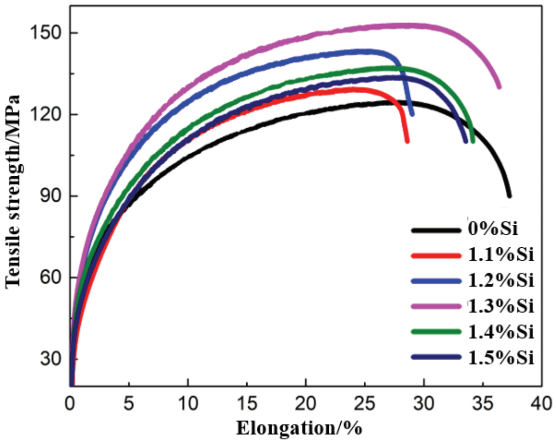

Figure 4. The tensile properties of 8079 alloy with different Si content.

Table 1. The hardness of 8079 aluminum alloy with different Si content

Si wt%	0	1.1	1.2	1.3	1.4	1.5
Hardness（$HV_{0.2}$）	35.7±1	36.8±1	41.1±1	41.2±2	36.9±2	31.9±1

4. Conclusion

The thickness of 8079 Al alloy is gradually thinning due to conserve energy and reduce emissions, and the processing technology of double zero Al foil is more intelligent, which requires that the raw materials of aluminum foil have better mechanical properties. Si is the main component of the material, which has a great influence on the grain size and phase distribution. By the analysis and discussion, the conclusions were drawn as follow:

(1) The addition of Si can refine primary α-Al phase and the mean grain size was decreased by 33.3% from 75μm to 50μm.

(2) When the Si content was less than 1.3%, the Si phase as the second phases was less which needle like, mostly distributed in the intergranular. When the Si content was more than 1.3%, the Si phase grown up, the amount of Si increased at the intergranular and grain boundary. The more Si content, the more favorable for the growth of Si phase.

(3) When Si content was 1.3%, the tensile strength, the elongation and the hardness with the highest value were 152MPa ,35% and 41.2$HV_{0.2}$, respectively.

Acknowledgments: This work was financed by Aluminum Corporation of China Limited Qinghai Branch (Grant No. K151879), and the Natural Science Foundation of Qinghai Province under Grant No. 2018-ZJ-957Q and No. 2020-ZJ-933Q.

Author Contributions: Linhui ZHANG took out the original ideas, carried out all the experiments and prepared the draft of the manuscript. Binnian ZHONG modified the manuscript and gave suggestions in the discussion. Xiaoshu KANG carried out the experiments.

Conflict of Interest: The authors declare that there is no conflict of interest regarding the publication of this paper.

References

[1] Roy. R. K, Kar. S, Das. K, et al. A study of precipitation and recrystallization behavior of aluminum alloy AA1235[J]. Journal of Materials Science, 2006, 41 (4): 1039-1045.

[2] Lentz, M., G. Laptyeva, and O. Engler, Characterization of second-phase particles in two aluminium foil alloys. Journal of Alloys and Compounds, 2016. 660: 276-288.

[3] Schmidt C W, Mortensen D, and Harryhausen K, Influence of Process Conditions on Segregation Behavior in Twin-Roll Casting of an Al-Fe-Si-Alloy[J]. Light Metals, 2017: 811-819.

[4] Zhang J, Pan F, Zuo R, et al. The low temperature precipitation in commercial-purity aluminum sheets for foils[J]. Journal of Materials Processing Technology, 2008, 206(1-3): 382-387.

[5] Lentz M, Laptyeva G, and Engler O, Characterization of second-phase particles in two aluminum foil alloys, Journal of Alloys and Compounds, 2016, 660(5): 276-288.

[6] Birol Y, Formation of pinch marks on pack rolled aluminum foil[J], Engineering Failure Analysis,2013, 28(3): 82-89.

[7] Wei C, Pizhi Z, Qi Z, et al. Effect of degreasing annealing temperature on mechanical properties of continuous casting and rolling AA8079 aluminum alloy foil[J]. heat treatment of metals, 2015, 40(7):155-159.

[8] Qinglin Li, Yuqian Zhu, Shang Zhao, et al. Influences of Fe, Mn and Y additions on microstructure and

mechanical properties of hypoeutectic Al–7%Si alloy[J]. Intermetallics, 2020, 120: 106768.

[9] Schmidt C. W, Mortensen. D, and Karhausen. K, Influence of Process Conditions on Segregation Behavior in Twin-Roll Casting of an Al-Fe-Si-Alloy[J]. Light Metals, 2017, 811-819.

[10] Zhang J, Pan F, Zuo R, et al. The low temperature precipitation in commercial-purity aluminum sheets for foils[J]. Journal of Materials Processing Technology, 2008, 206(1-3): 382-387.

[11] Roy. R. K, Kar. S, Das. K, et al. A study of precipitation and recrystallization behavior of aluminum alloy AA1235[J]. Journal of Materials Science, 2006, 41 (4): 1039-1045.

[12] D. Liang, W. Jie, H. Jones. The effect of growth velocity on primary spacing of Al3Fe dendrites in hypereutectic Al-Fe alloys[J]. Journal of Crystal Growth, 1994, 135(3-4): 561-564.

[13] C.-Y. Ban, Y. Han, Q.-X. Ba, et al. Effect of magnetic field on the morphology and distribution of Al3Fe phase in hypereutectic Al-Fe alloy[J]. Journal of Northeastern University, 2010, 31(9): 1278-1282.

[14] Belmares-Perales S, M. Castro-Román, Herrera-Trejo M, et al. Effect of cooling rate and Fe/Mn weight ratio on volume fractions of α-AlFeSi and β-AlFeSi phases in $Al_{7.3}Si_{3.5}Cu$ alloy[J]. Metals & Materials International, 2008, 14(3): 307-314.

[15] V. Stefániay, á. Griger, Turmezey T. Intermetallic phases in the aluminium-side corner of the AlFeSi-alloy system[J]. Journal of Materials Science, 1987, 22(2): 539-546.

[16] Kuijpers N C W, Vermolen F J, Vuik C, et al. The dependence of the β-AlFeSi to α-Al(FeMn)Si transformation kinetics in Al-Mg-Si alloys on the alloying elements[J]. Materials Science & Engineering A Structural Materials, 2005, A394(1/2): 9-19.

[17] V. Stefániay, Á. Griger, T. Turmezey. Intermetallic phases in the aluminium-side corner of the AlFeSi-alloy system[J]. Journal of Materials Science volume,1987, 22: 539–546.

[18] R.J.Davues, V.Randle, G.J.Marshall. Continuous recrystallization-related phenomena in a commercial Al-Fe-Si alloy[J]. Acta Materialia, 1998, 46(17): 6021-6032.

[19] Ahmet Can, Hüseyin Arikan, Kadir Çýnar. ANALYSIS OF TWIN-ROLL CASTING AA8079 ALLOY 6.35-µm FOIL ROLLING PROCESS[J]. Materials and technology,2016, 50 (6): 861–868.

[20] Christoph Heering, Xiaoli Li, Markus Bambach, et al. Physical and Numerical Simulation of Cold Rolling of an AlFeSi Alloy in Consideration of Static Recovery[J]. Advanced Engineering Materials, 2010, 12(3): 141-146.

[21 Wei C, Pizhi Z, Qi Z, et al. Effect of degreasing annealing temperature on mechanical properties of continuous casting and rolling AA8079 aluminum alloy foil[J]. Heat Treatment of Metals, 2015, 40(7): 155-159.

Viser Technology Pte. Ltd.
Research and Application of Materials Science
doi: 10.33142/msra.v2i1.2023

Research Article Open Access

Comparative Analysis of Rheological Properties and Modification Mechanism of SBS-Graphene Composite Modified Binder

Jiangmiao YU[1], Nikun YANG[1], Huayang YU[1*], Svetlana Shekhovtsova[2], Evgenii Korolev[2]

1 School of Civil Engineering and Transportation, South China University of Technology, Guangzhou, China
2 Building materials and materials science, National Research Moscow State University of Civil Engineering, Moscow, Russia

Corresponding Author: *Huayang YU, Wushan Road, Tianhe District, Guangzhou 510000, China; huayangyu@scut.edu.cn*

Abstract:
SBS (styrene-butadiene-styrene block copolymer) has been widely used in pavement industry as an asphalt modifier. Nanomaterials can further enhance the performance of SBS modified asphalt. However, rare studies investigate the feasibility of using graphene as a performance enhancer of SBS modified asphalt. To fill this gap, comprehensive experimental tests including chemical and mechanical test were carried out on SBS-graphene modified asphalt and SEBS (styrene-ethylene-butylene-styrene block copolymer, which is a hydrogenated polymer of SBS) modified asphalt. Graphene with different dimensions and contents was taken into consideration in this study. Based on the experimental work, it can be concluded that graphene improves the mid-temperature performance of SBS modified asphalt. Compared with two-dimensional graphene, three-dimensional graphene has a greater advantage and the enhancement effect increases with the increase of its dosage. In addition, the cross-linked structure of SBS-graphene composite improves the distribution of SBS in asphalt, which improves the overall performance of SBS modified asphalt.

Keywords: *SBS-graphene modified asphalt; chemical analysis; rheological properties*

1. Introduction

Base asphalt, a pavement material, is prone to be defected such as rutting, cracking and aging, which limits its wide application in road construction. Modification of asphalt can significantly improve the performance of pavement. SBS (styrene-butadiene-styrene block copolymer) modified asphalt is widely used due to its high temperature stability and low temperature crack resistance. However, SBS is generally unevenly dispersed in the binder, which results in road surface damage of varying degrees under the multiple effects of long-term driving loads and natural factors [1-3]. In recent years, many studies have focused on the effect of unsaturated hydrogen bond content in SBS on asphalt pavement performance [4,5]. At the same time, it is widely reported that other nano materials are added to SBS modified asphalt to promote cross-linking between SBS and asphalt molecules and to improve the high temperature resistant rutting and low temperature cracking performance of asphalt pavement [6,7].

SEBS (styrene-ethylene-butylene-styrene block copolymer) is a hydrogenated polymer of SBS, which is a linear tri-doped copolymer with a polystyrene end segment and an ethylene-butene copolymer obtained by hydrogenating polybutadiene as an intermediate elastic block. SEBS does not contain unsaturated double bonds and therefore has good stability [8-10].

Graphene is a monoatomic graphite layer. It is a honeycomb two-dimensional crystalline material that is infinitely extended by sp^2 hybridized carbon atoms. Three-dimensional graphene is composed of two-dimensional graphene and its porous structure gives it higher mechanical strength, electrical conductivity and specific surface area. Since its discovery in 2004 [11], graphene has attracted great attention from scientists, and researchers have reported its potential applications in electronics, energy storage and sensors. Each carbon atom in the graphene forms a covalent bond with the other three adjacent carbon atoms and the remaining one of the p-orbital electrons forms a π bond, while the π electron can move freely. These properties make it compatible with SBS and asphalt [12,13]. This unique structure that provides a large amount of electrons will be a potential bridge between asphalt and SBS compared to other inorganic nanomaterials [14,15].

In this paper, SBS modified asphalt was used as the control group and the SBS-graphene modified asphalt and SEBS modified asphalt were comprehensively evaluated. In order to obtain better experimental results, SBS-graphene composite modifiers with different graphene contents were prepared by chemical coupling method. The modified asphalt is subjected to rheological and chemical tests respectively and the physical and rheological properties are characterized by including penetration, softening point, rutting factor, fatigue factor, etc. Gel permeation chromatography (GPC) analysis and Fourier transform infrared spectroscopy (FTIR) analysis were used to characterize the molecular weight distribution and chemical functional groups, revealing the composite modification mechanism of graphene-SBS modified asphalt.

2. Materials and Methods

2.1. Materials

In this study, the basic asphalt was suitable for Hong Kong with a penetration grade of 60/70 (Pen 60/70) and supplied by Xin Yue Transportation Technology Co., Ltd., Guangzhou. All graphene are supplied by GAC (Guangzhou Automobile Group Co., Ltd) Automotive Engineering Research Institute, including three-dimensional structure and two-dimensional structure. Among them, two-dimensional graphene (2DG) is prepared from natural flake graphite by a simple redox method [12,13]. In detail, first, the nitric acid and the sulfuric acid are disposed in a certain proportion of the mixture and fully contacted with each layer of the graphite and the interlayer spacing of the graphite will increase with the generation of the gas to obtain the expanded graphite; then, the treated expanded graphite is placed in a strong oxidizing agent solution with a certain concentration and stored at a low temperature for a sufficient time; the residual oxidizing agent is removed by adding hydrogen peroxide, then the sample is moved to a vacuum drying oven for drying; finally, the sample was configured into a certain proportion of graphite oxide solution and sonicated to obtain a uniformly dispersed graphene oxide colloid and 2DG was obtained. Three-dimensional graphene (3DG) is prepared by metal catalytic epitaxial growth [16,17]. Under ultra-high vacuum conditions, a certain amount of hydrocarbons are introduced into a catalytically active transition metal matrix (an alloy of copper and iron) and the 3DG is obtained by adsorbing a gas at a high temperature by catalytic dehydrogenation. The basic parameters of graphene are shown in Table 1.

SBS with linear structure was provided by Changzhou Lubis New Material Technology Co., Ltd, while SEBS was provided by Kraton Polymers, inc. SBS and SEBS are separately added to Pen 60/70 as modifiers to further explore the differences before and after hydrogenation. At the same time, SBS and graphene are chemically coupled by KH-570 (Silane Coupling Agent) at room temperature and dried to prepare SBS-graphene composite modifier. For the convenience of expression, the SBS-graphene composite modifiers prepared by different 2DG dosages are named 2DG-L and 2DG-H, respectively. The same method is used to prepare 3DG-L and 3DG-H. All modifiers are encoded and listed in Table 2.

Table 1. Basic parameters of graphene.

	Layers	Conductivity (S/cm)	Bulk Density (g/cm^3)	Tap Density (g/cm^3)	Carbon Content (wt%)	Melting Point (°C)	Exterior
2DG	1-3	450-700	0.03-0.04	0.05-0.06	>98.5	>3000	Gray-black powder
3DG	5-10	800-1300	0.03-0.04	0.04-0.05	>95	>3000	Black powder

Table 2. Modifier composition.

Modifier Code	Graphene Content		SBS Content	SEBS Content	Hybrid Method
	Two-Dimensional	Three-Dimensional			
SBS	-	-	100.00 wt %	-	-
SEBS	-	-	-	100.00 wt %	-
2DG-L	0.05 wt %	-	99.95 wt %	-	Chemical coupling
2DG-H	-	0.10 wt %	99.90 wt %	-	
3DG-L	0.05 wt %	-	99.95 wt %	-	
3DG-H	-	0.10 wt %	99.90 wt %	-	

2.2. Sample Preparation

In order to gain the modified asphalts, high-speed shear mixer was utilized, whose purpose is to make the achievement about homogenous dispersion of the additives in the control asphalt. Considering the recommendation of manufacturer (GAC Automotive Engineering Research Institute), the modifier's dosages in this study are 4% by weight of asphalt. Here are the preparation processes listed as follows. (1) Heating control asphalt under the temperature of 170 °C; then, adding modifier into the control asphalt and stirring them for 10 minutes. (2) Using high-speed shear mixer to mingle the modifier with asphalt at 160°C and 8000 rpm/min for an hour. The modifier code is used to represent the corresponding modified asphalt.

2.3. Experiments

2.3.1. Standardized Performance Tests

Supervised by the ASTM D5 and ASTM D36, penetration test at 25 °C and softening point quiz were conducted, separately. The former evaluates the asphalt binder's consistency, while the later estimates the binder performance at high service temperature. With the intention of determining the viscosities of modified asphalts with the temperature of 135, 160, and 165 °C, separately, the rotational viscometer (RV, RVDVII+, Brookfield Eng Labs Inc., Stoughton, MA, United States), which guided by AASHTO T316-13 method, was engaged.

A dynamic shear rheometer (DSR, Malvern instruments Inc., Santa Ana, CA, United States) was used in the different rheological tests. Superpave rutting factor (G*/sinδ, for both unaged and RTFO aged samples) and non-recoverable creep compliance (J_{nr}, for RTFO aged samples only), as two cardinal elements in high temperature performance, were utilized in order to adjudicate property. The Multi-stress Creep Recovery (MSCR) test is designed to determine Jnr in accordance with ASTM D7405. During the test, 10 cycles were carried out at stress levels of 0.1 KPa and 3.2 KPa, respectively. In each test cycle, a creep load was applied for 1 second and recovered for 9 seconds.

The fatigue performance test was supervised on a Pressurized Aging Vessel (PAV) aged adhesive at a frequency of 10 rad/s, which utilized the 8mm diameter plates and 2mm gap. The fatigue factor tests were started at 25°C with a decrement of 3°C until the fatigue factor was larger than 5000KPa. In order to evaluate the fatigue properties of the asphalt adhesive, the fatigue resistance parameter (G*·sinδ) and failure temperature (T fatigue) were employed. With regard to the linear amplitude sweep (LAS) test, PAV aged samples was also fit for this operation. At the LAS test, a frequency sweep was first performed followed by a linear amplitude strain sweep in order to make determination about the cycles to failure denoted as N_f. Then in the viscoelastic continuum damage (VECD) model, there is the fatigue failure's definition that is the 35% reduction of the initial modulus in the LAS test. There were three replicates prepared for each type of binder in these tests.

2.3.2. Frequency Sweep

Frequency sweeps in the linear viscoelastic range were measured at 4°C, 16°C, 28°C, 40°C, 52°C, 64°C and 76°C, respectively, from 0.1(rad/s) to 100(rad/s) to evaluate the shear-deformation performance and temperature sensitivity of asphalt binders at the basis of time-temperature superposition principle. The parallel plates were prepped for the tests with diameter of 25mm and gap of 1mm. In this test, one specimen was utilized.

2.3.3. Chemical Tests

The mechanism of adhesive was investigated by Gel Permeation Chromatography (GPC, Agilent 1260, Agilent Technologies Inc., California, USA) and Fourier transform infrared spectroscopy (FTIR, VERTEX 70, BRUKER, Germany). In order to assay the influences of graphene, SBS and SEBS on molecular weight distribution of asphalt liquid components in detail, GPC test was conducted and the infrared spectroscopy (FTIR) figured out the feature of chemical bonds and functional groups of asphalt. Two samples were used in here.

3. Results and Discussion

3.1. Workability

Table 3 shows the results of the penetration and softening point tests. The results clearly show that all modified asphalts have lower penetration and higher softening point than base asphalt, indicating that the SBS-graphene composite modifier and SEBS can make the asphalt more viscous and stable at high temperatures.

In detail, the penetration of all the modified asphalts was at the same level, the addition of graphene had no significant effect on the asphalt. Compared with SBS, all the graphene-added binders have a lower softening point, which mirrored the fact that the addition of graphene affects the high-temperature properties of SBS to some extent. Nevertheless, SEBS has a higher softening point and a slightly lower permeability than SBS, which signified that SEBS can make asphalt harder and more stable than SBS at high temperatures.

At the same time, the viscosity of modified asphalt at 135°C is much higher than that of pen60/70, but this may be the influence of polymers from the composition analysis of the modifier. It is worth noting that SEBS has a viscosity 20% higher than SBS at 135°C. This is the fact that SEBS has a different compatibility with the light components in the bitumen after hydrogenation, which makes it easier to form a polymer network. Since the viscosity value of all modified asphalt is below 3000cp, their mixture can be compacted at 160°C, which is based on the AASHTO standard.

Table 3. Details of laboratory tests.

Sample ID	Penetration (0.1mm)	softening point (°C)	Rotational viscosity (cP)		
			135°C	160°C	165°C
Pen60/70	64.5±1.4	47.9±0.2	404.5±2.5	-	-
SBS	44.0±0.9	56.2±0.2	1032.5±37.5	357.5±12.5	297.5±12.5
SEBS	41.8±0.2	59.2±0.2	1205.0±105.0	417.5±42.0	347.5±42.0
2DG-L	44.3±0.4	54.6±0.2	965.0±80.0	330.0±20.0	280.0±20.0
2DG-H	45.0±0.5	54.4±0.2	962.5±72.5	348.8±1.5	288.8±1.5
3DG-L	43.0±0.9	54.3±0.1	970.0±50.0	338.8±1.0	278.8±1.0
3DG-H	44.7±1.0	52.8±0.1	995.0±75.0	355.0±5.0	285.0±5.0

[1] The numbers after "±" are standard deviations.

3.2. Rutting Resistance

The rutting factor test results for the binder is displayed in figure 1, which shows that all modifiers have a significant effect on improving rutting resistance. In the unaged state, SEBS has the highest destruction temperature. However, after a short period of aging, SBS's rutting performance is better than SEBS. Significantly, the rutting performance of SBS modified asphalt after aging is better than that before aging, while the rutting resistance of graphene added asphalt after aging is lower than that before aging, which proves that graphene is not conducive to rutting performance durability.

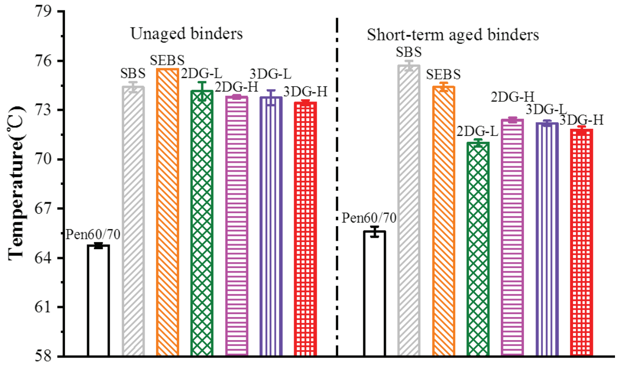

Figure 1. Rutting factor results.

Table 4 presents the MSCR test results. Drawing the conclusion that only the J_{nr} difference of SEBS did not meet the requirement of AASHTO TP70-13 i.e., < 75%. The reason is that the extremely low J_{nr} values was applied at the stress of 0.1kPa [18]. Based on the J_{nr}3.2 values, Two-dimensional graphene and three-dimensional graphene had negative effects on rut resistance, while the rut resistance of SEBS was better than that of SBS. This is coherent with the results of rutting factor test before aging. Based on the J_{nr}0.1 value, as the amount of graphene is increased, the rutting resistance of the binder is slightly enhanced, which indicates that graphene can make the asphalt harder. On the whole, under the same graphene content, the negative effect of two-dimensional graphene on rutting resistance was more significant.

3.3. Fatigue Resistance

The fatigue failure temperatures and the relationship between the G*sinδ value and the test temperature are illustrated in figure 2a and figure 2b, respectively. AASHTO M320 specified that the fatigue factor, G*sinδ, should be less than 5 MPa to pass a performance grade test at a specific temperature. As shown in the figure, there is a negative relationship between the fatigue failure temperature and fatigue resistance, that is, the higher the fatigue failure temperature is, the poorer the fatigue resistance the test binder has. As shown in figure 2a, the fatigue failure temperature of SBS is 3.0 °C higher than that of Pen60/70, which construes that SBS brings poor fatigue resistance, but graphene has a positive effect on the fatigue performance of SBS modified asphalt. The failure temperatures of 3DG-L and 3DG-H are 0.3-0.5 °C lower than that of Pen60/70. In contrast, the failure temperatures of 2DG-L and 2DG-H are 1.5-2.0 °C higher than that of Pen60/70, which demonstrates that three-dimensional graphene has a superior fatigue resistance.

Table 4. MSCR test results.

Sample ID	J_{nr}			% Recovery	
	0.1 kPa (kPa−1)	3.2 kPa (kPa−1)	Jnr% Diff	0.1 kPa (kPa−1)	3.2 kPa (kPa−1)
Pen60/70	4.514 ± 0.166	5.007 ± 0.154	11.0 ± 0.6	0.7 ± 0.4	−0.5 ± 0.2
SBS	0.749 ± 0.021	1.162 ± 0.036	55.2 ± 0.4	31.5 ± 0.6	8.4 ± 0.1
SEBS	0.336 ± 0.012	0.906 ± 0.088	168.6 ± 16.6	65.7 ± 1.8	23.0 ± 1.5
2DG-L	1.132 ± 0.009	1.662 ± 0.044	46.9 ± 3.4	24.4 ± 1.3	3.8 ± 0.3
2DG-H	0.999 ± 0.014	1.523 ± 0.016	52.5 ± 0.6	28.6 ± 0.2	5.1 ± 0.2
3DG-L	0.952 ± 0.011	1.183 ± 0.007	24.2 ± 0.7	15.3 ± 1.7	4.0 ± 0.1
3DG-H	0.883 ± 0.109	1.253 ± 0.055	43.4 ± 12.8	19.4 ± 5.3	5.1 ± 0.2

[1] The numbers after “±” are standard deviations.

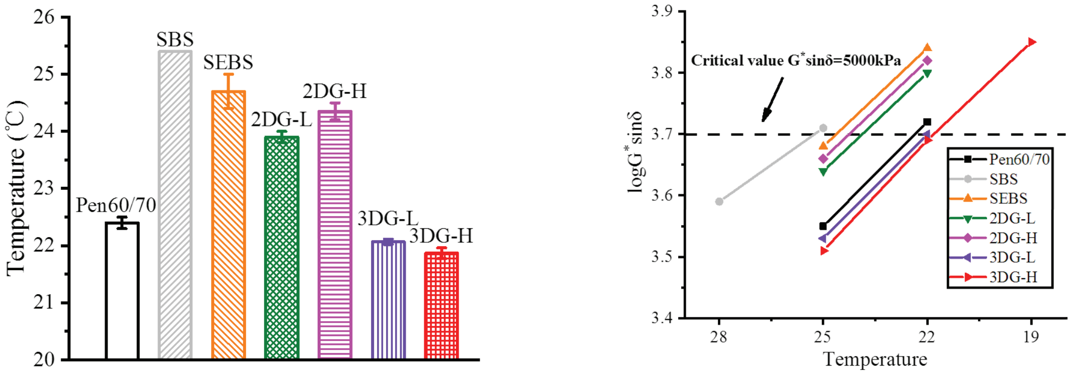

(a)

(b)

Figure 2. Fatigue performance of asphalt binders: (a) failure temperatures and (b) logarithm of G*sinδ values.

Higher cycles to fatigue (N_f) refer to better resistance of fatigue cracking. It can be seen from Table 5 that the N_f value of all the modified asphalts is higher than that of the original asphalt at the strain levels of 2.5% and 5%. Inconsistent with the fatigue factor results, all graphene have a negative impact on the fatigue properties of SBS in the LAS-based evaluation and increase with the increase in graphene content. Compared with SBS and SEBS, SEBS has better fatigue performance at higher strain levels and there is reason to believe that SEBS is more suitable for heavy traffic roads.

3.4. Low Temperature Cracking Resistance

Table 6 presents the consequence of the stiffness and m-values of test binders under the test of BBR. There is an AASHTO T313 elaborating the criterion that the m-value should exceed 0.3 and the maximum of stiffness value is 300MPa at a certain temperature level. The effect on low-temperature cracking is higher stiffness value. Table 6 shows that 2DG plays a positive role in the low-temperature properties of asphalt, but this positive effect will be weakened with the increase of the content of the 2DG; significantly, the lower content of 3DG has a negative effect on the asphalt's low-temperature. With the increase of the content of 3DG, the negative effect will turn into a positive; the stiffness value of SEBS is markedly higher than that of SBS, which meets the requirements that SEBS is harder. It can be seen that graphene has a positive effect on the low temperature performance of adhesives, and with the same amount of graphene, the improvement of the low temperature performance of two-dimensional graphene is better than that of three-dimensional graphene.

Table 5. LAS test results.

Sample ID	N_f	
	Applied Strain of 2.5%	Applied Strain of 5.0%
Pen60/70	17926±39	2236±55
SBS	66681±1544	5060±138
SEBS	56078±1149	5294±130
2DG-L	51548±742	5017±48
2DG-H	38357±1764	3832±268
3DG-L	36840±2550	4388±295
3DG-H	30451±870	3755±124

[1] The numbers after "±" are standard deviations.

Table 6. BBR test results.

Sample ID	−12 °C		−18 °C	
	Stiffness (MPa)	m-value (× 10−2)	Stiffness (MPa)	m-value (× 10−2)
SBS	244.0±9.9	35.0±2.8	390.0±25.5	31.0±1.4
SEBS	314.0±8.5	27.5±3.5	498.5±3.5	20.0±0.0
2DG-L	225.5±7.8	38.0±1.4	372.0±4.2	29.0±2.8
2DG-H	251.5±19.1	38.0±0.0	389.5±3.5	30.5±0.7
3DG-L	250.5±7.8	33.0±0.0	400.5±16.3	18.0±0.0
3DG-H	235.0±2.8	32.5±0.7	377.5±10.6	24.5±3.5

[1] The numbers after "±" are standard deviations.

3.5. Overall Rheological Behavior

The main curve (reference temperature: 60 °C) was obtained over a series of frequency sweeps with various frequencies between 0.01 and 30 Hz and ranged the temperature from 76 to 4 °C. The best fit of the frequency sweep test data is performed in order to obtain a single master curve. The single master curve is based on the Williams-Landel-Ferry (WLF) formula (Equation 1 and Equation 2) and the S-shaped function (Equation 3).

$$\log(a(T)) = \frac{-C_1 \Delta T}{C_2 + \Delta T} \tag{1}$$

where a(T) is the shift factor at a particular temperature T, ΔT is the difference between the quiz temperature and reference temperature and C_1 and C_2 are model constants.

$$\log(\xi) = \log(f) + \log(a(T)) \tag{2}$$

where ξ is the frequency of decrease at reference temperature and f is the test frequency at a particular temperature.

$$\log(G^*) = \delta + \frac{\alpha}{1 + e^{\beta + \gamma \log(\xi)}} \tag{3}$$

where β, γ are the shape parameters, α is the span of G^* values and δ is the minimum modulus value.

In order to obtain the main curve, an evaluation function about the overall rheological properties of asphalt adhesive at wide angle frequencies (10^{-2}-10^{-8} Hz), a series of complicated mathematical calculations were performed. First, the WLF formula (Equation 1 and Equation 2) is substituted into the sigmoid function (Equation 3), then gain the (Equation 4).

$$\log(G^{*}) = \delta + \frac{\alpha}{1+e^{\beta+\gamma(\log(f)+\frac{-C_1\Delta T}{C_2+\Delta T})}} \quad (4)$$

A nonlinear surface fit is then performed using (Equation 4) to acquire parameters C_1 and C_2 , with log(f) and ΔT as independent variables. A different loading frequency is moved at a given temperature (60 °C) to attain a single master curve based on (Equation 2). Finally, the fitted master curve is obtained by best fit based on (Equation 3). The parameters of the WLF formula and the sigmoidal function are shown in Table 7.

Figure 3 is a main curve of the test adhesive G* at a reference temperature of 60 °C. Based on the sigmoidal function, the scattering and smooth curves of lg|G*| and down-conversion ($\lg f_r$) are obtained. According to the principle of time-temperature superposition of viscoelastic materials, the low frequency is high temperature and vice versa. As expected, the increase in frequency results in an increase in the complex shear modulus. It can be seen from figure 3b that the modulus of all modified asphalts is lower at high frequencies and higher at low frequencies than pure asphalt, which indicates that modifiers has better performance at both high and low temperatures. Furthermore, it can be clearly seen that the performance increase at low frequencies is higher than that at high frequencies. At the same time, the performance order in the low frequency state is SEBS>3DG-L>3DG-H=2DG-L>2DG-H>SBS, which elucidates that the incorporation of graphene is beneficial to improve the high temperature performance of binders and the three-dimensional graphene is better than two-dimensional graphene.

Table 7. Model parameters of the WLF formula and sigmoidal function.

Parameters	WLF Formula		Sigmoidal Function				
	C_1 (-)	C_2 (-)	δ (Pa)	α (Pa)	B (-)	γ (-)	R^2 @|G*| (-)
Pen60/70	-8.99089	140.61166	-7.22452	8.50196	0.29137	0.46757	0.99937
SBS	−7.92734	128.67858	-6.88191	8.13285	0.28951	-0.43905	0.99953
SEBS	-7.95639	128.89044	-6.09833	7.28080	0.49296	-0.47701	0.99958
2DG-L	-7.97217	129.20746	-6.4882	7.64965	0.37949	-0.46618	0.99957
2DG-H	-7.94625	129.19929	-6.61167	7.82445	0.37393	-0.45369	0.99954
3DG-L	-8.09145	130.34157	-6.32974	7.53926	0.43375	-0.46519	0.99951
3DG-H	-7.93549	130.50466	-6.39626	7.55406	0.40649	-0.48011	0.99973

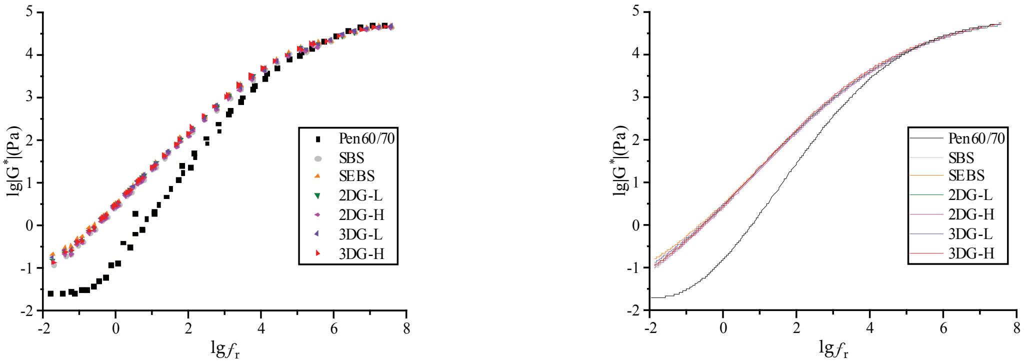

(a) (b)

Figure 3. Master curves of test binders: (a) scatters of test results and (b) sigmoidal fitting curves.

3.6. Molecular Weight Distribution

Figure 4 is a GPC test result of the test adhesive. By analyzing the fluctuation curve of the test adhesive, the elution amount in a specific molecular range can be obtained [19-22]. It is clear that the GPC test results for all adhesives have two peaks and the two peaks are plotted separately for ease of description. As shown in figure 4b and figure 4c, a chromatogram with a retention time of 10.9 ~ 18.0 minutes (molecular weight 22549 g/mol ~ 125 g/mol) and 9.17 ~ 9.71 minutes (molecular weight 79671 g/mol ~ 53749 g/mol) was selected and disjoint them into 8 parts on average. The entire area of the eight samples was adjusted to 1, then their area ratios and molecular weight distributions were compared. A higher area ratio represents a larger percentage of a particular molecular size.

Figure 4b shows molecular weights ranging from 22549 g/mol to 125 g/mol. The components here are mainly asphalt macromolecules. In the range of 16.3 ~ 18.0 min, the proportion of SBS is lower than other modified asphalt. This may be the effect of graphene on other binders. Figure 4c shows molecular weights ranging from 79771 g/mol to 53749 g/mol. The main component here is a polymer macromolecule (SBS or SEBS). On the basis of SBS modified asphalt, graphene moves the peaks of other binders to the left, which proves that the chemical coupling treatment of graphene and SBS has certain effects. It should be specially pointed out that the peak shift of 3DG-L and 3DG-H to the left is significant, which indicates that there is a better coupling mechanism between the three-dimensional structure of graphene and SBS.

The GPC test results is listed in Table 8 which is based on numerical statistics analysis. Five different parameters were selected for the purpose of understanding the situation of the variations of molecular weight distribution during the modification process, i.e. peak molecular weight (Mp), number-average molecular weight (Mn), weight-average molecular weight (Mw), polydispersity (PDI = Mw/Mn) and area ratio (Area). The main component of Peak1 is asphalt and the PDI value of 2DG-H is higher than 2DG-L, showing that the molecular weight distribution of 2DG-H is more dispersed. The PDI value of 3DG-H was lower than that of 3DG-L, indicating that the molecular weight distribution of 3DG-H was more concentrated. The main component of Peak2 is SBS modifier. The Mw values of 3DG-L and 3DG-H are significantly larger than other binders, that is to say, 3D graphene may establish a better coupling mechanism with SBS modifier. From the aspect of area ratio, the area ratio of Peak2 decreased with the increase of graphene content, which substantiates that graphene would contribute to the dissolution of SBS. At the same time, 2DG makes SBS dissolution better than 3DG.

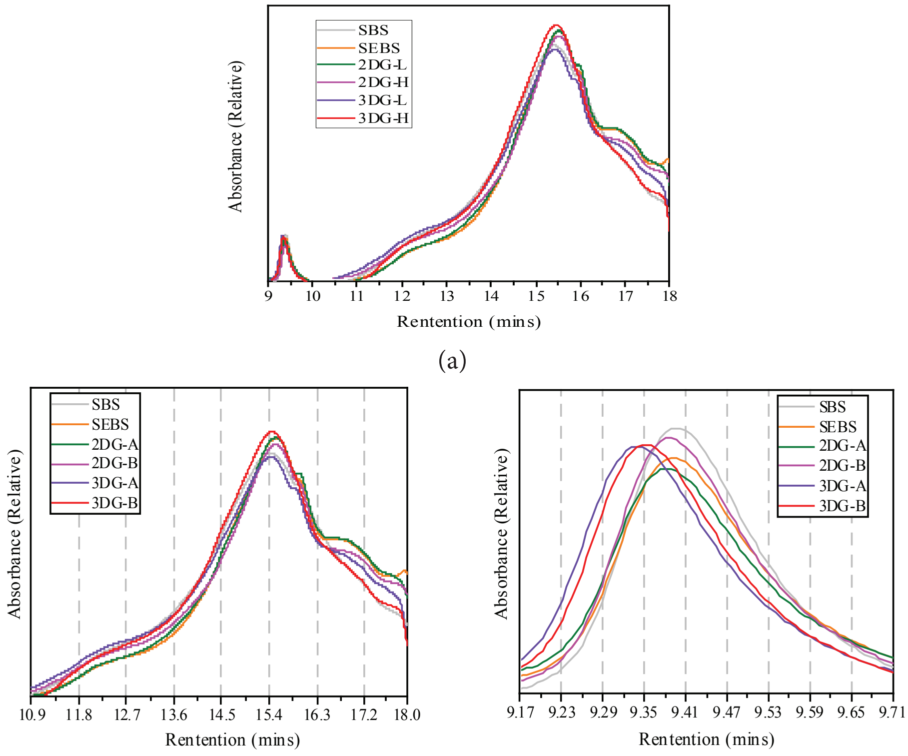

(a)

(b) (c)

Figure 4. GPC test results: (a) chromatograms of test binders (all the range), (b) chromatograms of test binders (from 10.9 to 18.0 mins), and (c) chromatograms of test binders (from 9.17 to 9.71 mins)

Table 8. GPC parameters.

Sample ID		Mp (g/mol)	Mn (g/mol)	Mw (g/mol)	PDI (-)	Area (%)
SBS	Peak 1	804 ± 2	522 ± 36	1648 ± 86	3.1636 ± 0.0504	98.3267
	Peak 2	67759 ± 0	64497 ± 586	65191 ± 380	1.0108 ± 0.0033	1.67328
SEBS	Peak 1	763 ± 0	480 ± 19	1495 ± 97	3.1105 ± 0.0779	98.4319
	Peak 2	67938 ± 1	65251 ± 360	65870 ± 293	1.0095 ± 0.0011	1.5681
2DG-L	Peak 1	758 ± 1	409 ± 67	1302 ± 108	3.2288 ± 0.2625	98.4314
	Peak 2	68297 ± 1	64727 ± 793	65587 ± 742	1.0133 ± 0.0009	1.56858
2DG-H	Peak 1	776 ± 9	490 ± 2	1600 ± 116	3.2669 ± 0.2259	98.8424
	Peak 2	68478 ± 3	64940 ± 542	65596 ± 397	1.0101 ± 0.0023	1.15764
3DG-L	Peak 1	827 ± 5	548 ± 3	1810 ± 138	3.3016 ± 0.2338	98.4327
	Peak 2	70489 ± 1	66843 ± 1095	67542 ± 958	1.0105 ± 0.0022	1.56733
3DG-H	Peak 1	807 ± 2	545 ± 23	1609 ± 44	2.9541 ± 0.0439	98.4945
	Peak 2	70119 ± 1	66435 ± 783	67284 ± 526	1.0128 ± 0.0040	1.50547

[1] The numbers after "±" are standard deviations.

3.7. Chemical Bonds Variation

Figure 5a-g present the FTIR spectra of all binders, respectively. Similar spectra of FTIR indicates their close chemical components [23]. Figure 5a-c shows the FTIR spectra of base asphalt, SBS and SEBS, respectively, and the spectra of the three show similar peaks. They are all at 2854cm^{-1} (symmetric stretching vibration of -CH2-), 1601cm^{-1} (C=C stretching vibration), 1376cm^{-1} (symmetric deformation vibration of -CH3), 750cm^{-1} (=CH out-of-plane deformation of single substituted benzene ring) reaches the peak. SBS and SEBS did not peak at 724 cm^{-1} (-(CH2)n- rocking vibration of alkane groups, n > 4). This may lead to a smaller average molecular weight than neat bitumen. Whether it is base asphalt or SBS modified asphalt, the maximum peaks appear at 2920 and 1460 cm^{-1} respectively, wherein the peak at 2920 cm^{-1} corresponds to the stretching vibration of the C-H and the deformation vibration at the 1460 cm^{-1} corresponds to the C-H, indicating that whether in the matrix asphalt or in the SBS modified asphalt, the CH bond is still the main body, which is consistent with the small amount of SBS or SEBS.

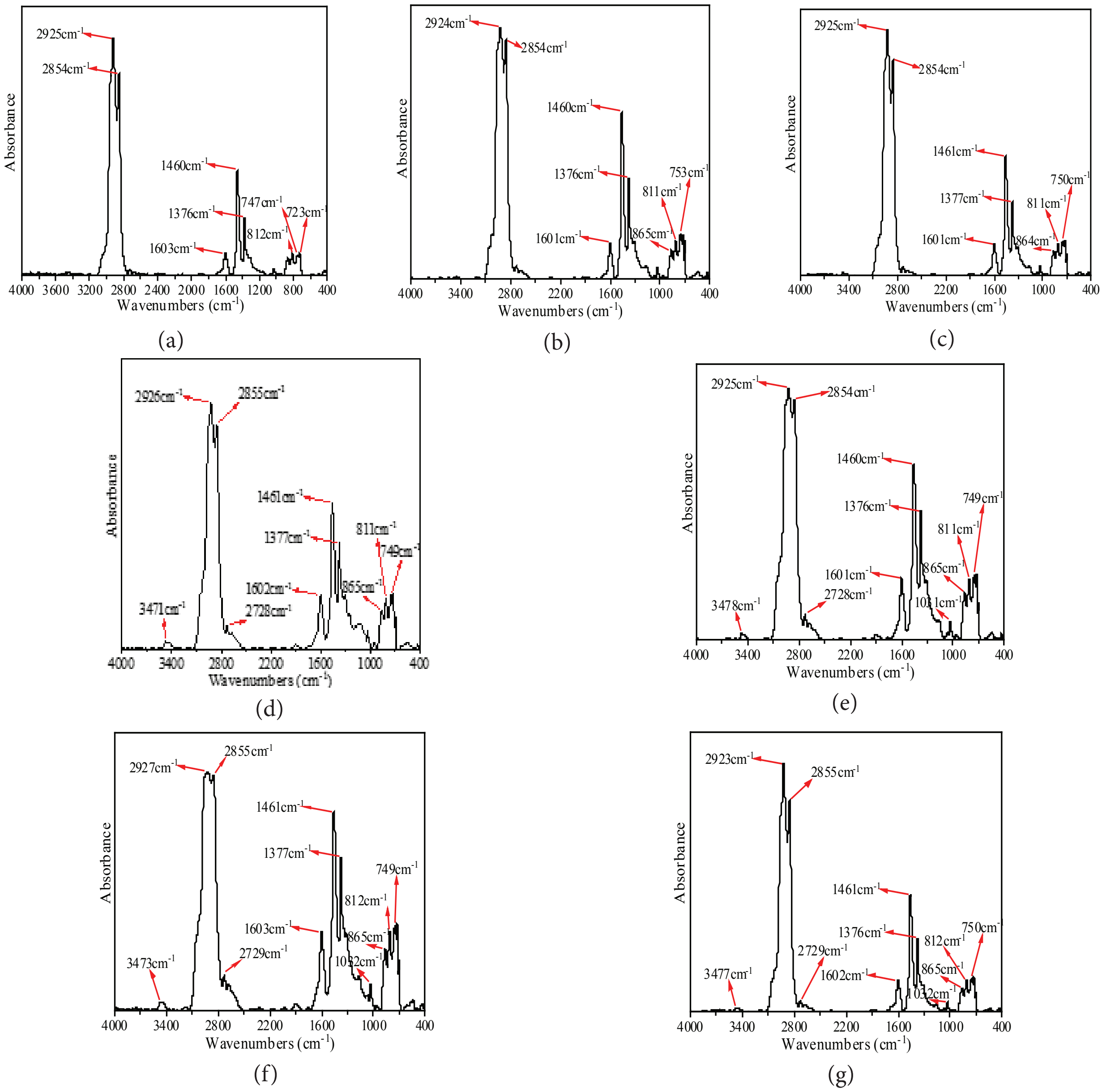

(a)

(b)

(c)

(d)

(e)

(f)

(g)

Figure 5. FTIR test results: (a) Base binder, (b) SBS, (c) SEBS, (d) 2DG-L, (e) 2DG-H, (f) 3DG-L, and (g) 3DG-H. (They're all spectra of the binders)

Figure 5d-g shows the FTIR spectrum of graphene-SBS composite modified asphalt. All spectra have a wide range of 3470 cm^{-1} (-OH or -NH stretching vibration of hydrogen-bonded hydroxyl group and amino groups). Binders also reached a peak near 2730 cm^{-1}, which was caused by the C-H stretching vibration in -CHO, but not in SBS and SEBS. Since there is no oxygen element in SBS, it can be speculated that oxygen element comes from the residue during the preparation of graphene.

Figure 6 shows the micro-morphology of all modifiers under the scanning electron microscope (SEM, Merlin, Zeiss Inc., Germany). In fact, because the SBS/SEBS particles are not at the nanoscale, the amplification of the sample is too large to get an effective and clear image, so the maximum amplification of the experimental control is 50,000 times. Figure 6a-c present that SEBS has a rougher appearance and a larger specific surface area than SBS, which will help to fully contact the asphalt during the binder preparation process. Under chemical coupling, two-dimensional graphene and three-dimensional graphene are well connected with SBS. Figure 6d shows that the two-dimensional graphene appears in a sheet shape and is covered on the SBS. Figure 6e shows that the three-dimensional graphene is embedded in the graphene surface in a block shape. It can be inferred that three-dimensional graphene and SBS have a better connection effect compared with two-dimensional graphene, which is consistent with the GPC test results.

The mechanism of the graphene-SBS composite modifier which contributes to the asphalt modification can be explained as follows. In the modification process by high shear mixing, chemical bonding and physical absorption may result in redistribution of hydrocarbon chains. A more compact and more stable microstructure is then obtained.

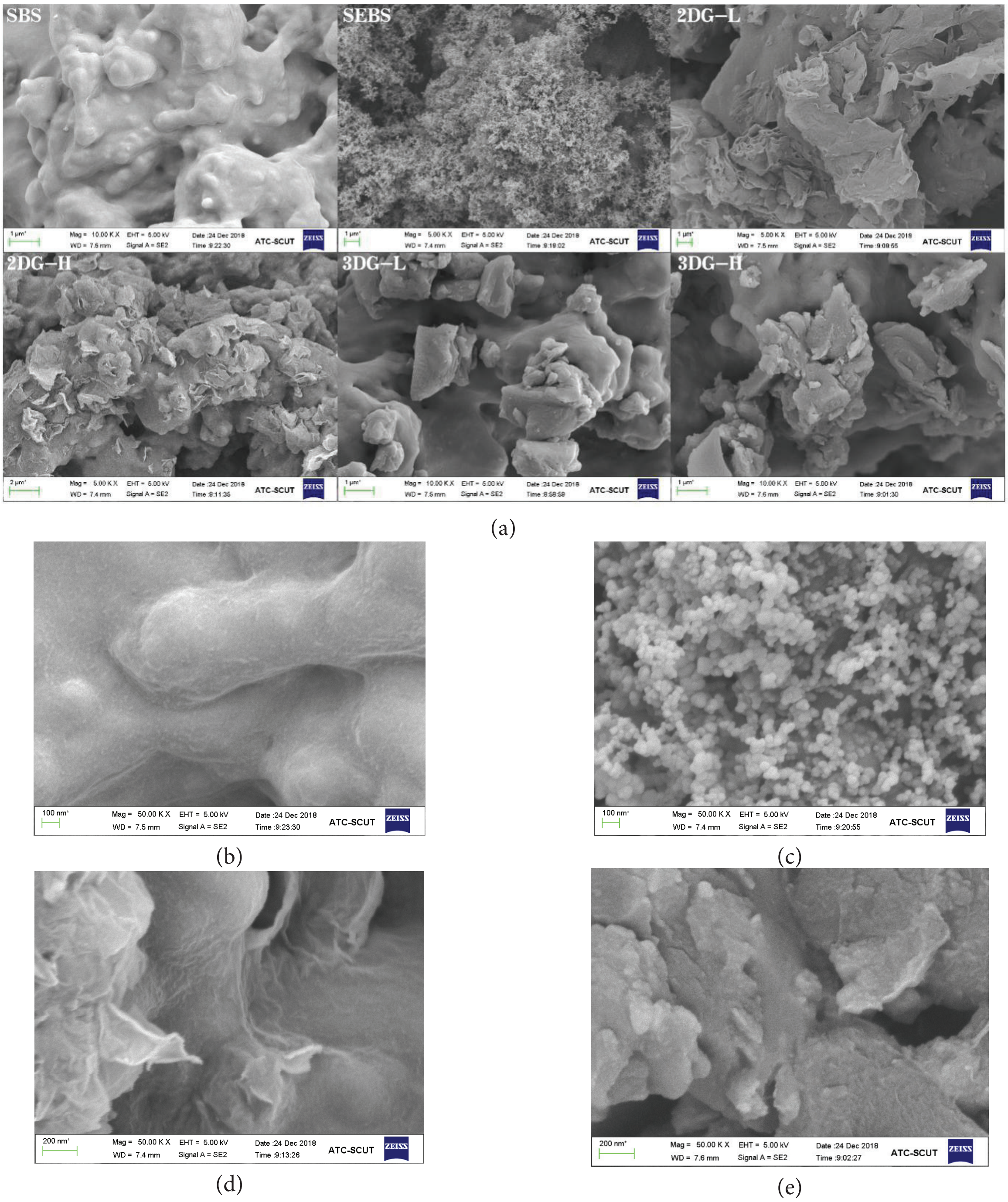

(a)

(b)

(c)

(d)

(e)

Figure 6. SEM results: (a) Microscopic morphology of all modifiers, (b) Pure SBS, (c) Pure SEBS, (d) 2D graphene-SBS composite modifier, and (e) 3D graphene-SBS composite modifier.

4. Conclusions

This study investigated the feasibility of using graphene as a performance enhancer for SBS modified asphalt. Effects of different dimensions and different amounts of graphene on the performance of SBS modified asphalt were comprehensively evaluated using rheological and chemical experiments. In addition, SEBS and SBS modified asphalt was prepared and selected as control groups. Based on the test results, the following were found.

Graphene has limited negative impacts on rutting resistance and fatigue resistance.

There are significant enhancements on the intermediate temperature properties of graphene-SBS modified asphalt. The improvement in asphalt modified by three-dimensional graphene and SBS is particularly remarkable.

Two-dimensional graphene modified SBS asphalt reports better low temperature performance in comparison with control groups.

Because SEBS has a more stable structure (SEBS contains no unsaturated double bonds), SEBS modified asphalt has better rutting performance and fatigue resistance than that of SBS modified asphalt.

Graphene, especially three-dimensional graphene, can establish a good connection with SBS through chemical coupling, besides graphene helps SBS dissolve to a limited extent, resulting in a more uniform binder.

Author Contributions: Data curation, N.Y. Funding acquisition, J.Y. Investigation, S.S., E.K., J.Y., and H.Y. Methodology, J.Y., S.S., E.K., and H.Y. Supervision, J.Y. Writing—original draft, N.Y. Writing—review & editing, H.Y.

Conflict of Interest: The authors declare that there is no conflict of interest regarding the publication of this paper.

Acknowledgments: The authors sincerely acknowledge the funding support from National Natural Science Foundation of China (51678251) and Central University's Basic Research Business Fees Transformation and Cultivation Project (2018KZ001). Trademark or manufacturers' names appear in this paper only because they are considered essential to the object of this paper.

References

[1] Zhang, W., Z. Jia, Y. Zhang, K. Hu, L. Ding, and F. Wang. The Effect of Direct-to-Plant Styrene-Butadiene-Styrene Block Copolymer Components on Bitumen Modification. Polymers, Vol. 11, No. 1, 2019.

[2] Li, Y., S. Wu, L. Pang, Q. Liu, Z. Wang, and A. Zhang. Investigation of the Effect of Mg-Al-LDH on Pavement Performance and Aging Resistance of Styrene-Butadiene-Styrene Modified Asphalt. Construction and Building Materials, Vol. 172, 2018, pp. 584–596.

[3] Yan, C., F. Xiao, W. Huang, and Q. Lv. Critical Matters in Using Attenuated Total Reflectance Fourier Transform Infrared to Characterize the Polymer Degradation in Styrene–Butadiene–Styrene-Modified Asphalt Binders. Polymer Testing, Vol. 70, 2018, pp. 289–296.

[4] Cao Qingxia, He zhaoyi, L. Overview of SBS Modified Asphalt Aging Research. Polymer Materials Science&Engineering, Vol. 27, 2013, pp. 1–5.

[5] Gao, Y., F. Gu, and Y. Zhao. Thermal Oxidative Aging Characterization of SBS Modified Asphalt. Journal Wuhan University of Technology, Materials Science Edition, Vol. 28, No. 1, 2013, pp. 88–91.

[6] Rooholamini, H., R. Imaninasab, and M. Vamegh. Experimental Analysis of the Influence of SBS/Nanoclay Addition on Asphalt Fatigue and Thermal Performance. International Journal of Pavement Engineering, Vol. 20, No. 6, 2019, pp. 628–637.

[7] Zhang, D., Z. Chen, H. Zhang, and C. Wei. Rheological and Anti-Aging Performance of SBS Modified Asphalt Binders with Different Multi-Dimensional Nanomaterials. Construction and Building Materials, Vol. 188, 2018, pp. 409–416.

[8] Zhang, F., C. Hu, and Y. Zhang. Research for SEBS / PPA Compound-Modified Asphalt. Journal of Applied Polymer Science, Vol. 46085, 2018, pp. 1–10.

[9] Ma Feng, Yang Tiantian, Fu Zhen, X. H. Overview of SEBS Modified Asphalt. Petroleum Asphalt, Vol. 32, 2018, pp. 2–6.

[10] Zapién-castillo, S., J. L. Rivera-armenta, M. Y. Chávez-cinco, B. A. Salazar-cruz, and A. M. Mendoza-martínez. Physical and Rheological Properties of Asphalt Modified with SEBS / Montmorillonite Nanocomposite. Vol. 106, 2016, pp. 349–356.

[11] Raimond, J. M., M. Brune, Q. Computation, F. De Martini, and C. Monroe. Electric Field Effect in Atomically Thin Carbon Films. Vol. 306, No. October, 2004, pp. 666–670.

[12] Allen, M. J., V. C. Tung, and R. B. Kaner. Honeycomb Carbon: A Review of Graphene. 2010, pp. 132–145.

[13] Choi, W., I. Lahiri, R. Seelaboyina, Y. S. Kang, W. Choi, I. Lahiri, and R. Seelaboyina. Synthesis of Graphene and Its Applications: A Review Synthesis of Graphene and Its Applications: A Review. Vol. 8436, 2010.

[14] Du, H., and S. D. Pang. Enhancement of Barrier Properties of Cement Mortar with Graphene Nanoplatelet. Cement and Concrete Research, Vol. 76, 2015, pp. 10–19.

[15] Du, H., and S. D. Pang. Mechanical Response and Strain Sensing of Cement Composites Added with Graphene Nanoplatelet Under Tension. Nanotechnology in construction, 2015, pp. 377–382.

[16] Cao, X., B. Zheng, X. Rui, W. Shi, Q. Yan, and H. Zhang. Metal Oxide-Coated Three-Dimensional Graphene Prepared by the Use of Metal–Organic Frameworks as Precursors**. Angewandte Chemie - International Edition, Vol. 53, No. 5, 2014, pp. 1404–1409.

[17] Wen, X., D. Zhang, T. Yan, J. Zhang, and L. Shi. Three-Dimensional Graphene-Based Hierarchically Porous Carbon Composites Prepared by a Dual-Template Strategy for Capacitive Deionization†. Journal of Materials Chemistry A, Vol. 1, No. 39, 2013, pp. 12334–12344.

[18] Yu, H., Z. Leng, F. Xiao, and Z. Gao. Rheological and Chemical Characteristics of Rubberized Binders with Non-Foaming Warm Mix Additives. Construction and Building Materials, Vol. 111, 2016, pp. 671–678.

[19] Ding, Y., B. Huang, and X. Shu. Investigation of Functional Group Distribution of Asphalt Using Liquid Chromatography Transform and Prediction of Molecular Model. Fuel, Vol. 227, No. April, 2018, pp. 300–306.

[20] Wang, D., D. Li, J. Yan, Z. Leng, Y. Wu, J. Yu, and H. Yu. Rheological and Chemical Characteristic of Warm Asphalt Rubber Binders and Their Liquid Phases. Construction and Building Materials, Vol. 193, 2018, pp. 547–556.

[21] Yang, S. H., and L. C. Lee. Characterizing the Chemical and Rheological Properties of Severely Aged Reclaimed Asphalt Pavement Materials with High Recycling Rate. Construction and Building Materials, Vol. 111, 2016, pp. 139–146.

[22] Kim, S., S. H. Lee, O. Kwon, J. Y. Han, Y. S. Kim, and K. W. Kim. Estimation of Service-Life Reduction of Asphalt Pavement Due to Short-Term Ageing Measured by GPC from Asphalt Mixture. Road Materials and Pavement Design, Vol. 17, No. 1, 2016, pp. 153–167.

[23] Fini, E. H., D. J. Oldham, and T. Abu-Lebdeh. Synthesis and Characterization of Biomodified Rubber Asphalt: Sustainable Waste Management Solution for Scrap Tire and Swine Manure. Journal of Environmental Engineering (United States), Vol. 139, No. 12, 2013, pp. 1454–1461.

Viser Technology Pte. Ltd.
Research and Application of Materials Science
doi: 10.33142/msra.v2i1.2024

Research Article Open Access

Combustion Characteristics in Growth Chamber for Verneuil-grown Rutile Crystal

Xudong LIU[1*], Lei WANG[2], Huiyun YAN[1], Xiaoguo BI[3], Xudong SUN[1, 2]

1 College of Environmental and Chemical Engineering, Dalian University, Dalian 116622
2 School of Materials Science and Engineering, Northeastern University, Shenyang 110819
3. School of Renewable of Energy, Shenyang Institute of Engineering, Shenyang 110136

***Corresponding Author:** Xudong SUN, College of Environmental and Chemical Engineering, Dalian University, Dalian 116622, P. R. China. E-mail address: xdsun@mail.neu.edu.cn; Xudong LIU, College of Environmental and Chemical Engineering, Dalian University, Dalian 116622, P. R. China. E-mail address: liuxudong@dlu.edu.cn*

Abstract:
Combustion characteristics of three-tube burner in growth chamber for preparation of single crystal by the Verneuil method were investigated, and the effects of nozzle structure and flow rate on the surface temperature of molten cap were analyzed. The results showed that hydrogen flowed out from the nozzle diffused with inner and outer oxygen, and two flame produced in the center and near the wall of growth chamber. The surface temperature of molten cap were gradually reduced from the center outward. The temperature of molten cap decreased gradually with increasing the nozzle aperture of inner oxygen, and varied slightly with the diameter of hydrogen and outer oxygen nozzle. The temperature of molten cap decreased gradually with increasing the flow rate of inner and outer oxygen, while increased with the flow rate of hydrogen.

Keywords: *rutile crystal; growth chamber; combustion; simulation*

1. Introduction

The father of crystal fabrication technology is A. Verneuil with his flame-fusion growth method 1902. His principles of nucleation and growth control are adapted in most later growth methods from melt. The Verneuil method is one of the main methods for growing rutile single crystals[1-4].

It was crucial for crystal growth to control the distribution of temperature and atmosphere in the growth chamber, especially near the crystal molten cap[5-10]. In the process of crystal growth, the too large radial temperature gradient of the growth chamber, especially near the crystal molten cap, is easy to cause the too low edge temperature of the flat molten cap, as shown in figure 1a, which makes the crystal size less likely to grow, or even shrink. While the radial temperature gradient in the vicinity of the molten cap is too small and the molten cap will be filled, as shown in figure 1b, which make the crystal molten cap is prone to overflow and get the crystal shown in figure 2. The too large axial temperature gradient of the growth chamber shows that the cooling speed of crystal is too quickly, which causes the poor crystal integrity and the high brittleness, as shown in figure 3.

The quality of crystals not only depends on the temperature distribution, but also the oxidation or reduction atmosphere in the growth chamber. It is easy for TiO_2 to lose oxygen, and not easy to crystallize in the reduction atmosphere of hydrogen-oxygen flame[11, 12]. Therefore, the structure of burner was adjusted to obtain the temperature and atmosphere distribution in the growth chamber, which was favorable for the growth of rutile single crystals.

Flame fusion burners are customarily of the two-bube type with inner and outer tubes having tapered tips. The taper at the tip of the outer tube (H_2) has a tendency to constrict the flame pattern and enlarge the axial and radial temperature gradient. The taper at the tip of the inner tube constricts the O_2 flow and the powder fall into a very narrow path so that both the oxygen flow and the powder strike the center of the growing crystal with high velocities sufficient to cause dishing out. In order to reduce the axial and radial temperature gradient, it is not enough to increase the diameter of center nozzle. The more flow rate of oxygen must be maintained to prevent the flareback when the diameter of center nozzle increases, which causes the excessive heat and local temperature for the crystals growth. So, the burner is constructed from three concentric tubes of different diameters. The center tube carrying the oxygen and feed material is of stainless steel. The intermediate and outer tubes carry the hydrogen and oxygen respectively. A water-cooled sleeve is placed over the outer tube of the burner. By adjusting the ratio of hydrogen and oxygen, the three-tube burner not only produce the rich oxygen atmosphere in the growth chamber, which inhibit the lack of oxygen in the growth progress of rutile single crystals, but also reduce the radial temperature gradient, which is conductive to the growth of crystal.

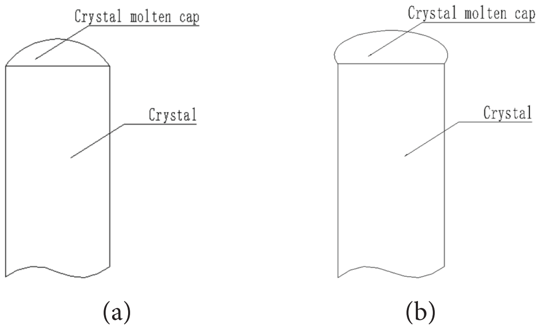

Figure 1. The oblate (a) and engorged (b) shape of crystal molten cap

Figure 2. The overflow of rutile crystal

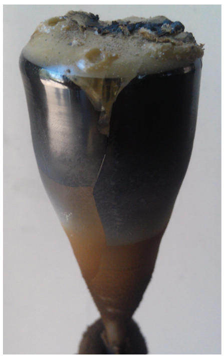

Figure 3. The crack of rutile crystal

The structural perfection of rutile grown by various techniques has been related to the growth conditions and several characterization data on the flame-fusion-grown crystal have been published[13, 14]. The patents and publications do not contain all the necessary data on the experimental conditions for growth of large rutile crystals, and there are few publications about numerical analysis of combustion characteristics in growth chamber for preparation of rutile crystals by the Verneuil method [15-17]. Therefore, a systematic numerical investigation on the flame-fusion growth process of rutile crystals was undertaken in order to evaluate the conditions required in the growth of crack-free crystals.

2. Mathematical Model Formulation

The structure of growth chamber is three-cone type, and the height of growth chamber is 350mm. The diameters of growth chamber from upper to lower are 44mm, 50mm, 60mm and 70mm, respectively. The nozzle of burner is three concentric tubes structure. The diameter of center tube carrying the oxygen and TiO_2 feed powder is 3mm. The inner and outer diameter of intermediate tube carrying the hydrogen is 22mm and 24mm, and the inner and outer diameter of outer tube is 34mm and 35mm. Considering the structure characteristics and symmetry of the growth chamber and the crystal, the schematic diagram, grid used for the computational models and structure size of growth chamber were determined as shown in figure 4, in which the size of grid is 0.2mm and the number of node is 171677.

The temperature and atmosphere distribution in the growth chamber is mainly based on the combustion process of hydrogen and oxygen and the effect of flame

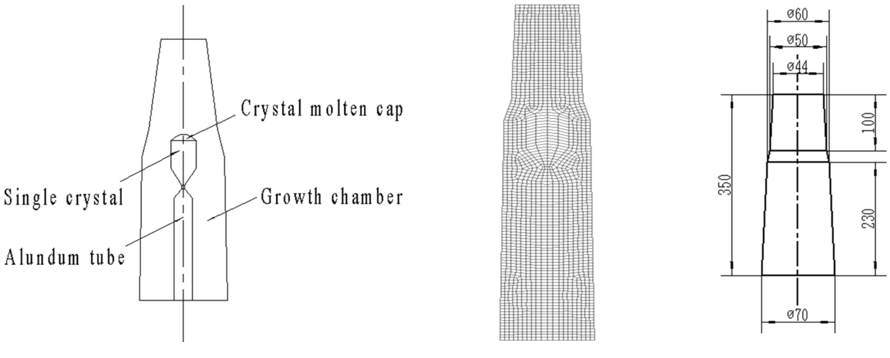

(a) (b) (c)

Figure 4. (a) schematic diagram, (b) grid and (c) structure size of growth chamber

on the heat transfer of the crystal and corundum tube. In the combustion process, the coupling effect of chemical reaction, turbulent flow, convection and radiation heat transfer is analyzed. FLUENT software based on the finite volume and gradient algorithm is used to solve the CFD problems, such as convection and radiation heat transfer and combustion reaction, etc. The differential equations describing the combustion reaction, fluid flow and heat transfer of oxygen and hydrogen in the growth chamber are mainly included mass, momentum and energy conservation equations and heat transfer differential equation, and the mass conservation equation is given by[18]

$$\frac{1}{r}\frac{\partial}{\partial r}\left(r\rho v_r\right)+\frac{\partial}{\partial x}\left(\rho v_x\right)=0 \tag{1}$$

Where ρ is density, and v_r and v_x are velocity vector.

The momentum conservation equation is given by

$$\frac{\partial\left(r\rho v_x v_x\right)}{\partial x}+\frac{\partial\left(r\rho v_x v_r\right)}{\partial r}=\frac{\partial\left(r\tau_{x}\right)}{\partial r}+r\frac{\partial\tau_x}{\partial x}-r\frac{\partial p}{\partial r}+\rho g_x r \tag{2}$$

$$\frac{\partial\left(r\rho v_r v_x\right)}{\partial x}+\frac{\partial\left(r\rho v_r v_r\right)}{\partial r}=\frac{\partial\left(r\tau_r\right)}{\partial r}+r\frac{\partial\tau_x}{\partial x}-r\frac{\partial p}{\partial r} \tag{3}$$

Where p is pressure and τ_{ij} is stress tensor, which is defined as

$$\tau_{xx}=\mu\left[2\frac{\partial v_x}{\partial x}-\frac{2}{3}\left(\nabla\cdot V\right)\right] \tag{4}$$

$$\tau_{rr}=\mu\left[2\frac{\partial v_r}{\partial r}-\frac{2}{3}\left(\nabla\cdot V\right)\right] \tag{5}$$

$$\tau_{rx}=\mu\left[\frac{\partial v_x}{\partial r}+\frac{\partial v_r}{\partial x}\right] \tag{6}$$

Where μ is dynamic viscosity.

The standard k-ε model is determined for turbulent flow, and the equations of turbulent kinetic energy and dissipation rate are given by

$$\frac{1}{r}\frac{\partial}{\partial r}\left[\left(\mu+\frac{\mu_t}{\sigma_k}\right)\frac{\partial(k)}{\partial r}\right]+\frac{\partial}{\partial x}\left[\left(\mu+\frac{\mu_t}{\sigma_k}\right)\frac{\partial k}{\partial x}\right]+G_k+G_b-\rho-Y_M=0 \tag{7}$$

$$\frac{1}{r}\frac{\partial}{\partial r}\left[\left(\mu+\frac{\mu_t}{\sigma_k}\right)\frac{\partial(r\varepsilon)}{\partial r}\right]+\frac{\partial}{\partial x}\left[\left(\mu+\frac{\mu_t}{\sigma_k}\right)\frac{\partial\varepsilon}{\partial x}\right]+C_{1\varepsilon}\frac{\varepsilon}{k}\left(G_k+C_{3\varepsilon}G_b\right)-C_{2\varepsilon}\rho\frac{\varepsilon^2}{k}=0 \tag{8}$$

Where μ_t is turbulent viscosity, and G_k and G_b are turbulent kinetic energy generated by the average velocity gradient and buoyancy, respectively.

The energy conservation equation is given by

$$\frac{1}{r}\frac{\partial}{\partial x}\left(r\rho v_x\int c_p dT\right)+\frac{1}{r}\frac{\partial}{\partial r}\left(r\rho v_r\int c_p dT\right)-\frac{1}{r}\frac{\partial}{\partial r}\left(r\rho D\frac{\partial\int c_p dT}{\partial r}\right)=-\sum_{j'}h_{j'}J_{j'} \tag{9}$$

Where J_j is the diffusion flux of component j.

The combustion reaction rate of oxygen and hydrogen is very fast, and the turbulent mixing of oxygen and hydrogen is much slower than the combustion process. As a result, the total chemical reaction rate is controlled by turbulent mixing, which can be determined as Magnussen and Hjertager vortex dissipation model, and expressed as

$$R_{i,r}=v'_{i,r}M_{w,i}AB\rho\frac{\varepsilon}{k}\frac{\sum_P Y_P}{\sum_j^N v''_{j,r}M_{w,j}} \tag{10}$$

Where Y_P is mass percentage of product P, A and B are empirical constants, which determined as 4 and 0.5 respectively.

Heat transfer differential equation is given by

$$\frac{1}{r}\frac{\partial}{\partial r}\left(k\frac{\partial t}{\partial r}\right)+\frac{\partial}{\partial x}\left(k\frac{\partial t}{\partial x}\right)=0 \tag{11}$$

The boundary conditions are determined as following:

(1) The inlets of oxygen and hydrogen are the volume flow rates, and the flow rates of inner and outer oxygen and hydrogen are 7.2 L/min, 3.8 L/min and 19 L/min, respectively.

(2) The heat flow in the upper part of growth chamber is small, and treated to be an adiabatic boundary.

(3) Because the heat transfer in the axial direction of the furnace is much less than that in the radial direction, it can be neglected, and the heat transfer in radial direction is determined by

$$q_2=h_{eff}\left(T_w-T_f\right) \tag{12}$$

Where h_{eff} is the effective heat transfer coefficient, including the convection and radiation heat transfer from the furnace wall to the environment.

(4) The pressure of outlet of the growth chamber is zero.

The density and special heat of rutile crystals were 4270 kg/m³, 812 J/kgK respectively, and the thermal conductivity was the fuction of temperature, as shown in Talbe 1. When the temperature is greater than the melting point, considering the influnce of the flow on heat tuansfer, the effective thermal conductivity was used to the heat truansfer in crystal, so the effective thermal conductivity is greater than the thermal conductivity of solid crystals.

Table 1. the thermal conductivity of rutile crystals

T (K)	300	600	1000	2000	2123	2500
λ (W/mK)	10	9.8	5	4	3.5	60

3. Results and Discussions

3.1. Temperature and Component Distribution

The temperature and distribution of gas components in the growth chamber not only affect the combustion reaction, but also determine the stable growth process and microscopic quality of rutile crystal. In the actual growth process of rutile single crystal, the flow rates of inner and outer oxygen and hydrogen were 7.2L/min, 3.8L/min and 19L/min respectively when the crystal diameter was 24mm. According to the above equations and the boundary conditions, the FLUENT software was used to calculate the distribution of gas components in the growth chamber.

The radial temperature and component distribution characteristics of hydrogen, oxygen and water vapor at different distance from the nozzle, such as 10mm, 50mm and 90mm, were analyzed quantitatively, and the results were shown in figure 5. The inner oxygen was mainly concentrated within the distance 50mm from the nozzle, while the outer oxygen was mainly concentrated within the distance 30mm from the nozzle and the trend diffusing to the wall of growth chamber was more obvious, as shown in figure 6. However, the radial molar fraction distribution of inner oxygen at the distance 90mm from nozzle was obviously different from the others position, and the inner oxygen flowed outward along the radial direction and reacted to hydrogen surrounding crystal when it reached the surface of the molten cap, which led to increasing the edge temperature of crystal and was easy to cause the overflow problem.

It was difficult for hydrogen to spread to the inner oxygen and outer oxygen in the vicinity of the nozzle due to the large diffusion resistance produced by the high partial pressure of oxygen, and the two reaction peaks generated in the interface of hydrogen and oxygen. The reaction peak of outer oxygen and hydrogen disappeared and the distribution of hydrogen was gradually inclined to uniformity in the wall direction with the increasing of the distance from the nozzle, which showed that the outer oxygen was reacted completely and the oxidation atmosphere was supplied by the inner oxygen in the growth chamber. The concentration and radial concentration gradient of hydrogen decreased gradually with increase of distance from the nozzle. The farther the distance was, the more the diffusion and mixing of oxygen and hydrogen were. The combustion reaction of hydrogen and oxygen occurred in the process of mutual diffusion, and the molar fraction of water vapor was maximal when the molar fraction of hydrogen was the same as the oxygen.

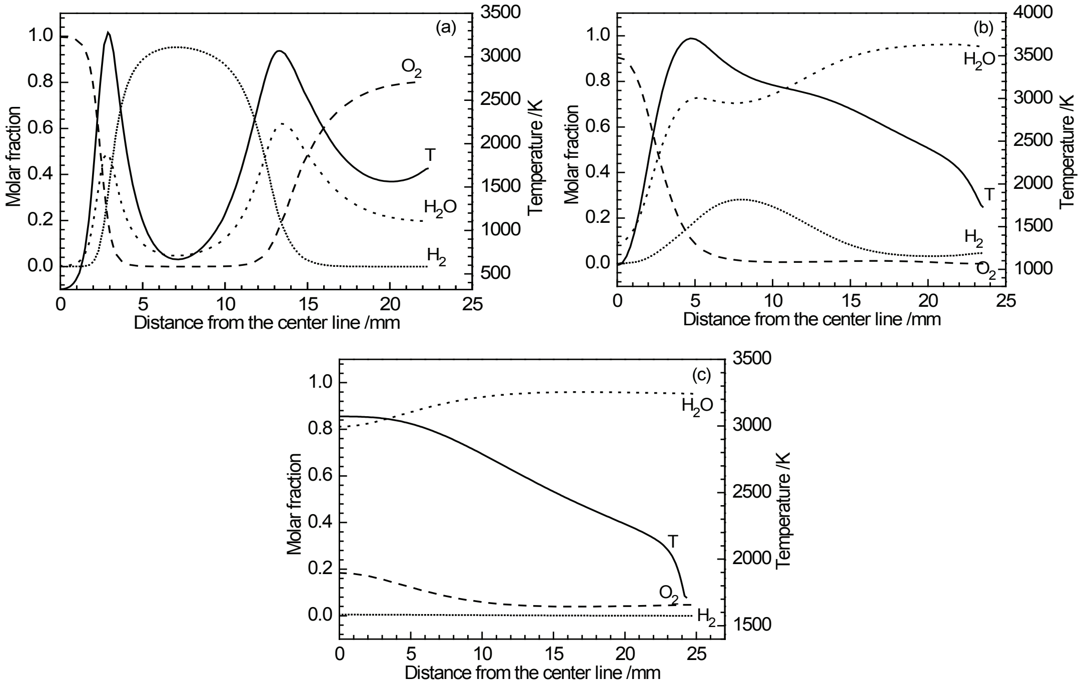

Figure 5. The temperature and molar fraction distribution of H_2, O_2, and H_2O at different distance, 10mm (a), 50mm (b) and 90mm (c) from the nozzle

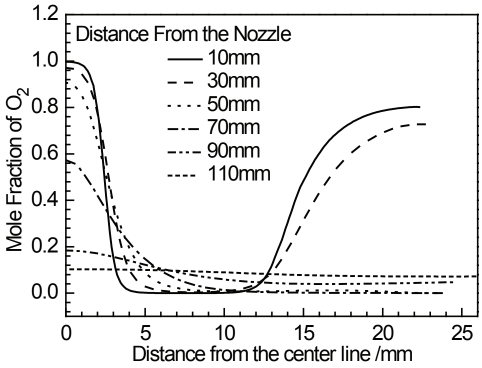

Figure 6. Radial oxygen distribution in growth chamber

The temperature distribution in the growth chamber was the most critical condition in the growth process of crystal, which determined whether the crystal was able to grow steadily and the final size and quality of crystal. The hydrogen flowed out from the nozzle diffused with inner and outer oxygen, and two high temperature flame produced in the center and near the wall of growth chamber, as shown in figure 7. Since the reaction rate of hydrogen and oxygen was very fast, the combustion process was mainly determined by the diffusion of hydrogen and oxygen. The mutual diffusion degree of outer oxygen and hydrogen was high and the combustion reaction was complete due to their similar blowing depth, which could be seen in figure 5.

Whether the crystal was melting or crystallizing at the growth position was determined by the axial temperature in the growth chamber, and the radial temperature distribution determined the size of crystal. As can be seen from figure 5, there was two temperature peaks near the nozzle, and only one temperature peak far away from the nozzle, where the radial concentration of water vapor was maximal. The high temperature flame cooled from the reaction interface in the radial direction due to the heat lost from the wall of furnace. There was a temperature boundary layer near the wall, where the temperature was in a sharp decline. The radial temperature closed to the nozzle increased with decreasing the distance from the wall, which was more obvious at the position closer to the nozzle. This was because that the outer oxygen flow formed a vortex in the vicinity of the wall, and the high-temperature water vapor was involved in the vortex.

The growth state was determined by the temperature of molten cap of the growing crystal, which determined the superheat and viscosity of molten cap. If the superheat of molten cap was too large and the viscosity was too small, the molten cap was east to produce the large deformation when the greater pressure generated by airflow on it, which led to the overflow problem and the crystal growth failure, as shown in figure 2. While the molten cap was not easy to expand outward due to the too large viscosity, and the diameter of molten cap of the growing crystal decreased gradually. Sometimes the TiO_2 powder blown into the molten crystal was not melted due to the lower melted superheat, which produced defects such as inclusions and crack in the crystal, as shown in figure 3. Therefore, it was very critical to analyze the temperature and oxygen distribution of the molten cap, as shown in figure 8.

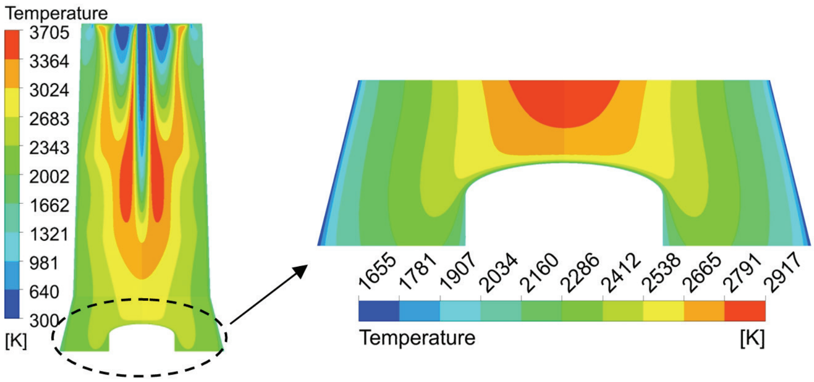

Figure 7. The temperature in the growth chamber

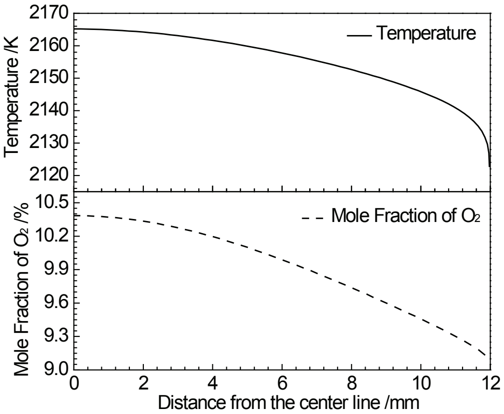

Figure 8. The distribution of radial temperature and mole fraction of oxygen in surface of molten cap

The surface temperature and mole fraction of oxygen of molten cap were gradually reduced from the center outward, and the gradient was small in the diameter range of less than 10mm. The magnitude of decreasing temperature increased with increasing the distance from the center line, and the maximum magnitude reached in the edge of the crystal.

3.2 Effects of Nozzle Aperture

The more and more flow rates of hydrogen and oxygen needed to meet the increasing diameter of crystal during the growth of rutile single crystal by the Verneuil method. If the nozzle aperture was too small, it was easy to form the turbulence in growth chamber when the flow rates of hydrogen and oxygen was larger, which caused the greater impact to the molten cap and the unstable crystal growth. If the nozzle aperture was too large, the larger flow rates of hydrogen and oxygen was required to maintain the molten crystal at the growth position, which led to the higher edge temperature of molten cap and caused the overflow of molten crystal. Therefore, it was critical to analyze the effects of nozzle aperture on temperature distributions of the molten cap. The temperature distributions were calculated at the different nozzle apertures of inner oxygen, hydrogen and outer oxygen when the flow rates of inner and outer oxygen and hydrogen are 7.2 L/min, 3.8 L/min and 19 L/min respectively, and the results were shown in figure 9.

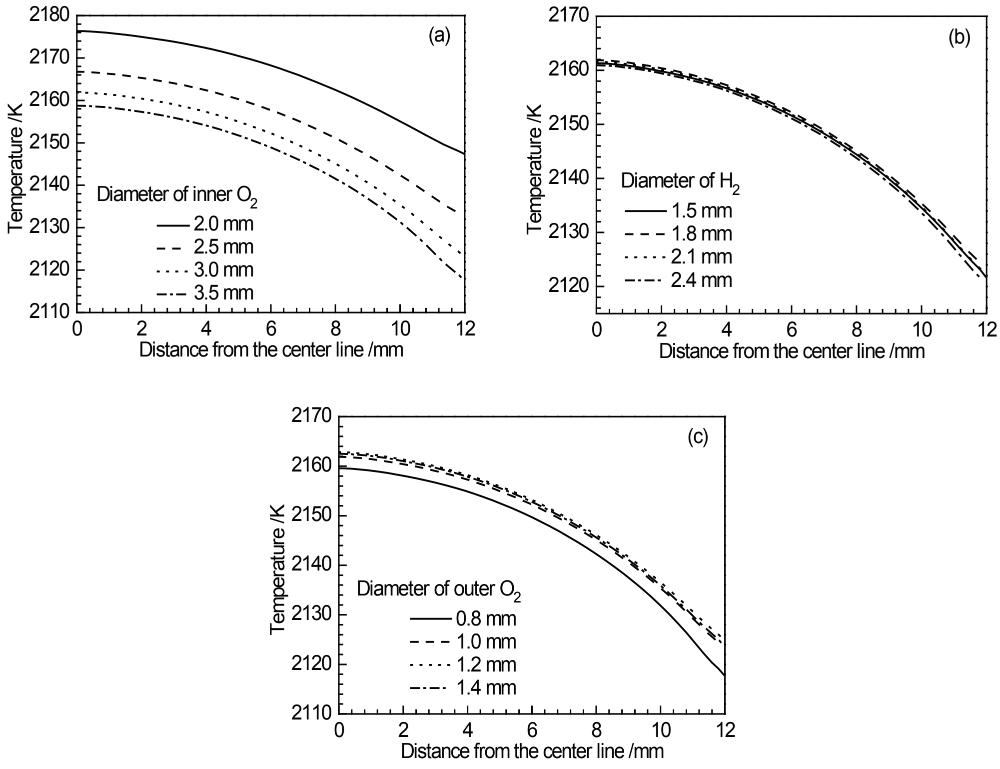

Figure 9. Effects of diameter of inner oxygen (a), hydrogen (b) and outer oxygen (c) on temperature in molten cap

The effects of nozzle aperture on the temperature of molten cap could be seen in figure 9. The temperature decreased gradually with increasing the nozzle aperture of inner oxygen, and the changing trend was more obvious in the smaller nozzle aperture. This was because that the hydrogen distribution in the growth chamber was essentially invariant when the apertures and the flow rates of hydrogen and outer oxygen were unchanged. The blowing depth of inner oxygen decreased and the diameter of oxygen flow increased with increasing the diameter of inner oxygen nozzle, which meant that the diameter of high-temperature zone of flame increased and the length decreased. So the center zone temperature of molten cap decreased with increasing the nozzle aperture of inner oxygen.

Although, the blowing depth and diameter of hydrogen flow changed with increasing the diameter of hydrogen nozzle, the effects of hydrogen distribution on the combustion reaction in growth chamber were little due to the good thermal expansion and diffusion of hydrogen. So the surface temperature of molten cap varied slightly with increasing the diameter of hydrogen nozzle.

As shown in figure 9(c), the surface temperature of molten cap varied slightly with increasing the diameter of outer oxygen nozzle due to the small change of blowing depth, which effected slightly by the diameter of outer oxygen.

3.3 Effects of Flow Rate

The growing diameter of crystal needed the more amounts of hydrogen and oxygen. The relative flow rates of hydrogen and oxygen not only determined the oxidation or reduction atmosphere, more importantly, but also the temperature distribution in the growth chamber during the growth process of rutile single crystal by the Verneuil method. In order to analyze the effects of flow rates of hydrogen and oxygen on the surface temperature of molten cap and the others were constant. The results were shown in figure 10.

As could be seen in figure 10(a), when the flow rate of hydrogen and outer oxygen were kept constant, the temperature of molten cap decreased gradually with increasing the flow rate of inner oxygen. This was because that the combustion heat depended mainly on the flow rate of hydrogen when the flow rate of oxygen was excessive in the growth chamber. Invariable flow rate of hydrogen meant that the blowing depth and distribution of hydrogen had little change. The velocity of inner oxygen flow increased with the increasing flow rate of inner oxygen, which led to the more inactive inner oxygen flow. The inactive inner oxygen flow reduced the temperature and increased the radial temperature gradient in the molten cap, which increased the internal thermal stress of crystal and reduced the crystal quality.

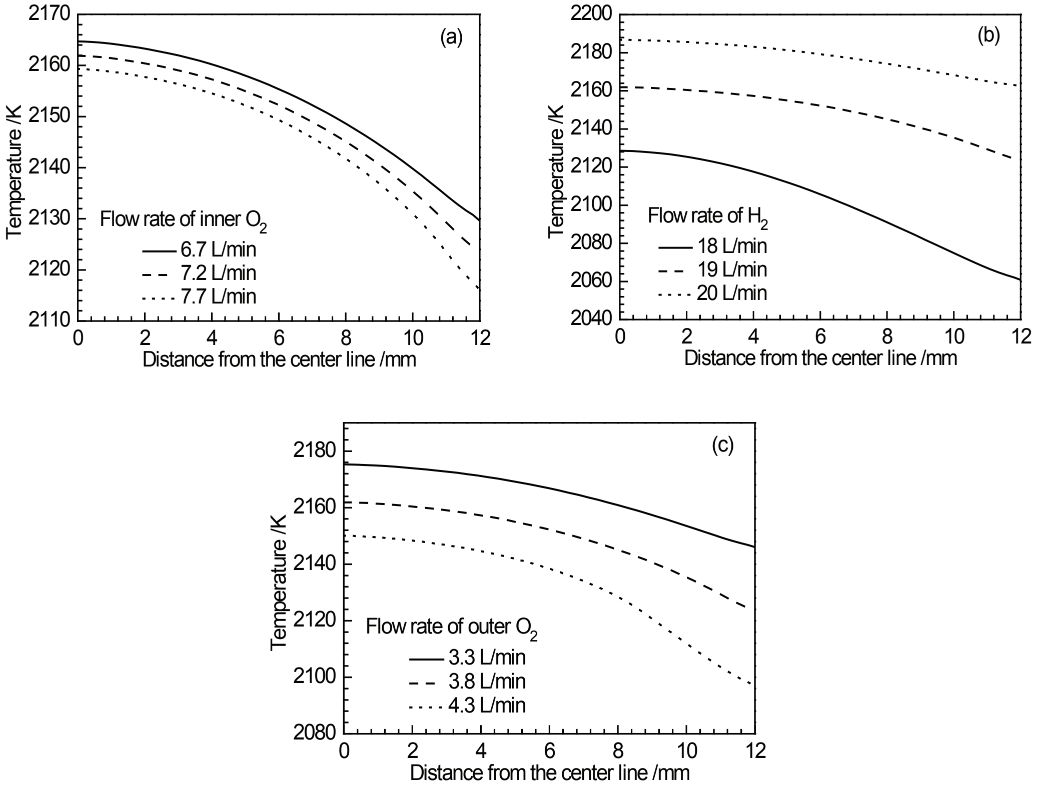

Figure 10. Effects of flow rate of inner oxygen (a), hydrogen (b) and outer oxygen (c) on temperature in molten cap

The surface temperature of molten cap increased obviously with the increasing flow rate of hydrogen. Theoretically, the total combustion reaction heat depended on the flow rate of hydrogen under the conditions of excessive oxygen flow in the growth chamber. The blowing depth of centric oxygen flow unchanged basically due to the same in inner oxygen flow when the flow rate of hydrogen changed. With the increasing flow rate of hydrogen, the blowing depth of hydrogen increased, which led to the more oxygen reacted with hydrogen and decreased the distance between the high temperature flame and the molten cap and increased the surface temperature of molten cap. The diffusion ability and diameter of hydrogen increased with the increasing flow rate of hydrogen, which led to the more diameter of high temperature zone. Therefore, the more flow rate of hydrogen need to meet the increasing crystal size in the process of rutile crystal growth, and increase the flow rate of hydrogen slowly in order to avoid the edge of the crystal temperature too high and cause overflow.

As could be seen in figure 10(c), when the flow rate of inner oxygen and hydrogen was kept constant, the temperature of molten cap decreased gradually with increasing the flow rate of outer oxygen. This was because that the combustion heat depended mainly on the flow rate of hydrogen when the flow rate of oxygen was excessive in the growth chamber. Invariable flow rate of hydrogen meant that the blowing depth and distribution of hydrogen had little change, the more hydrogen reacted with outer oxygen and the less hydrogen reacted with inner oxygen, so the surface temperature of molten cap decreased with the increasing flow rate of outer oxygen. The more increasement of outer oxygen flow was, the more inactive inner oxygen flow was, which reduced the temperature in molten cap.

4. Conclusions

The hydrogen flowed out from the nozzle diffused with inner and outer oxygen, and two high temperature flame produced in the center and near the wall of growth chamber. The surface temperature of molten cap were gradually reduced from the center outward. The temperature of molten cap decreased gradually with increasing the nozzle aperture of inner oxygen, and the changing trend was more obvious in the smaller nozzle aperture. While they varied slightly with the diameter of hydrogen and outer oxygen nozzle. The temperature of molten cap decreased gradually with increasing the flow rate of inner and outer oxygen, while increased with the flow rate of hydrogen.

Acknowledgements: This work was supported by the Projects of National Natural Science Foundation of China, No. 51872033 and No. 51732007, and by the Project of Dalian Natural Science Foundation, No. 2019J12GX044, and by the Project of Natural Science Foundation of Liaoning Province, No. 2019-ZD-0572.

References

[1] Joseph A. Adamski. New Oxy-Hydrogen Burner for Flame Fusion[J].Journal of Applied Physics, 1965, 36(5):1784-1786

[2] Hans J. Scheel. Historical aspects of crystal growth technology[J]. Journal of Crystal Growth, 2000, 211: 1-12

[3] H. J. Scheel. Crystal growth technology CGT for energy: saving energy and renewable energy[J], Journal of Crystal Growth, 2005, 275:331-337

[4] Dr.-Ing. Hans J. Scheel, Dr. Peter Capper, Hans J. Scheel, et, al. Crystal Growth Technology: Chapter 16 Flame-Fusion (Verneuil) Growth of Oxides[M]. John Wiley & Sons, Ltd, 2008, Nov. 25

[5] F. B. Khambatta, P. J. Gielisse and M. P. Wilson. Initial thermal model of the flame fusion crystal growth process[J].Journal of Crystal Growth, 1972, 13:710-717

[6] Floricica Barvinschia, Jean-Louis Santaillerb, Thierry Duffarb, Hervé Le Gal, Modelling of Verneuil process for the sapphire crystal growth[J], Journal of Crystal Growth, 1999, 198-199:239-245

[7] Shuichi Kawaminami, Keisuke Mochizuki, Shinobu Hashimoto, et, al. Coloration of Ti-doped sapphire grown by the Flame-Fusion Method[J]. Journal of Asian Ceramic Societies, 2013, 1(4): 362-367

[8] Xiao Guo Bi, Xu Dong Liu, Wei Niu. Flame-fusion growth of rutile single crystal[J].Advanced Materials Research, 2012, 535-537: 2571-2575

[9] J. B. Donnet, H. Oulanti, T. Le Huu, M. Schmitt. Sythesis of large crystal diamond using combustion-flame method[J]. Carbon, 2006, 44(2):374-380

[10] H. Tang, H. Li and J. Xu, Advanced Topics on Crystal Growth[M]. Ed. by S. O. Ferreira, InTech, Croatia, 2013: 307–333

[11] K T Hwang, J H Pee, W S Cho, S H Eom, J K Lee, Effect of Alumina Starting Materials on Spheroidization in Flame Fusion Method [J]. Materials Science Forum, 2010, 654-656:2382-2385

[12] Xiaoguo BI, XIU Zhi-meng, MA Wei-min, Xudong SUN, Study on Growth of Rutile (TiO2) Single Crystals, Journal of Northeastern University(Natural Science), 2004, 25(10):977-979

[13] Xiaoguo BI, XIU Zhi-meng, Xudong SUN, ZHAO Hong-sheng, CAO Zhong-jie, GUO Guo-you, XIAO Ji-tian, Experimental Study on Growth Conditions of Big- bulk Rutile Crystal[J], Journal of Synthetic Crystals, 2004, 33(2):244-249

[14] S H Eom, J H Pee, J K Lee, K T Hwang, W S Cho, Effects of Chemical Composition and Particle Size of Starting Aluminum Source on the Spheroidization in the Flame Fusion Process [J]. Journal of Korean Powder Metallurgy Institute, 2009, 16(6):431-437.

[15] LIU Xudong, BI Xiaoguo, TANG Jian, NIU Wei, DONG Yingnan, Study on combustion characteristic in growth chamber for preparation of single crystal with flame fusion method[J], Chinese Journal of Materials Research, 2015, 29(5):394-400

[16] LIU Xudong, BI Xiaoguo, TANG Jian, CAI Yunping, SUN Xudong, Numerical Simulation of Temperature Distribution in Growth Chamber for Preparation of Rutile Single Crystal with Flame Fusion Method[J], Journal of Synthetic Crystals, 2016, 1: 138-145

[17] LIU Xudong, BI Xiaoguo, TANG Jian, NIU Wei, SUN Xudong, Numerical simulation of the influence of growth parameters on the temperature distribution in growth chamber[J], Journal of the Chinese Ceramic Society, 2016, 44(5): 1-7

[18] Stephen R Turns. An Introduction to Combustion Concept and Applications[M]. Tsinghua university press, 2015

Publisher: Viser Technology Pte. Ltd.

URL: www.viserdata.com

Add.:21 Woodlands Close, #08-18,
Primz Bizhub SINGAPORE (737854)